UNIVERSITÀ DEGLI STUDI DI PADOVA

Dipartimento di Fisica e Astronomia "Galileo Galilei"

Master Degree in Physics of Data

Final Dissertation

Modelling carbon dynamics in Lagrangian oceanic ecosystems: applications to fertilization experiments and mesoscale eddies

Thesis supervisor

Prof. Samir Suweis

Thesis co-supervisor

Dr. Enrico Ser-Giacomi

Candidate

Stefano Campagnola

Academic Year 2023/2024

Abstract

Plankton is a key component of the marine environment and provides invaluable ecosystem services, ranging from carbon sequestration to biodiversity preservation. Plankton is embedded in patches of water that are continuously moving, stretching, and diluting under the continuous effect of turbulent oceanic currents. In this work, we present an ecosystem model that describes biomass production and carbon dynamics within a Lagrangian patch in the ocean. The model accounts for spatial heterogeneity emerging from nutrient and phytoplankton interaction and physical processes. First, we illustrate the theoretical background starting from a simple homogeneous case. Then, we show that our framework is able to reproduce observed biogeochemical patterns during the SOIREE fertilization experiment. In particular, the predicted CO_2 partial pressure anomaly is compared with in-situ measurement and other modelling frameworks present in the literature. Finally, we present an extension of the Lagrangian approach to the case of three-dimensional mesoscale eddies, and we discuss possible future research directions.

Un'isola è una porzione di terraferma
completamente circondata dalle acque,
un mondo a sé stante.
È luogo lontano e appartato,
uno spazio discreto e protettivo.

Un'isola deve bastare a se stessa.

Contents

Chapter 1

Introduction

The interest in studying Lagrangian oceanic ecosystems derives from the crucial interplay between physics, biology, and biogeochemistry. This interdisciplinary approach is becoming increasingly common in the scientific literature related to complex systems like the ocean, in which the transportation given by the medium is so more effective with respect to what happens to living beings in the atmosphere.

Fluid mechanics, in this respect, is a powerful tool to interpret water parcels' movements. Different approaches like Lagrangian and Eulerian descriptions can be taken depending on the contest, while fluid deformations are mainly controlled by flow velocity fields. An important role is covered by the system of reference in which we are observing the fluid, since it can simplify a lot the mathematics and the understanding of the patch motion.

The growth of oceanic fauna is linked to presence of primary producers, mainly to planktonic organisms. The huge number of phytoplanktonic species populating terrestrial waters form the basis of the marine food web, collecting all the principal nutrients dissolved in sea-water to produce organic compounds. Environmental conditions affecting survival of phytoplankton can set the foundation of irreversible decline for many living creatures.

Primary production is related to the transformation of several basic elements from inorganic to organic. In particular, carbon exists in water in various forms, starting from dissolved carbon dioxide coming from the atmosphere to sedimented compounds floating in the deep ocean. Equilibrium between these shapes plays a crucial role in regulate carbon sequestration and so Earth's climate.

1.1 Lagrangian approach to fluids flows

1.1.1 Lagrangian and Eulerian descriptions

There are two ways to describe fluid motion. In the Lagrangian specification, we track individual fluid particles as they move within a flow field. In the Eulerian specification, we observe the characteristics of the flow field at fixed locations [16]. Both of the description are useful in physics, since they are suited to different types of problems and analyses.

Lagrangian specification comes from Newton's dynamic, in which one is normally concerned with positions and momenta of material points [32] (that's why is also called *material point of view*). The idea is that the fluid can be subdivided into fluid particles, whose identity remains clearly separated during the inner motion. The trajectory of a single fluid particle will satisfy Newton's law

$$\frac{d\mathbf{x}(t)}{dt} = \mathbf{F}(\mathbf{x}, t) \tag{1.1}$$

with initial condition

$$\mathbf{x}(0) = \mathbf{x}_0 \tag{1.2}$$

Any scalar or vector property $\mathcal{F}$ of the flow field will then depend on the paths that relevant particles (the one passing on $\mathbf{x}$) followed

$$\mathcal{F}(\mathbf{x}(t; \mathbf{x}_0), t) \tag{1.3}$$

This representation is perfectly acceptable in principle and provide a complete characterization of the fluid dynamical system. However, in practical terms, it's more than what is frequently needed, and trying to make it work for many fluid particles is very complicated.

Eulerian specification focuses instead on flow field properties at specific locations in the space that fluid particles cross in their trajectories. Spatial and temporal variables become independent of each other, allowing to express flow field properties simply as

$$\mathcal{F}(\mathbf{x}, t) \tag{1.4}$$

The condition of equivalence between the two specifications can be set requiring

$$\mathcal{F}(\mathbf{x}(t; \mathbf{x}_0), t) = \mathcal{F}(\mathbf{x}, t), \qquad \text{with} \quad \mathbf{x} = \mathbf{x}(t; \mathbf{x}_0) \tag{1.5}$$

Applying a total time derivative to the left-hand side, one would have the definition of flow-field property temporal derivative in the Lagrangian description as

$$\frac{d\mathcal{F}(\mathbf{x}(t; \mathbf{x}_0), t)}{dt} \tag{1.6}$$

which can be decomposed, in the Eulerian description as

$$\frac{\partial \mathcal{F}}{\partial t} + \frac{\partial \mathcal{F}}{\partial x}\frac{dx}{dt} + \frac{\partial \mathcal{F}}{\partial y}\frac{dy}{dt} + \frac{\partial \mathcal{F}}{\partial z}\frac{dz}{dt} = \frac{\partial \mathcal{F}}{\partial t} + \mathbf{v} \cdot \nabla \mathcal{F} = \frac{D\mathcal{F}}{Dt} \tag{1.7}$$

The last equality defines the D/Dt as the total time derivative experienced in the Eulerian description (*material derivative*), that turns out to be very different with respect to the one experienced in the Lagrangian. Added to the local rate of change $\partial \mathcal{F}/\partial t$, there is also an advective term involving the scalar product between the velocity field $\mathbf{v}$ and the spatial gradient of $\mathcal{F}$. This represents the contribution coming from surrounding fluid that has been dislocated in the new position $\mathbf{x}$, and it's related to the mass conservation law.

1.1.2 Water patch deformations

The velocity field in a fluid, denoted with $\mathbf{v}(\mathbf{x}, t)$, represents, in the Eulerian description, the velocity of an element of fluid that is located at a position $\mathbf{x}$ at time t. Relative position between particles inside a fluid can change in time, due to differences in the velocity direction and intensity at diverse spots. If two sites in the fluid A and B are subject to the same velocity vector ($\mathbf{v}(\mathbf{x}_A, t) = \mathbf{v}(\mathbf{x}_B, t)$), relative position between them does not change. If instead the two velocities $\mathbf{v}(\mathbf{x}_A, t)$ and $\mathbf{v}(\mathbf{x}_B, t)$ are

different, this would lead to a sliding between A and B that modifies the distance vector $\mathbf{d} = \mathbf{x}_B - \mathbf{x}_A$. The rate at which this distance changes is

$$\frac{d\mathbf{d}}{dt} = \frac{d\mathbf{x}_B}{dt} - \frac{d\mathbf{x}_A}{dt} = \mathbf{v}(\mathbf{x}_B, t) - \mathbf{v}(\mathbf{x}_A, t) \simeq \nabla \mathbf{v}^T \left(\frac{\mathbf{x}_A + \mathbf{x}_B}{2}, t \right) \cdot \mathbf{d} \tag{1.8}$$

and so is related, at first order, to the gradient of the velocity field $\nabla \mathbf{v}$ computed in the midpoint between A and B.

Relative displacements between fluid particles in a smooth flow can indeed be characterized by the strain-rate tensor $\mathbf{E}$ and the rotation tensor $\mathbf{R}$, which are defined in terms of combinations of the velocity field gradient components [16]

$$\begin{aligned} \mathbf{E} &= \frac{1}{2} \left(\nabla \mathbf{v}^T + \nabla \mathbf{v} \right), \qquad & \mathbf{R} &= \frac{1}{2} \left(\nabla \mathbf{v}^T - \nabla \mathbf{v} \right) \\ E_{ij} &= \frac{1}{2} \left(\frac{\partial v_i}{\partial x_j} + \frac{\partial v_j}{\partial x_i} \right), \qquad & R_{ij} &= \frac{1}{2} \left(\frac{\partial v_i}{\partial x_j} - \frac{\partial v_j}{\partial x_i} \right) \end{aligned} \tag{1.9}$$

Rotational tensor $\mathbf{R}$ is antisymmetric, so its diagonal elements are zero and its off-diagonal elements are equal and opposite. Given the definition of vorticity $\boldsymbol{\omega} = \nabla \times \mathbf{v}$, the latter can be reformulated as

$$R_{ij} = -\sum_k \epsilon_{ijk} \omega_k \tag{1.10}$$

Both $\mathbf{R}$ and $\boldsymbol{\omega}$ will then depend on the frame of reference, since it is always possible to choose a frame of reference that rotates with the flow around the point of interest, in which $\mathbf{R}$ and $\boldsymbol{\omega}$ are zero. In that case, distance vector $\mathbf{d}$ does not change in time, meaning that rigid-like rotation expressed by antisymmetric tensor is not a source of deformation.

The strain-rate tensor $\mathbf{E}$ is instead symmetric, with on- and off-diagonal terms. Diagonal terms represent a stretching along their respective axes, while off-diagonal ones are related to shear deformations involving two coordinates at a time. An interesting point is that $\mathbf{E}$ cannot disappear, even choosing accurately the frame of reference, as happens instead to $\mathbf{R}$. It exists, in fact, an invariant that is $tr(\mathbf{E}) = \nabla \cdot \mathbf{v}$ which does not depend on the frame of reference.

The tensor $\mathbf{E}$ can be broken down further as the sum of a diagonal tensor $\mathbf{S}$, which is the spherical part, and a traceless tensor $\mathbf{D}$, that represent a deviatoric tendency [20]. The expression is

$$E_{ij} = S_{ij} + D_{ij} = \left[\frac{1}{3} \left(\sum_k \frac{\partial v_k}{\partial x_k} \right) \delta_{ij} \right] + \left[\frac{1}{2} \left(\frac{\partial v_i}{\partial x_j} + \frac{\partial v_j}{\partial x_i} \right) - \frac{1}{3} \left(\sum_k \frac{\partial v_k}{\partial x_k} \right) \delta_{ij} \right] \tag{1.11}$$

We are simply separating the spherical expansion-contraction effect of $\mathbf{S}$ (denoting a divergence different from zero) and the shear-deviatorical effect of $\mathbf{D}$, that does not alter the fluid parcel volume. Imaging to describe an incompressible fluid, we will have $S_{ij} = 0$ and $E_{ij} = D_{ij}$.

In particular, the deformation of a piece of incompressible fluid becomes very simple in a frame of reference aligned with the principal axes of the $\mathbf{D}$ tensor. In these new coordinates, the deviatoric tensor can be expressed as

$$\bar{\mathbf{D}} = \begin{pmatrix} \bar{D}_{11} & 0 & 0 \\ 0 & \bar{D}_{22} & 0 \\ 0 & 0 & \bar{D}_{33} \end{pmatrix}, \qquad \text{with } \bar{D}_{11} + \bar{D}_{22} + \bar{D}_{33} = 0 \tag{1.12}$$

An example of velocity field, displaying such kind of diagonalized strain-rate tensor, is the 3D stagnation point flow

$$\begin{cases} v_x = ax \\ v_y = by \ , \\ v_z = cz \end{cases} \qquad \text{with } a+b+c=0 \tag{1.13}$$

that is suitable for modelling the dynamic of a patch of incompressible fluid in time.

1.2 Planktonic ecosystems

1.2.1 Plankton in general

Plankton represent a wide variety of microscopic organisms that float or drift in the ocean or other bodies of water, unable to swim against the current. They form the base of the marine food web and play a crucial role in marine ecosystems and global biogeochemical cycles. Plankton are extremely diverse in form and function, ranging in size from one to several hundred microns [35]. Their classification into different trophic groups is based on their feeding strategies and ecological roles. The two main ones are phytoplankton and zooplankton, representing autotroph and heterotroph organisms respectively.

Phytoplankton are in general microalgae that perform photosynthesis, converting inorganic carbon dioxide (CO_2) and water (H_2O) into organic compounds, exploiting the sunlight. They produce indeed chlorophyll and other pigments, and they are confined to live in near-surface waters, at a maximum depth of around 100 m. The main families of phytoplankton organisms are [3]

- Diatoms: they are characterized by their intricate silica cell walls, which give them a distinctive glass-like appearance. They are among the most abundant and ecologically significant phytoplankton in the ocean, well known for their capacity to form immense blooms in spring.
- Dinoflagellates: they are characterized by the presence of two flagella that enable vertical motion. Some species display bioluminescence, while others can produce virulent neurotoxins.
- Coccolithophores: they are characterized by their calcium carbonate plates and play a significant role in global carbon calcification.
- Cyanobacteria: they play a unique role in the nutrient-depleted waters of the open oceans, converting inert atmospheric nitrogen (N_2) into organic forms that can serve as nutrients.

Zooplankton are a diverse group of small, heterotrophic organisms that drift in aquatic environments, feeding mainly on phytoplankton. They are primary consumers, often referred to as grazers, transferring energy and nutrients to higher trophic levels. Crustacea, which display chitin exoskeletons, typically dominate zooplankton communities. Other significant species include cnidarians, typically characterized by their gelatinous bodies and stinging tentacles [3].

1.2.2 Phytoplankton and Primary production

Primary production refers to the process by which living organisms produce and store chemical energy in the form of organic compounds. The main source of this energy is sunlight, but a minute fraction of primary production is driven by lithotrophic organisms using the chemical energy of inorganic molecules. Photosynthesis, in particular, takes inorganic carbon dioxide (CO_2) and water (H_2O) to synthesize simple organic molecules like glucose and other sugars.

$$6CO_2 + 6H_2O + \text{Energy} \rightarrow C_6H_{12}O_6 + 6O_2 \tag{1.14}$$

The latter may be further used to obtain more complicated molecules, including proteins, complex carbohydrates, lipids, and nucleic acids, or be respired to perform work. The energy stored in these compounds reaches higher trophic levels through grazing by heterotrophic organisms, fueling all oceanic living systems [7].

Phytoplankton play a central role in primary production, being the principal autotrophic organism in the ocean. They rely on elements such as carbon, nitrogen, phosphorus, sulfur, and iron to synthesize important organic compounds. When phytoplankton die, their organic matter undergoes various processes, including viral infection, predation, and sinking into deeper ocean layers. This leads to the formation of particulate and dissolved organic detritus, which is subsequently decomposed and respired by heterotrophic organisms like zooplankton and bacteria. This process, called the biological pump, enhances the carbon stored in the deep ocean, complementing the solubility pump, which primarily relies on the reactivity of carbon dioxide in seawater [35].

1.2.3 Limiting factors

The growth of phytoplankton, like any other organism, is subject to various limiting factors that can affect their productivity.

Light intensity Primary production increases with the incidence of photons at low light levels but saturates at high levels, like in an enzymatic reaction. Phytoplankton adjusts chlorophyll concentration to optimize light harvesting, producing higher concentrations in low-light conditions and reducing it in intense light conditions. In the latter situation, photo-protection pigments may be produced to dissipate excess energy and protect the cell, but this can slow down photosynthesis and population growth [35].

Temperature Within certain limits, an increase in temperature promotes metabolic processes, so a higher temperature generally corresponds to increased phytoplankton biomass production [35]. Temperature also influences other important factors for phytoplankton, such as oxygen solubility and water mass movements, to which plankton is inherently linked by definition.

Nutrients availability The major chemical factors that control the phytoplankton productivity in any type of aquatic ecosystem are carbon (C), nitrogen (N), phosphorus (P) and silica (Si), but other elements like iron (Fe) can become critical in specific environments. Carbon is the main element that regulates the functioning of natural waters because of the intricate equilibrium that exists between CO_2, bicarbonate and carbonate that determine the presence of acidity or alkalinity. Moreover, it is the central building block of all the organic compounds, and so is required in maximum quantity by photosynthetic organisms [27]. Nitrogen is primarily utilized by phytoplankton in order to synthesize proteins, enzymes, and chlorophyll, which are essential for their growth, photosynthesis, and overall physiological functions. Scarcity of this element, in the past, was regarded as the main limiting factor for abundance. However, other chemical factors like phosphorus are important for specific species of phytoplankton, which flourish under nanomolar phosphorus concentrations. Phosphorus is a crucial component of adenosine triphosphate (ATP) and a key part of nucleic acids. Silica is instead needed in small quantity, mainly for protein synthesis.

Stratification Differences in temperature, salinity, or density between water masses can cause the stratification of different water layers. This stratification can impact phytoplankton in various ways, particularly by influencing the availability of nutrients and light. Often, nutrients like nitrogen and phosphorus can become concentrated in deeper layers due to limited vertical mixing, but depleted in

the euphotic zone. Turbidity of the upper layers of the water column can also act as an important regulator of the light availability in deeper layers [27].

1.2.4 Liebig's law

Liebig's Law of the Minimum, proposed by German chemist Justus von Liebig in the 19th century, states that the growth of the organisms is controlled not by the total amount of resources available, but by the scarcest resource, often referred to as the limiting factor. In other words, the growth of an organism or population is determined by the resource that is available in the lowest amount relative to the organism's requirements.

For instance, imaging to model the growth of a population $\mathcal{N}$ which depend on a set of resources $\{\mathcal{R}_i\}$, one can mathematically define Liebig's Law as

$$\nu_{\mathcal{N}}(\{\mathcal{R}_i\}) = \min_i \left(\nu_i \frac{\mathcal{R}_i}{\mathcal{R}_i + k_i} \right) \tag{1.15}$$

where $\nu_{\mathcal{N}}$ is the effective growth rate of the population $\mathcal{N}$ and the right-hand side is the minimum between all the Michaelis-Menten kinetic terms, representing uptake rates of all the different resources $\{\mathcal{R}_i\}$.

This principle is valid also for phytoplankton growth, meaning that the net growth rate will depend only on the limiting nutrient present in the specific region of the ocean we are considering. For example, if a phytoplankton species requires both nitrogen and phosphorus for growth, but nitrogen is available in lower concentrations than phosphorus, then nitrogen becomes the limiting factor. Increasing phosphorus availability will not enhance phytoplankton growth unless nitrogen is also supplied in sufficient quantities.

Even if, in the recent literature, limitations of Liebig's Law have been longly discussed and ascertained [30], [14] in this work we will adopt this concept to limit the number of important nutrients necessary for phytoplankton growth.

1.2.5 Redfield ratio

The Redfield ratio is a fundamental concept in marine biogeochemistry that describes the stoichiometric ratio of elements in phytoplankton and their role in the marine carbon cycle. It was first proposed by American oceanographer Alfred C. Redfield in the 1930s, based on his analysis of nutrient data from various oceanic regions.

The Redfield ratio specifically refers to the molar ratio of carbon (C), nitrogen (N), and phosphorus (P) in phytoplankton biomass, which is approximately 106 C: 16 N : 1 P, respectively. In other words, for every 106 atoms of carbon, phytoplankton require approximately 16 atoms of nitrogen and 1 atom of phosphorus.

The main discovery is that the Redfield ratio exists not only within living organisms, but also in the composition of the ocean itself. In other words, vast ocean chemistry is perfectly suited to the requirements of living organisms [35]. The mechanism generating these proportions between the elements is not completely clear, even if probably related to cellular growth stoichiometry. It's important to specify that there is some variability in nutrient ratios due to different nutrient cycles, and this leads to departures from the canonical Redfield values in some areas.

An extension that can be useful to consider in our work is the Redfield ratio with iron, which provides 106 C : 16 N : 1 P : 0.0075 Fe. [6].

1.3 Ocean carbon dynamic

1.3.1 Forms of carbon

Carbon exists in various forms within aquatic ecosystems, each playing a distinct role in biogeochemical cycling and ecosystem dynamics. Here's an overview of the different forms of carbon, starting from total carbon (TC) to dissolved and particulate organic and inorganic carbon [35]

- Total carbon (TC): refers to the sum of all carbon-containing compounds present in a sample or ecosystem. It includes both organic and inorganic carbon compounds in dissolved, particulate, and gaseous forms.
- Dissolved inorganic carbon (DIC): comprises carbon dioxide, carbonic acid, bicarbonate ions, and carbonate ions dissolved in water. These compounds are inorganic and can be directly measured in seawater or freshwater samples.
- Dissolved organic carbon (DOC): consists of organic carbon compounds that are dissolved in water. These compounds originate from the decomposition of organic matter, such as dead organisms, plant material, and microbial byproducts. DOC is a crucial component of aquatic ecosystems, serving as a substrate for microbial activity and nutrient cycling.
- Particulate organic carbon (POC): refers to organic carbon compounds that are associated with particulate matter suspended in water. This includes living organisms, such as phytoplankton and zooplankton, as well as detritus and organic particles derived from decaying organic matter. It serves as a source of energy and carbon for heterotrophic organisms.
- Particulate inorganic carbon (PIC): comprises inorganic carbon compounds that are associated with particulate matter in aquatic environments. This may include calcium carbonate (CaCO3) shells and skeletons of marine organisms like coccolithophores. PIC contributes to carbonate sedimentation and plays a role in the global carbon cycle.

In particular, we are interested in the role of dissolved inorganic carbon (DIC) and its relationship with carbon dioxide. The equation defining the DIC molar concentration is

$$DIC = [CO_2^*] + [HCO_3^-] + [CO_3^{2-}] \tag{1.16}$$

where CO_2^* includes the aqueous form of carbon dioxide, CO_2^{aq}, and carbonic acid, H_2CO_3.

The majority of carbon dioxide in the ocean is transformed into bicarbonate and carbonate ions, with approximately 90% of DIC consisting of bicarbonate ions, around 9% as carbonate ions, and a small fraction, up to 1%, remaining as dissolved carbon dioxide. As a result of this transformation, the ocean holds a significantly larger amount of carbon compared to the atmosphere, approximately 50 times more. The inorganic carbon stored in the ocean is approximately 40 times greater than the amount of organic carbon present [35].

1.3.2 CO_2 partial pressure

Carbon dioxide molecules continuously move across the interface between the air and sea, resulting in gas fluxes that go inward and outward of the water. When the flux in each direction is equal, the concentrations of CO_2 in the air and water are in equilibrium. The abundance of carbon dioxide in the surface atmosphere is quantified in terms of partial pressure, denoted as pCO_2^{atm}, which represents the pressure exerted by CO_2 gas at the Earth's surface [35].

Seawater also has an effective partial pressure of carbon dioxide, denoted simply as pCO_2, which represents the partial pressure that CO_2 would reach in the atmosphere if equilibrium were established with the concentration of dissolved carbon dioxide, $[CO_2^*]$, in surface water. The ratio between $[CO_2^*]$

and the effective partial pressure, pCO_2, is determined by the solubility coefficient, denoted as K_o, which is defined as

$$K_o = \frac{[\mathrm{CO}_2^*]}{pCO_2} \tag{1.17}$$

The solubility coefficient indicates how efficient are molecules in moving into and out of the water, and is influenced by environmental conditions such as temperature and salinity.

The air–sea flux of the carbon dioxide in a disequilibrium scenario can be written in terms of the difference between atmospheric and water partial pressures of CO_2, as

$$F_{CO_2} = \rho K_o K_g (pCO_2 - pCO_2^{atm}) = \rho K_o K_g \Delta p \tag{1.18}$$

where ρ is the water density, K_o CO_2 solubility in water and K_g represent the gas transfer velocity, depending strongly on the wind speed above the considered oceanic surface.

Another approach to characterize the imbalance between the surface ocean and atmospheric carbon reservoirs is to subdivide dissolved inorganic carbon (DIC) into "saturation" C_{sat} and "disequilibrium" ΔC components:

$$DIC = C_{sat} + \Delta C \tag{1.19}$$

C_{sat} is the concentration of dissolved inorganic carbon that the surface ocean would have if $pCO_2 = pCO_2^{atm}$.

1.3.3 Revelle Buffer factor

The chemical buffering of anthropogenic CO_2 represents the most significant oceanic process acting as a carbon sink [24]. Practically, carbon dioxide entering the ocean is converted mainly into bicarbonate and carbonate ions, so that the resulting increase in gaseous seawater CO_2 concentration is smaller than the amount of CO_2 added per unit of seawater. This mechanism is quantified by the Revelle buffer factor B, which express the relationship between fractional changes in pCO_2 and DIC after re-equilibrating. The explicit definition is

$$B = \frac{\Delta p}{pCO_2} \Big/ \frac{\Delta C}{C_{sat}} \simeq const. \tag{1.20}$$

In reality, Revelle buffer factor is not constant and increase with water pCO_2, as shown in Fig. 1.1. The assumption that one makes is usually that water pCO_2 is very near to the equilibrium with the atmospheric one ($pCO_2 \sim pCO_2^{atm}$), and so nearly constant and uniform for the spatio-temporal scales of interest.

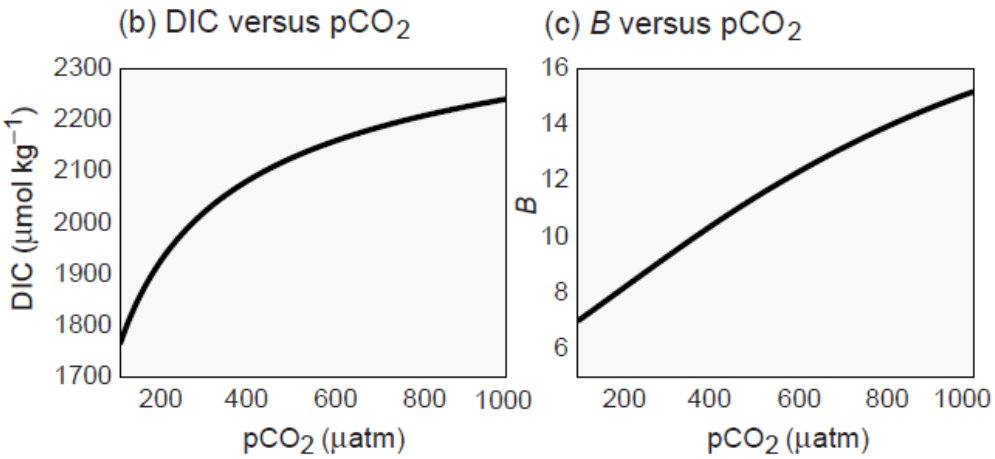

Figure 1.1: Dissolved inorganic carbon (DIC) and Revelle buffer factor (B) relationships with the water CO_2 partial pressure pCO_2 [35].

Chapter 2

Simple phytoplankton CR model

The dynamics of phytoplankton populations have been extensively investigated to elucidate intriguing phenomena, such as seasonal blooms, eutrophication and the ecological diversity role on productivity.

First, let's start with a simple model of an open ocean ecosystem that is inspired by [10]. A patch of water (at the surface or at a given depth) contains phytoplankton and limiting nutrient with mean concentrations P and N, while the surrounding acts like a reservoir and displays fixed mean concentrations P_{out} and N_{out}. With respect to [10], we are modelling an external space which is not necessarily located below the patch, but could more generally represent the rest of water ocean in ecological equilibrium.

Focusing on what happens inside the water patch, we can imagine a Consumer-Resource dynamics taking place, where phytoplankton exploits the available amount of nutrient to grow. The coupled system of equations describing this phenomenon are

$$\begin{cases} \dfrac{dN(t)}{dt} = -\nu \dfrac{N(t)}{N(t)+k} P(t) + \Omega(N_{out} - N(t)) \\ \dfrac{dP(t)}{dt} = \nu \dfrac{N(t)}{N(t)+k} P(t) - mP(t) + \Omega(P_{out} - P(t)) \end{cases} \tag{2.1}$$

In the first one, the nutrient N is eaten at a rate that involves Michaelis–Menten kinetics, with maximum growth rate ν and half-saturation constant k. Here, we assume that the rate of nutrient uptake is constrained by a maximum saturation level, while the nutrient cannot regenerate by itself. The only source of new nutrient is coming from the outside, with a rate given by the product of an entrainment rate Ω and the difference between external and inner concentrations.

In the second equation, nutrient depletion is converted into phytoplankton growth (there is no loss of mass). Then, processes of grazing and degradation are collected into the phytoplankton mortality rate m. The last term provides phytoplankton exchange between our small system and the reservoir, depending again on Ω.

2.1 Stationary points analysis

Equilibrium for this kind of system can be characterized depending on ν, k, m, Ω, N_{out} and P_{out}. Let's start, for simplicity, with the case in which P_{out} is set to zero, meaning that there's no phytoplankton in the reservoir. Then, we will consider also $P_{out} > 0$ as general case.

2.1.1 $P_{out} = 0$

Stationary conditions can be rearranged as:

$$\begin{cases} 0 = -\nu \dfrac{N^*}{N^* + k} P^* + \Omega(N_{out} - N^*) \\ 0 = \left(\nu \dfrac{N^*}{N^* + k} - m - \Omega \right) P^* \end{cases} \tag{2.2}$$

It is easy to show that there are two stationary points, the first is trivial and describes absence of life, while the second admits persistent phytoplankton fed by entrainment of outside nutrient:

$$(N^*_{trivial}, P^*_{trivial}) = (N_{out}, 0) \tag{2.3}$$

$$(N^*, P^*) = \left(\frac{(m + \Omega)k}{\nu - (m + \Omega)}, \frac{\Omega N_{out}}{m + \Omega} - \frac{\Omega k}{\nu - (m + \Omega)} \right) \tag{2.4}$$

Once set the feasibility conditions

$$\nu > m + \Omega, \qquad N_{out} > N^*(\nu, k, m, \Omega) \tag{2.5}$$

one can demonstrate that the trivial stationary point is unstable, while the one with phytoplankton is stable [10]. If the second feasibility condition is not met, one would have the opposite.

In summary, presence of persistent phytoplankton inside the water patch is allowed only if N_{out} is sufficiently high to counterbalance the loss of nutrient taken away for the growth.

2.1.2 $P_{out} > 0$

Similar results can be obtained in the case $P_{out} > 0$, even if the expressions involved are more complex. Stationary conditions become now

$$\begin{cases} 0 = -\nu \dfrac{N^*}{N^* + k} P^* + \Omega(N_{out} - N^*) \\ 0 = \nu \dfrac{N^*}{N^* + k} P^* - m P^* + \Omega(P_{out} - P^*) \end{cases} \tag{2.6}$$

and they can be rewritten, after some manipulations, into

$$\begin{cases} A N^{*2} + B N^* + C = 0 \\ P^*(N^*) = \dfrac{\Omega(N_{out} - N^*)}{\nu \frac{N^*}{N^* + k}} \end{cases} \tag{2.7}$$

where

$$A = -(\nu - (m + \Omega)) \tag{2.8}$$

$$B = [\nu(N_{out} + P_{out}) + (m + \Omega)(k - N_{out})] \tag{2.9}$$

$$C = -(m + \Omega)kN_{out} \tag{2.10}$$

This system will have two pairs of solutions if $\Delta = B^2 - 4AC > 0$, and this is proven to be guaranteed for every value of the parameters involved. Let's define

$$N^*_{(1)} = \frac{-B + \sqrt{B^2 - 4AC}}{2A} \tag{2.11}$$

$$N^*_{(2)} = \frac{-B - \sqrt{B^2 - 4AC}}{2A} \tag{2.12}$$

From Cartesio's rule, we can predict the signs of $N^*_{(1)}$ and $N^*_{(2)}$. There are two cases:

- $\nu > m + \Omega$ both solutions are positive
- $\nu < m + \Omega$ only one solution is positive

First case Since the sign of $P^*(N^*)$ is completely determined by the one of $N_{out} - N^*$, it would be useful to reexpress the quadratic equation in (2.7) with respect to the quantity $\Delta N^* = N^* - N_{out}$. This would lead to the following relations

$$\begin{cases} A'\Delta N^{*2} + B'\Delta N^* + C' = 0 \\ P^*(\Delta N^*) = \dfrac{-\Omega\Delta N^*}{\nu\frac{N_{out}+\Delta N^*}{N_{out}+\Delta N^*+k}} \end{cases} \tag{2.13}$$

where

$$A' = A = -(\nu - (m + \Omega)) \tag{2.14}$$

$$B' = [\nu(P_{out} - N_{out}) + (m + \Omega)(k + N_{out})] \tag{2.15}$$

$$C' = \nu N_{out} P_{out} \tag{2.16}$$

We are guaranteed that Δ remains the same in the transformation between (2.7) and (2.13), so, again, two distinct solutions $\Delta N^*_{(1)} = N^*_{(1)} - N_{out}$ and $\Delta N^*_{(2)} = N^*_{(2)} - N_{out}$ will be present (Fig 2.1). This time, from Cartesio's rule, we expected that they will have opposite sign independently on the sign of B'. One can show that $\Delta N^*_{(1)} < 0$ and $\Delta N^*_{(2)} > 0$, so the only acceptable solution for (2.13), satisfying the feasibility condition $P^*(\Delta N^*) \geq 0$, is $\Delta N^*_{(1)}$. This automatically entails that the couple $(N^*_{(1)}, P^*_{(1)})$ is the only feasible in our biological system.

Second case Since $N^*_{(1)} > 0$ and $N^*_{(2)} < 0$, the second solution is discarded. We can demonstrate, applying again Cartesio's rule on (2.13), that $\Delta N^*_{(1)} < 0$, which satisfies again the feasibility condition $P^*(\Delta N^*) \geq 0$ (Fig 2.2). Consequently, also in this case, the couple $(N^*_{(1)}, P^*_{(1)})$ is the only feasible.

In summary, in the case $P_{out} > 0$, it is not necessary to assume $\nu > m + \Omega$ to have coexistence, because P^* cannot be zero in presence of an external source. Anyway, for very low value of the growth rate ν, the stationary phytoplankton concentration is very close to be absent.

Unfortunately, the expressions for $N^*_{(1)}$ and $P^*_{(1)}$ in terms of ν, k, m, Ω, N_{out} and P_{out} are quite complicated to write, so the stability analysis is not trivial and will not be performed analytically. Despite that, one can show that simulations converge towards $(N^*_{(1)}, P^*_{(1)})$ for every feasible choice of the initial conditions.

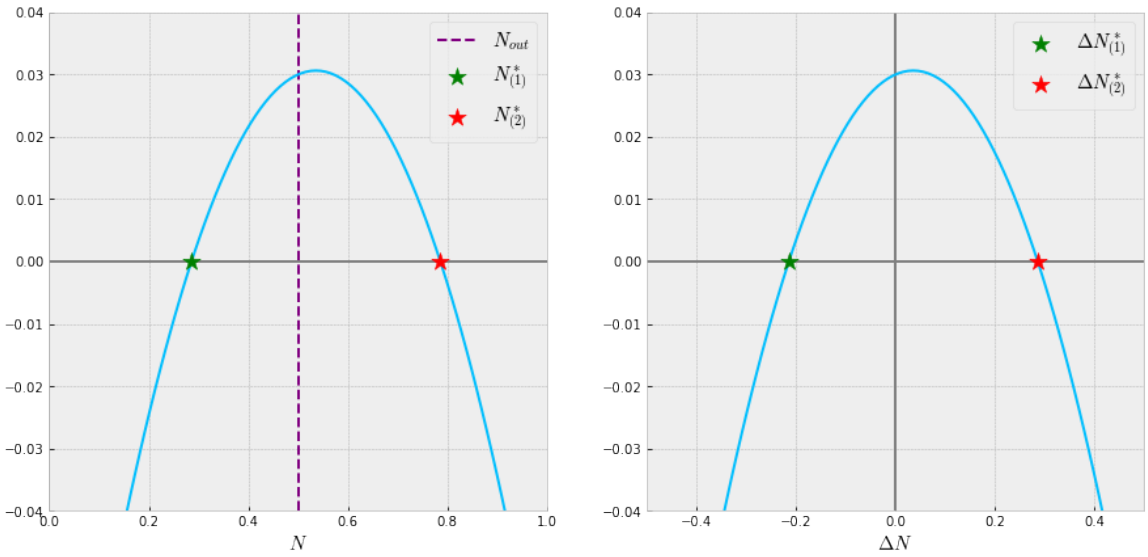

Figure 2.1: Quadratic equation solutions of (2.7) and (2.13), in the case $\nu > m + \Omega$. Values of the model parameters are $\nu = 0.6$, $m = 0.05$, $k = 2$, $\Omega = 0.06$, $N_{out} = 0.5$, $P_{out} = 0.1$. $\Delta N^*_{(1)}$ is negative, satisfying feasibility condition.

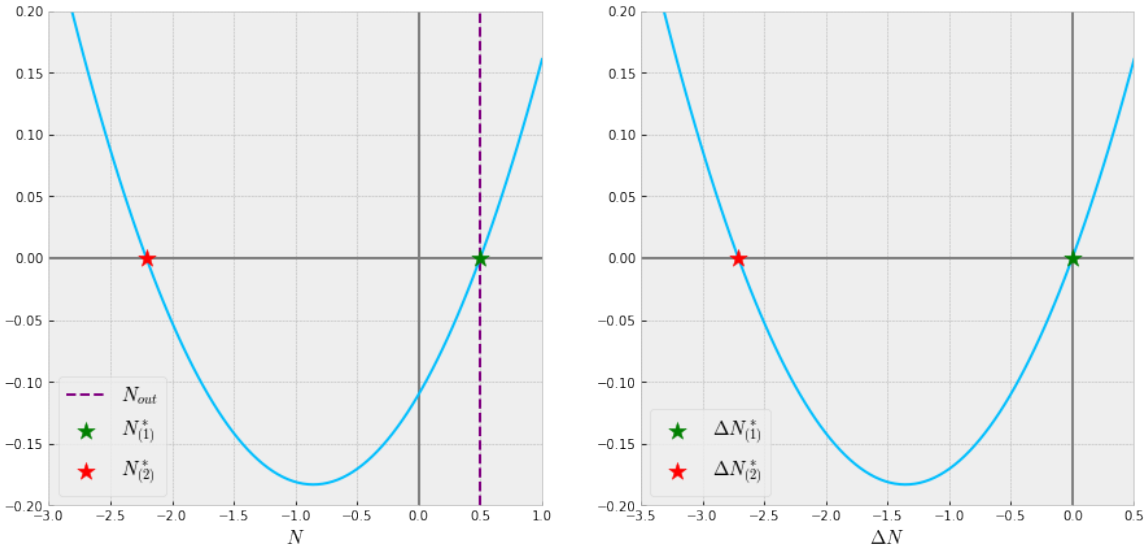

Figure 2.2: Quadratic equation solutions of (2.7) and (2.13), in the case $\nu < m + \Omega$. Values of the model parameters are $\nu = 0.01$, $m = 0.05$, $k = 2$, $\Omega = 0.06$, $N_{out} = 0.5$, $P_{out} = 0.1$. In this case $\Delta N^*_{(1)}$ is very close to zero, but still negative.

Chapter 3

Lagrangian water patch dynamic

In this Chapter we study the evolution of a three-dimensional patch of water in the ocean under the effect of advection, stirring and diffusion. We characterize its shape in terms of spatial variances in each direction, using a Gaussian approximation. The interaction between the water patch and the current velocity field into which it is immersed is analyzed through an advection-diffusion equation. The shaping mechanisms determine a change in the patch characteristic sizes, in particular effective diffusion leads to an increase of the volume occupied. The enlargement rate of the water patch is finally linked to the entrainment rate of diverse water coming from the surrounding, which tend to dilute the patch composition.

3.1 Three stages tracer dispersal

The analysis of tracer dispersal in the ocean is tackled in classical theory from the prospective of simple diffusive and advective processes, which lack on describing shear and strain at difference scales. In a turbulent media, the problem is a way more complex and requires making some distinction between dispersal phases. In [12] three different stages are considered:

1. When the scale of the patch is smaller than the one of the straining velocity field, stirring can be neglected and the velocity field acts like an effective diffusion process [12]. Thus, the area grows approximately linearly in time.
2. When the scale of the patch is of the order of the straining velocity field, the patch begins to be advected into long, thin streaks. Their length grows exponentially in time.
3. When the scale of the patch is bigger than the one of the straining velocity field, streaks start to wrap around the eddies formations, mixing eventually the tracer. We can interpret this stage as diffusive again.

This qualitative description finds confirmation in experiments like NATRE [29], where the dispersal of a passive tracer in the North Atlantic is considered (Fig. 3.1). In particular, streaks formation and size evolution, related to the second phase, can be formalized in the following sections.

3.2 Ellipsoid approximation

Let's image to have an initial tracer distribution (Fig. 3.2) made of a single patch centered in $\mathbf{X}(t_0) = (x_0, y_0, z_0)$ that can be considered approximately Gaussian, due to the initial effective diffusion phase. Iso-surfaces of this three-dimensional distribution are described by ellipsoids, whose axes are assumed

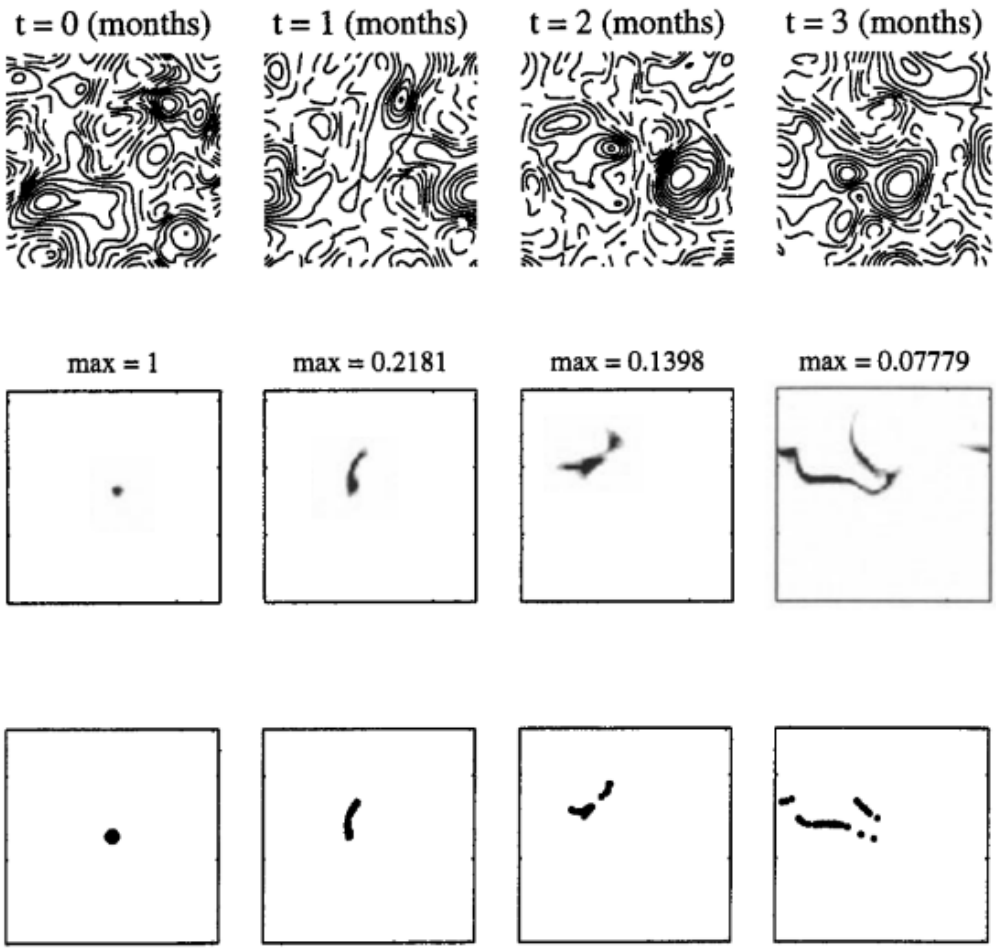

Figure 3.1: Different phases of a tracer dispersal [29]. At the beginning, the patch is circular. Then, it elongates in one direction until multiple merging streaks appear.

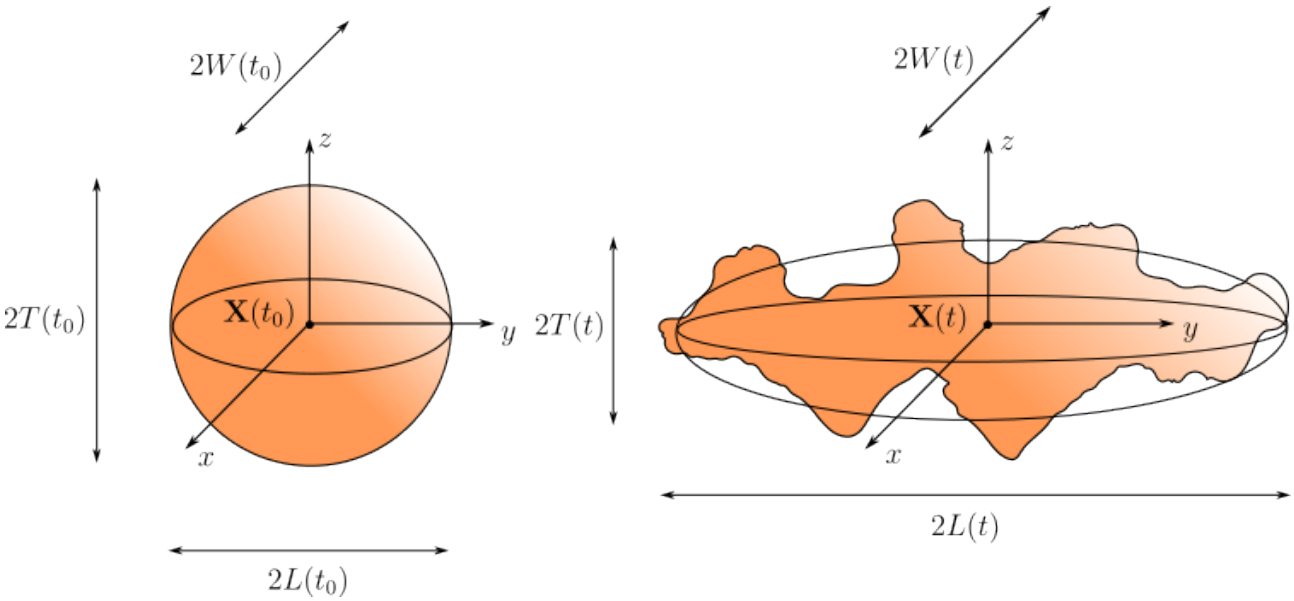

Figure 3.2: The evolution of a Lagrangian patch, starting from the beginning of the second phase of dispersal, at instant t_0, and affected by stirring on the y direction. At time t, the Lagrangian patch has not anymore a symmetric shape, but can be approximated by the ellipsoid containing the majority of its volume. We keep track of the ellipsoid semi-axes, that are width $W(t)$, length $L(t)$ and thickness $T(t)$.

to be aligned with horizontal and vertical directions. Let's define patch width $W(t)$, length $L(t)$ and thickness $T(t)$ as characteristic lengths that incorporates a major part of the tracer inside them. They can be expressed as multiples of the 3D Gaussian standard deviations $\sigma_x(t)$, $\sigma_y(t)$ and $\sigma_z(t)$. A common choice is to set $W(t) = \sigma_x(t)$, $L(t) = \sigma_y(t)$ and $T(t) = \sigma_z(t)$, although this prescription includes only a restricted part of the tracer "mass" inside such ellipsoid. Its volume would be

$$V(t) = \frac{4\pi}{3} W(t)L(t)T(t) \tag{3.1}$$

while the horizontal projected area

$$A(t) = \pi W(t)L(t) \tag{3.2}$$

This holds in the assumption that the patch is localized at a given depth such that boundaries conditions (e.g. sea surface) are not meaningful.

3.3 Sources of deformation

Following a Lagrangian approach, we want to describe now how the oceanic flow alters the position and the shape of the tracer patch. Conceptually, all rigid-like movement such pure advection and rotation can be absorbed into the motion of the local frame of reference, that we can set to be centered in $\mathbf{X}(t)$ and oriented along ellipsoid principal axes $\hat{\mathbf{w}}(t)$, $\hat{\mathbf{l}}(t)$ and $\hat{\mathbf{t}}(t)$. This means that the coordinate system that will be adopted from now will have x, y and z axes which are aligned to $\hat{\mathbf{w}}(t)$, $\hat{\mathbf{l}}(t)$ and $\hat{\mathbf{t}}(t)$.

Patch shape modification can be caused by by horizontal stirring, divergence and diffusion. The first two can be modeled through the local velocity field $\mathbf{v}(\mathbf{x}, t)$ acting on the tracer patch, which can be approximated, at first order, to a 3D stagnation point flow:

$$\mathbf{v}(\mathbf{x},t) = \left(\left(-\gamma(t) + \frac{\delta(t)}{2}\right)x; \quad \left(+\gamma(t) + \frac{\delta(t)}{2}\right)y; \quad -\delta(t)z\right) \tag{3.3}$$

Here we are assuming that horizontal stirring acts along the y direction, which is aligned with the $\hat{\mathbf{l}}$ axis. The quantities $\gamma(t)$ and $\delta(t)$ represent time dependent horizontal strain and divergence rates respectively, in a way that vertical dimension dynamic is independent of the horizontal one. This is done since horizontal and vertical motions in the ocean are often driven by different processes and span different spatio-temporal scales [12]. Moreover, this stagnation flow displays a field divergence $\nabla \cdot \mathbf{v}$ that is equal to zero, since we are describing a fluid that can be assumed incompressible.

Diffusion contribution tends to enlarge the patch, diluting its content with the outside. We again distinct between time dependent horizontal and vertical diffusivity $\kappa^h(t)$ and $\kappa^v(t)$, since they are order of magnitude different [13]. The diffusion that we are treating here represent unresolved scales of the velocity field, typically much smaller than the patch characteristic size.

Fluid dynamical parameters scaling The temporal dependence of strain, divergence and diffusivities is a shorthand notation to indicate, more properly, a system size dependence. The extension of the Lagrangian patch, indeed, varies with time and can be quantitatively measured by horizontal and vertical characteristic sizes, denoted as $S^h(t)$ and $S^v(t)$. These quantities can be expressed in terms of width $W(t)$, length $L(t)$ and thickness $T(t)$ of the patch

$$\begin{aligned} S^h(t) &= W(t) + L(t) \\ S^v(t) &= 2T(t) \end{aligned} \tag{3.4}$$

Following some approaches that have been found in literature [26], [9], we assume that fluid dynamical parameters scale with horizontal and vertical characteristic sizes as

$$\begin{aligned} \gamma(S^h(t), S^v(t)) &= \gamma_0 \cdot \left(\frac{S^h(t)}{S^h(0)}\right)^{-\frac{2}{3}} \\ \delta(S^h(t), S^v(t)) &= \delta_0 \\ \kappa^h(S^h(t), S^v(t)) &= \kappa^h_0 \cdot \left(\frac{S^h(t)}{S^h(0)}\right) \\ \kappa^v(S^h(t), S^v(t)) &= \kappa^v_0 \cdot \left(\frac{S^v(t)}{S^v(0)}\right) \end{aligned} \tag{3.5}$$

3.4 Advection-diffusion equation

In the Lagrangian frame of reference, the effects of the aforementioned strain, divergence and diffusion can be joined into an advection-diffusion equation of the patch distribution $\theta(\mathbf{x},t)$:

$$\frac{\partial\theta(\mathbf{x},t)}{\partial t} + \mathbf{v}(\mathbf{x},t)\cdot\nabla\theta(\mathbf{x},t) = \kappa^h(t)\left(\frac{\partial^2\theta(\mathbf{x},t)}{\partial x^2} + \frac{\partial^2\theta(\mathbf{x},t)}{\partial y^2}\right) + \kappa^v(t)\frac{\partial^2\theta(\mathbf{x},t)}{\partial z^2} \tag{3.6}$$

This description is quite general, since it does not assume a specific shape for $\theta(\mathbf{x},t)$ and only requires differentiability in space. Inserting the local velocity field of equation (3.3) inside (3.6), one gets

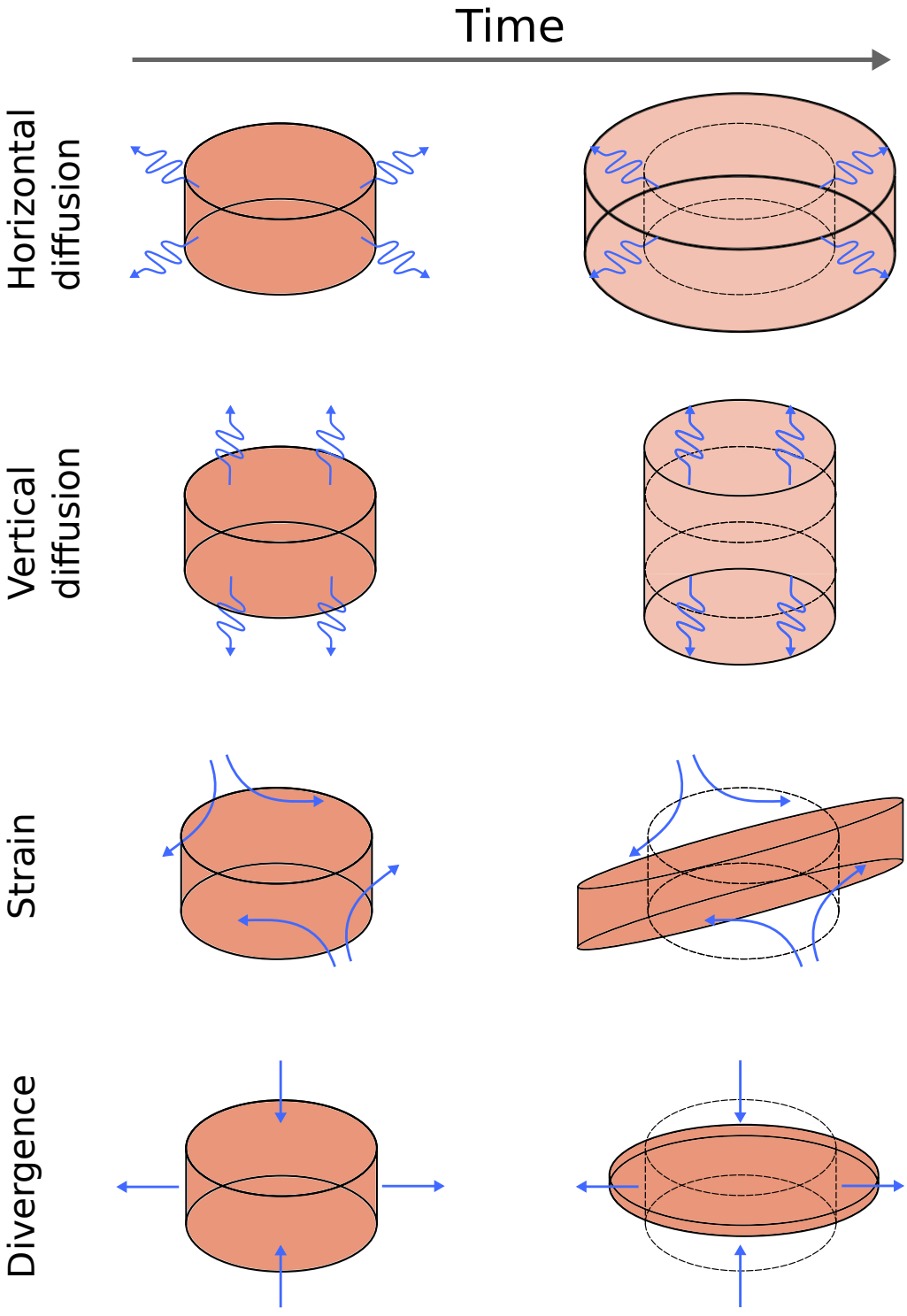

Figure 3.3: Effects of horizontal and vertical diffusion, strain and divergence on the Lagrangian patch [28]. In order to make the image more comprehensible, in place of the ellipsoid we depicted the circumscribed cylinder. Diffusion in both directions increase the volume of the patch by diluting its content, while strain and divergence simply stretch the patch on different axes.

$$\frac{\partial\theta}{\partial t}+\left(-\gamma(t)+\frac{\delta(t)}{2}\right)x\frac{\partial\theta}{\partial x}+\left(\gamma(t)+\frac{\delta(t)}{2}\right)y\frac{\partial\theta}{\partial y}-\delta(t)z\frac{\partial\theta}{\partial z}=\kappa^h(t)\left(\frac{\partial^2\theta}{\partial x^2}+\frac{\partial^2\theta}{\partial y^2}\right)+\kappa^v(t)\frac{\partial^2\theta}{\partial z^2} \quad (3.7)$$

This is a partial differential equation involving four time-dependent parameters: $\gamma(t)$, $\delta(t)$, $\kappa^h(t)$ and $\kappa^v(t)$. An analytic solution for $\theta(\mathbf{x},t)$ can be found only for the Gaussian approximation [29], while, more in general, other relationship between patch distribution moments can be found to hold.

3.5 Variances dynamic

What we want to understand now is how the characteristic size of the patch distribution evolves in time due to the presence of these "shaping" mechanism (strain, divergence and diffusion). Reminding the Gaussian example, standard deviations σ_x, σ_y and σ_z represent a good proxy of the patch size. Let's indeed find the spatial variances that can be computed as

$$\begin{aligned}\sigma_x^2(t)&=\frac{M_2^x(t)}{M_0^x(t)}\\ \sigma_y^2(t)&=\frac{M_2^y(t)}{M_0^y(t)}\\ \sigma_z^2(t)&=\frac{M_2^z(t)}{M_0^z(t)}\end{aligned} \quad (3.8)$$

where the time-dependent zeroth and second moments of the patch distribution are defined as

$$\begin{aligned}M_0^x(t)&=\int\theta(\mathbf{x},t)\Big|_{y,z=0}dx \quad ; \quad M_2^x(t)=\int x^2\theta(\mathbf{x},t)\Big|_{y,z=0}dx\\ M_0^y(t)&=\int\theta(\mathbf{x},t)\Big|_{x,z=0}dy \quad ; \quad M_2^y(t)=\int y^2\theta(\mathbf{x},t)\Big|_{x,z=0}dy\\ M_0^z(t)&=\int\theta(\mathbf{x},t)\Big|_{x,y=0}dz \quad ; \quad M_2^z(t)=\int z^2\theta(\mathbf{x},t)\Big|_{x,y=0}dy\end{aligned} \quad (3.9)$$

These integral are computed respectively on the x, y and z axes, so alternately two of three coordinates are set to zero. In particular, the zeroth moments represent just some normalizing quantities which take into account the amount of tracer present on a given axis.

Since explicit computation of the moments would depend on the complete history of the patch distribution itself, one can simply try to characterize their time evolution in a recursive manner. Integrating the advection-diffusion equation (3.7) along the x, y and z axes would allow reexpressing the latter in terms of the zeroth moments, obtaining

$$\begin{aligned}
\frac{dM_0^x(t)}{dt} &= \left(-\gamma(t) + \frac{\delta(t)}{2}\right) M_0^x(t) \\
\frac{dM_0^y(t)}{dt} &= \left(\gamma(t) + \frac{\delta(t)}{2}\right) M_0^y(t) \\
\frac{dM_0^z(t)}{dt} &= -\delta(t) M_0^z(t)
\end{aligned} \tag{3.10}$$

We can see that, depending on the values of $\gamma(t)$ and $\delta(t)$, the zeroth moments would increase or decrease approximately exponentially (rate would depend on integrals $\int_0^t \gamma(t')dt'$ and $\int_0^t \delta(t')dt'$), due to the shape of the local velocity field.

Similarly, multiplying by x^2, y^2, z^2 and integrating along the x, y and z axes equation (3.7) one would get

$$\begin{aligned}
\frac{dM_2^x(t)}{dt} &= +2\kappa^h(t) M_0^x(t) + 3\left(-\gamma(t) + \frac{\delta(t)}{2}\right) M_2^x(t) \\
\frac{dM_2^y(t)}{dt} &= +2\kappa^h(t) M_0^y(t) + 3\left(\gamma(t) + \frac{\delta(t)}{2}\right) M_2^y(t) \\
\frac{dM_2^z(t)}{dt} &= +2\kappa^v(t) M_0^z(t) - 3\delta(t) M_2^z(t)
\end{aligned} \tag{3.11}$$

On the second moments, then, roughly exponential scaling is coupled with the diffusive contribution, which can be linear, sublinear or superlinear depending on diffusivity rates.

At this point, we could exploit equations (3.10) and (3.11) to retrieve the time evolution of the patch spatial variances. In fact, applying derivation chain rule to (3.8)

$$\begin{aligned}
\frac{d\sigma_x^2(t)}{dt} &= \frac{1}{M_0^x(t)}\left(\frac{dM_2^x(t)}{dt} - \sigma_x^2(t)\frac{dM_0^x(t)}{dt}\right) \\
\frac{d\sigma_y^2(t)}{dt} &= \frac{1}{M_0^y(t)}\left(\frac{dM_2^y(t)}{dt} - \sigma_y^2(t)\frac{dM_0^y(t)}{dt}\right) \\
\frac{d\sigma_z^2(t)}{dt} &= \frac{1}{M_0^z(t)}\left(\frac{dM_2^z(t)}{dt} - \sigma_z^2(t)\frac{dM_0^z(t)}{dt}\right)
\end{aligned} \tag{3.12}$$

one would have, finally:

$$\begin{aligned}
\frac{d\sigma_x^2(t)}{dt} &= +2\kappa^h(t) + 2\left(-\gamma(t) + \frac{\delta(t)}{2}\right) \sigma_x^2(t) \\
\frac{d\sigma_y^2(t)}{dt} &= +2\kappa^h(t) + 2\left(\gamma(t) + \frac{\delta(t)}{2}\right) \sigma_y^2(t) \\
\frac{d\sigma_z^2(t)}{dt} &= +2\kappa^v(t) - 2\delta(t)\sigma_z^2(t)
\end{aligned} \tag{3.13}$$

Let's analyze the right-hand side of equations (3.13), where the interplay between diffusivity and strain-divergence plays a crucial role. In all directions, diffusion will tend to increase the spatial variances (as one would expect from stochastic phenomena), while the combinatorial effect of strain and divergence will act roughly exponentially, reducing or feeding variances' increase depending on

the axis. Assuming for simplicity that $\gamma(t) > \delta(t) > 0$, dynamical equilibrium values for $\sigma_x^2(t)$ and $\sigma_z^2(t)$ can be written as

$$\sigma_x^{2*} = \frac{\kappa^h(t)}{\gamma(t) - \frac{\delta(t)}{2}} \tag{3.14}$$

$$\sigma_z^{2*} = \frac{\kappa^v(t)}{\delta(t)} \tag{3.15}$$

3.6 Entrainment rate

Modifications in the spatial variances of $\theta(\mathbf{x}, t)$ imply a change of the patch volume $V(t)$ and projected area $A(t)$, that were defined in (3.1), (3.2). Adopting the convection whereby width, length and thickness of the patch are identified with the standard deviations, equations (3.13) can be reformulated as

$$\begin{aligned}
\frac{dW(t)}{dt} &= +\frac{\kappa^h(t)}{W(t)} + \left(-\gamma(t) + \frac{\delta(t)}{2}\right) W(t) \\
\frac{dL(t)}{dt} &= +\frac{\kappa^h(t)}{L(t)} + \left(\gamma(t) + \frac{\delta(t)}{2}\right) L(t) \\
\frac{dT(t)}{dt} &= +\frac{\kappa^v(t)}{T(t)} - \delta(t) T(t)
\end{aligned} \tag{3.16}$$

and they can be used, together with the derivation chain rule, to retrieve

$$\frac{dV(t)}{dt} = \frac{4\pi}{3}\left[\kappa^h(t)\left(\frac{W^2(t) + L^2(t)}{W(t)L(t)}\right) T(t) + \kappa^v(t)\frac{W(t)L(t)}{T(t)}\right] \tag{3.17}$$

and

$$\frac{dA(t)}{dt} = \pi\left[\kappa^h(t)\left(\frac{W^2(t) + L^2(t)}{W(t)L(t)}\right) + \delta(t)W(t)L(t)\right] \tag{3.18}$$

Notice that the rate of change of $V(t)$ seems to depend only on the diffusive rates $\kappa^h(t)$ and $\kappa^v(t)$, but in reality there is a hidden dependence also on $\gamma(t)$ and $\delta(t)$ that, underneath, determine the values of $W(t)$, $L(t)$ and $T(t)$ through (3.16). From these considerations, one can understand that the volumetric growth for this kind of process is not trivial at all, and that is the product of multiple agents, as strain, divergence and diffusion.

Conceptually, one can subdivide horizontal and vertical components of dV/dt based on the proportionality to the horizontal and vertical diffusivity:

$$\begin{aligned}
\left(\frac{dV(t)}{dt}\right)^h &= \frac{4\pi}{3}\kappa^h(t)\left(\frac{W^2(t) + L^2(t)}{W(t)L(t)}\right) T(t) \\
\left(\frac{dV(t)}{dt}\right)^v &= \frac{4\pi}{3}\kappa^v(t)\frac{W(t)L(t)}{T(t)}
\end{aligned} \tag{3.19}$$

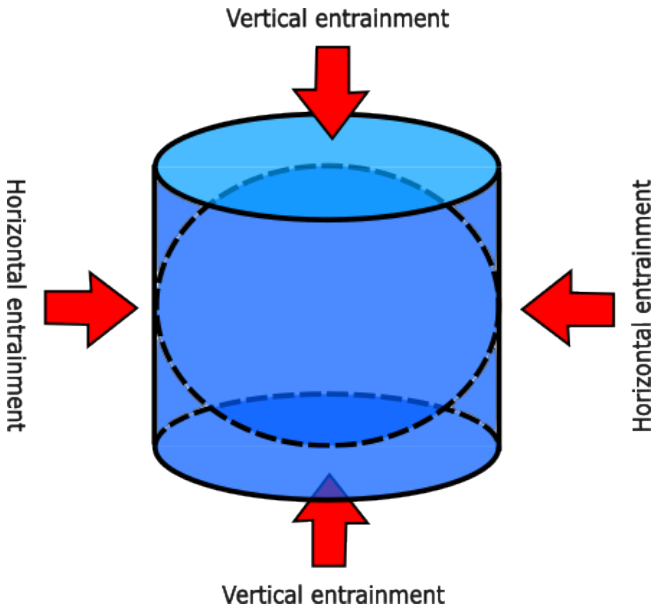

Figure 3.4: Horizontal and vertical entrainments of external water inside the patch. The vertical entrainment depends on the horizontal area given by the two basis of the cylinder, while horizontal entrainment depends on the lateral vertical surface.

The interesting thing is that these equations have a nice geometric interpretation, since the perimeter of the projected area is proportional to $\sqrt{W^2(t) + L^2(t)}$ (approximated formula for the perimeter of an ellipse) and so horizontal and vertical components in (3.19) can be reexpressed in terms of the circumscribed cylinder area (Fig. 3.4)

$$\begin{aligned} \left(\frac{dV(t)}{dt}\right)^h &\propto \frac{(\text{horizontal perimeter})^2(\text{thickness})^2}{\text{volume}} = \frac{(\text{vertical boundary area})^2}{\text{volume}} \\ \left(\frac{dV(t)}{dt}\right)^v &\propto \frac{(\text{horizontal boundary area})^2}{\text{volume}} \end{aligned} \tag{3.20}$$

The rate of change of the patch volume $V(t)$ is also related to the rate at which water from outside the patch enters by diffusion. This quantity was already introduced in Chapter 2 and was called entrainment rate Ω. Physically speaking, one can think of it as a measure of the rate of exchange of matter among the patch surface. Dimensionally, the time-dependent entrainment rate can be defined as

$$\Omega(t) = \frac{1}{V(t)}\frac{dV(t)}{dt} \tag{3.21}$$

The latter can again be decomposed in horizontal and vertical contributions, modelling the different amount of exchange present in the two directions:

$$\Omega^h(t) = \frac{1}{V(t)}\left(\frac{dV(t)}{dt}\right)^h \quad ; \quad \Omega^v(t) = \frac{1}{V(t)}\left(\frac{dV(t)}{dt}\right)^v \tag{3.22}$$

The importance of these quantities will be more clear when patch interaction with the surrounding will be investigated.

3.7 Two-dimensional approximation

In many realistic cases, a two-dimensional representation of the water patch is enough to capture the main properties of the system. If we are not interested in modelling the third dimension, the above discussion can be simplified just assuming a constant thickness of the patch $T(t) = T$ and no divergence and vertical diffusion occurring ($\delta(t) = 0$, $\kappa^v(t) = 0$). In that case, the entrainment rate can be simplified as

$$\Omega(t) = \frac{1}{A(t)} \frac{dA(t)}{dt} \tag{3.23}$$

where $A(t)$ is just the previous projected area, that coincides with the area of the ellipse representing the patch [28]. All the others equation still hold.

Chapter 4

Tracers dynamic in a changing water patch

In the previous Chapter, we analyzed how the spatial dimensions of a given water patch distribution (in the second stage of dispersal) evolve depending on the fluid dynamical parameters and diffusivity. What we didn't model yet, is how the concentrations of the tracers that are linked to the patch evolve during this stirring and expansion. This can be formulated mathematically by a full general master equation, accounting for the entrainment of external water containing different concentrations of the tracers, for the homogenization processes driven by turbulence and for the biogeochemical reactions occurring among the tracers. All these terms are examined with the powerful tool of the Reynolds decomposition, in which we renounce to characterize the entire tracers distribution and focus on the statistical properties such as distribution moments, up to the second order. We finally end up with a statistical model that resembles the main agents of the master equation, but in a simplified manner.

4.1 Reynolds decomposition

Inside a moving water patch, there may be very different species of inorganic and organic elements, each one representing a given tracer with distribution $u_i(\mathbf{x}, t)$, $i = 1, ..., n$. These concentrations are well-defined only inside the ellipsoid of reference, while in external regions different distributions of tracers containing a distinct amount of material can be considered.

Let's define properly some statistical quantities of interest related to the internal tracer distributions. We make use of the so-called "Reynolds decomposition", which express a given scalar field in terms of its average value and the fluctuations around it. In our case, the tracer distribution $u_i(\mathbf{x}, t)$ can be split into

$$u_i(\mathbf{x}, t) = \langle u_i \rangle_{pat}(t) + u_i'(\mathbf{x}, t) \tag{4.1}$$

where the mean value is defined as

$$\langle u_i \rangle_{pat}(t) = \frac{1}{V(t)} \int_{pat} u_i(\mathbf{x}, t) dV \tag{4.2}$$

and *pat* stands for the ellipsoidal patch.

The fluctuation term $u_i'(\mathbf{x}, t)$ can be used to determine the variance of the tracer distribution that is

$$\langle u_i'^2 \rangle_{pat}(t) = \frac{1}{V(t)} \int_{pat} u_i'^2(\mathbf{x}, t) dV \tag{4.3}$$

To make the things more clear, just recall the variance definition in terms of first and second moments

$$\langle u_i'^2 \rangle_{pat}(t) = \langle u_i^2 \rangle_{pat}(t) - \langle u_i \rangle_{pat}^2(t) \tag{4.4}$$

Proceeding with the same notation, the covariance between two different tracers i and j is written as

$$\langle u_i' u_j' \rangle_{pat}(t) = \frac{1}{V(t)} \int_{pat} u_i'(\mathbf{x}, t) u_j'(\mathbf{x}, t) dV \tag{4.5}$$

These statistical quantities, which have little meaning by now, will be very useful to characterize full tracers distributions properties of interest, without necessarily know the set of $u_i(\mathbf{x}, t)$ complete expressions.

4.2 Surrounding distributions

Around the water patch, we can identify three different regions: water that is present around, above and below. The cylinder circumscribed to the ellipsoid, connected also to equations (3.20), define clearly these regions, and is shown in Fig. 4.1.

In general, these surroundings can display very different characteristics due, for example, to light availability or others biogeochemical properties. Tracer concentrations are indeed described separately as $h_i(\mathbf{x}, t)$, $a_i(\mathbf{x}, t)$ and $b_i(\mathbf{x}, t)$, where h stands for *horizontal* surrounding, a for *above* and b for *below*.

To simplify the discussion, only statistical information such as means, variances and covariances of these distributions can be required. Their definition is straightforward, since they involve the same integrals of equations (4.2), (4.3), (4.5), but in different regions of space

$$\begin{aligned}
\langle h_i \rangle_{suh}(t) &= \frac{1}{V(t)} \int_{suh} h_i(\mathbf{x}, t) dV \\
\langle a_i \rangle_{sua}(t) &= \frac{1}{V(t)} \int_{sua} a_i(\mathbf{x}, t) dV \\
\langle b_i \rangle_{sub}(t) &= \frac{1}{V(t)} \int_{sub} b_i(\mathbf{x}, t) dV
\end{aligned} \tag{4.6}$$

$$\begin{aligned}
\langle h_i'^2 \rangle_{suh}(t) &= \frac{1}{V(t)} \int_{suh} h_i'^2(\mathbf{x}, t) dV \\
\langle a_i'^2 \rangle_{sua}(t) &= \frac{1}{V(t)} \int_{sua} a_i'^2(\mathbf{x}, t) dV \\
\langle b_i'^2 \rangle_{sub}(t) &= \frac{1}{V(t)} \int_{sub} b_i'^2(\mathbf{x}, t) dV
\end{aligned} \tag{4.7}$$

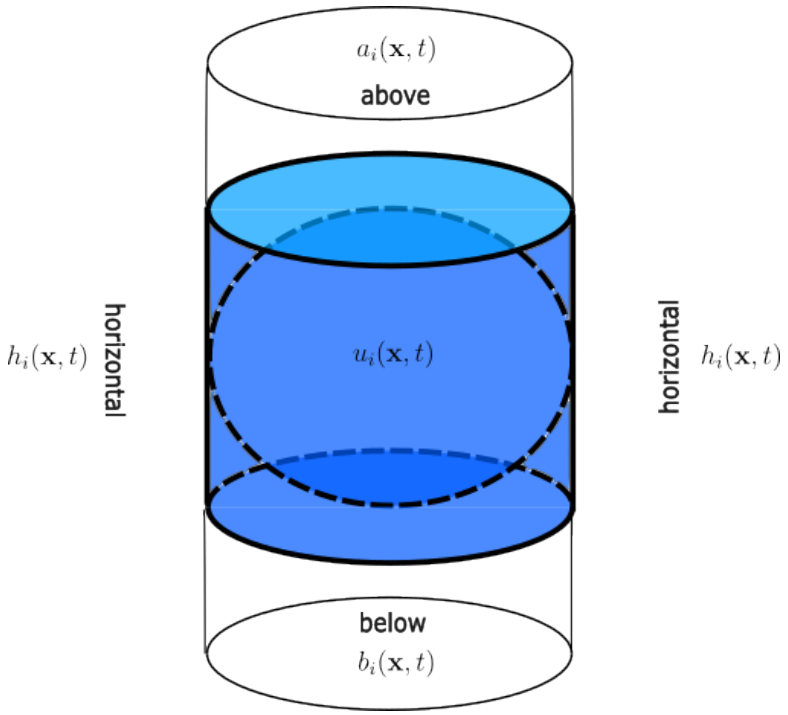

Figure 4.1: Decomposition of the water patch surrounding in three main regions: they are above, below and horizontally placed. The tracer concentrations in these areas are called, respectively, $a_i(\mathbf{x},t)$, $b_i(\mathbf{x},t)$ and $h_i(\mathbf{x},t)$.

$$\begin{aligned}
\langle h_i' h_j' \rangle_{suh}(t) &= \frac{1}{V(t)} \int_{suh} h_i'(\mathbf{x},t) h_j'(\mathbf{x},t) dV \\
\langle a_i' a_j' \rangle_{sua}(t) &= \frac{1}{V(t)} \int_{sua} a_i'(\mathbf{x},t) a_j'(\mathbf{x},t) dV \\
\langle b_i' b_j' \rangle_{sub}(t) &= \frac{1}{V(t)} \int_{sub} b_i'(\mathbf{x},t) b_j'(\mathbf{x},t) dV
\end{aligned} \tag{4.8}$$

4.3 Master equation for tracers

Starting from a general perspective, one can isolate and categorize the main processes acting on the tracers distributions as follows:

- entrainment of external water with different tracer concentration. For a given tracer i, it can be modelled by the term $\mathcal{E}[u_i; h_i, a_i, b_i]$.
- internal mixing which tend to homogenize the single tracer concentration u_i. It can be represented by the mixing term $\mathcal{M}[u_i]$
- biogeochemical interaction between different tracers due to predation and other reactions. Interaction of tracer i with all the others is summarized in $\mathcal{I}[u_i, \{u\}]$, where $\{u\}$ is the set of all tracers taken into account.

Mathematically, they can be thought as different terms acting on the time derivative of the patch distribution

$$\frac{du_i(\mathbf{x},t)}{dt} = \mathcal{E}[u_i(\mathbf{x},t); h_i(\mathbf{x},t), a_i(\mathbf{x},t), b_i(\mathbf{x},t)] + \mathcal{M}[u_i(\mathbf{x},t)] + \mathcal{I}[u_i(\mathbf{x},t), \{u(\mathbf{x},t)\}]$$
$$= \left[\frac{du_i(\mathbf{x},t)}{dt}\right]_{sur} + \left[\frac{du_i(\mathbf{x},t)}{dt}\right]_{mix} + \left[\frac{du_i(\mathbf{x},t)}{dt}\right]_{bio} \tag{4.9}$$

The complexity of this general kind of description resides on the identification of each contribution, especially for surrounding (*sur*) and mixing (*mix*) terms. They in fact cannot be seen as mere products of patch diffusion, given the presence of turbulence and intricacy of the mesoscale water flow.

We will therefore exploit the statistical quantities already defined, in order to get at least insight of how means, variances and covariances of the tracer distributions evolve in time and interact with each other.

4.4 Entrainment term

The exchange of material at the patch boundaries is given by the intrusion of external tracers that mix with the ones already present. This phenomenon can be described in several ways, for example with the definition of biogeochemical fluxes related to the entrainment rate or directly with some PDEs accounting for the diffusion of both internal and external tracer. The second approach, however, oversimplifies the interplay between the two boundaries, which can display a complex behavior not only driven by diffusion. We then aim to formalize the first of them, that is more suitable for the statistical approach we are going to take.

Consider the change of patch volume at a given time t that brings $V(t)$ to $V(t+\Delta t)$. The new added capacity is $\Delta V(t) = V(t+\Delta t) - V(t)$ and it's related to the volume derivative

$$\Delta V(t) = \lim_{\Delta t \to 0} \frac{dV(t)}{dt} \Delta t \tag{4.10}$$

Following the subdivision (3.19), one can split $\Delta V(t)$ into

$$\Delta V^h(t) = \lim_{\Delta t \to 0} \left(\frac{dV(t)}{dt}\right)^h \Delta t \quad ; \quad \Delta V^v(t) = \lim_{\Delta t \to 0} \left(\frac{dV(t)}{dt}\right)^v \Delta t \tag{4.11}$$

The added water has different characteristics, so the patch composition is modified in its properties. Let's find than how means, variances and covariances of the tracers distributions change in relation to this exchange.

The mean tracer concentration of tracer i into the added volume can be found as the weighted average of the mean concentrations in the three different surroundings.

$$\langle u_i \rangle_{\Delta V(t)}(t) = \frac{\Delta V^h(t) \langle h_i \rangle_{suh}(t) + \frac{1}{2}\Delta V^v(t) \left(\langle a_i \rangle_{sua}(t) + \langle b_i \rangle_{sub}(t)\right)}{\Delta V^h(t) + \Delta V^v(t)} \tag{4.12}$$

At the same time, also the new total mean concentration $\langle u_i \rangle_{V(t+\Delta t)}(t+\Delta t)$ can be retrieved by a weighted average between the old one and the one into the gained volume

$$\langle u_i \rangle_{V(t+\Delta t)}(t+\Delta t) = \frac{V(t)\langle u_i \rangle_{pat}(t) + \Delta V^h(t)\langle h_i \rangle_{suh}(t) + \frac{1}{2}\Delta V^v(t)(\langle a_i \rangle_{sua}(t) + \langle b_i \rangle_{sub}(t))}{V(t) + \Delta V^h(t) + \Delta V^v(t)} \tag{4.13}$$

Using the definition of derivative, the temporal evolution of the means can be written as

$$\left[\frac{d\langle u_i\rangle_{pat}(t)}{dt}\right]_{sur} = \lim_{\Delta t\to 0}\frac{\langle u_i\rangle_{V(t+\Delta t)}(t+\Delta t) - \langle u_i\rangle_{V(t)}(t)}{\Delta t} \tag{4.14}$$

which becomes in the limit

$$\left[\frac{d\langle u_i\rangle_{pat}}{dt}\right]_{sur} = \Omega^h(t)\langle h_i\rangle_{suh} + \frac{1}{2}\Omega^v(t)\left(\langle a_i\rangle_{sua} + \langle b_i\rangle_{sub}\right) - \Omega(t)\langle u_i\rangle_{pat} \tag{4.15}$$

where we omitted the temporal dependence of the means to simplify the notation. Notice that the differential equation we found depends on the geometry of the patch only through the entrainment rate $\Omega(t)$ and its components. At stationary, the mean concentration of the tracer inside the patch is meant to converge to a combination between the surrounding reservoirs mean concentrations.

Regarding the other statistical quantities, a similar approach permits to compute total concentration variances and covariances depending on the weighted averages of second moments of u_i, h_i, a_i and b_i. The equations are

$$\begin{aligned}\langle u_i'^2\rangle_{V(t+\Delta t)}(t+\Delta t) = &\frac{V(t)\langle u_i^2\rangle_{pat}(t) + \Delta V^h(t)\langle h_i^2\rangle_{suh}(t) + \frac{1}{2}\Delta V^v(t)(\langle a_i^2\rangle_{sua}(t) + \langle b_i^2\rangle_{sub}(t))}{V(t) + \Delta V^h(t) + \Delta V^v(t)}\\ &- \langle u_i\rangle^2_{V(t+\Delta t)}(t+\Delta t)\end{aligned} \tag{4.16}$$

which allows retrieving the time evolution of the variances

$$\begin{aligned}\left[\frac{d\langle u_i'^2\rangle_{pat}}{dt}\right]_{sur} &= \Omega^h(t)\left(\langle h_i'^2\rangle_{suh} - \langle u_i'^2\rangle_{pat} + (\langle h_i\rangle_{suh} - \langle u_i\rangle_{pat})^2\right) +\\ &+ \frac{1}{2}\Omega^v(t)\left(\langle a_i'^2\rangle_{sua} - \langle u_i'^2\rangle_{pat} + (\langle a_i\rangle_{sua} - \langle u_i\rangle_{pat})^2\right) +\\ &+ \frac{1}{2}\Omega^v(t)\left(\langle b_i'^2\rangle_{sub} - \langle u_i'^2\rangle_{pat} + (\langle b_i\rangle_{sub} - \langle u_i\rangle_{pat})^2\right) =\\ &= \left[\left(\frac{d\langle u_i'^2\rangle_{pat}}{dt}\right)^h\right]_{sur} + \left[\left(\frac{d\langle u_i'^2\rangle_{pat}}{dt}\right)^v\right]_{sur}\end{aligned} \tag{4.17}$$

and

$$\begin{aligned}\langle u_i'u_j'\rangle_{V(t+\Delta t)}(t+\Delta t) = &\frac{V(t)\langle u_iu_j\rangle_{pat}(t) + \Delta V^h(t)\langle h_ih_j\rangle_{suh}(t) + \frac{1}{2}\Delta V^v(t)(\langle a_ia_j\rangle_{sua}(t) + \langle b_ib_j\rangle_{sub}(t))}{V(t) + \Delta V^h(t) + \Delta V^v(t)}\\ &- \langle u_i\rangle_{V(t+\Delta t)}(t+\Delta t)\cdot\langle u_j\rangle_{V(t+\Delta t)}(t+\Delta t)\end{aligned} \tag{4.18}$$

which allows retrieving the time evolution of the covariances

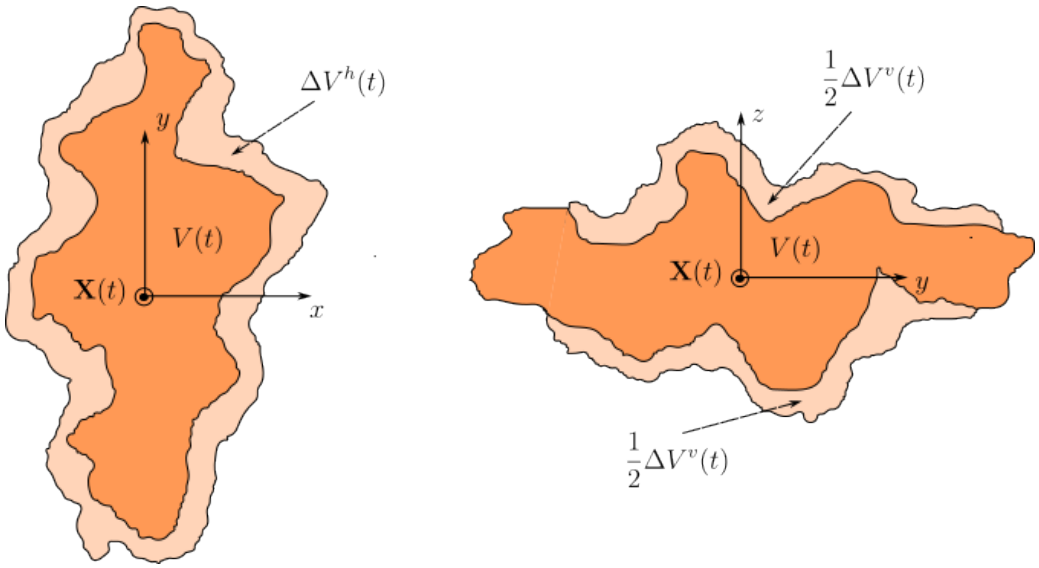

Figure 4.2: The entrainment of surrounding water into a Lagrangian patch leads to an increase of volume from $V(t)$ to $V(t) + \Delta V^h(t) + \Delta V^v(t)$ and this modifies internal tracer distributions. In the left picture, we are representing the projection of the water patch on the x-y plane, imaging to looking towards it from above. Horizontal expansion of the initial core (dark orange) embeds the horizontal water of volume $\Delta V^h(t)$ (light orange). In the right picture, the patch is projected on the y-z plane as seen from the front. Vertical expansion embeds some water from above and below, with total volume $\Delta V^v(t)$.

$$\begin{aligned}\left[\frac{d\langle u_i' u_j'\rangle_{pat}}{dt}\right]_{sur} &= \Omega^h(t)\left(\langle h_i' h_j'\rangle_{suh} - \langle u_i' u_j'\rangle_{pat} + (\langle h_i\rangle_{suh} - \langle u_i\rangle_{pat})\cdot(\langle h_j\rangle_{suh} - \langle u_j\rangle_{pat})\right) + \\ &+ \frac{1}{2}\Omega^v(t)\left(\langle a_i' a_j'\rangle_{sua} - \langle u_i' u_j'\rangle_{pat} + (\langle a_i\rangle_{sua} - \langle u_i\rangle_{pat})\cdot(\langle a_j\rangle_{sua} - \langle u_j\rangle_{pat})\right) + \\ &+ \frac{1}{2}\Omega^v(t)\left(\langle b_i' b_j'\rangle_{sub} - \langle u_i' u_j'\rangle_{pat} + (\langle b_i\rangle_{sub} - \langle u_i\rangle_{pat})\cdot(\langle b_j\rangle_{sub} - \langle u_j\rangle_{pat})\right) = \\ &= \left[\left(\frac{d\langle u_i' u_j'\rangle_{pat}}{dt}\right)^h\right]_{sur} + \left[\left(\frac{d\langle u_i' u_j'\rangle_{pat}}{dt}\right)^v\right]_{sur}\end{aligned} \tag{4.19}$$

Despite the large amount of terms and variables involved, the idea behind is very simple. In the case of equilibrium between the inside and outside means, variances and covariances of the inside tracers distribution will tend to the one outside, implying patch total dilution. If instead the mean difference is different from zero, we expect that heterogeneity inside is enhanced with respect to the one outside.

4.5 Mixing term

In a three-dimensional incompressible turbulent flow, passive tracers undergo mixing processes that gradually equalize their concentration over time. Various methods have been elaborated to theoretically describe the decline of tracer concentration moments [2], [31]. In particular, the rate at which tracer second moments decrease can be linked to the diffusion rate $\kappa(t)$ and the system size $S(t)$ considered. Due to the different horizontal and vertical dynamic of the water patch, mixing acts separately on the two components

$$\begin{aligned}\left[\left(\frac{d\langle u_i' u_j'\rangle_{pat}}{dt}\right)^h\right]_{mix} &= -\frac{\kappa^h(t)}{(S^h(t))^2}\langle u_i' u_j'\rangle_{pat} \\ \left[\left(\frac{d\langle u_i' u_j'\rangle_{pat}}{dt}\right)^v\right]_{mix} &= -\frac{\kappa^v(t)}{(S^v(t))^2}\langle u_i' u_j'\rangle_{pat}\end{aligned} \tag{4.20}$$

We remember that system's characteristic sizes $S^h(t)$ and $S^v(t)$ are expressible as

$$\begin{aligned}S^h(t) &= W(t) + L(t) \\ S^v(t) &= 2T(t)\end{aligned} \tag{4.21}$$

4.6 Interaction term

Tracer's interaction can be modelled, from the mathematical point of view, as an interaction between scalar fields in the space. By assuming the presence of n different tracers in our description, we would have a system of n ODEs defining in detail tracers' relation. Using the vector $\mathbf{U}$ to denote the set of the n scalar fields u_i, each equation of the system can be written in the form

$$\frac{du_i(\mathbf{x},t)}{dt} = F_i^{bio}(\mathbf{U}(\mathbf{x},t)) \qquad \mathbf{U}(\mathbf{x},t) = \{u_1(\mathbf{x},t), ..., u_n(\mathbf{x},t)\} \tag{4.22}$$

Since, as before, we don't want to resolve explicitly the spatial heterogeneity of these distributions, the idea is to understand again how the main statistical quantities are affected by the interactions. For this purpose, the function F_i^{bio} can be expanded [33] around tracers' vector mean value $\langle\mathbf{U}\rangle_{pat} = \{\langle u_1\rangle_{pat}, ..., \langle u_n\rangle_{pat}\}$ and written in terms of the fluctuations as

$$\begin{aligned}\frac{du_i(\mathbf{x},t)}{dt} &= F_i^{bio}(\mathbf{U}(\mathbf{x},t)) \\ &\simeq F_i^{bio}(\langle\mathbf{U}\rangle_{pat}) + \sum_{l=1}^{n}\frac{\partial F_i^{bio}}{\partial u_l}(\langle\mathbf{U}\rangle_{pat})\cdot u_l'(\mathbf{x},t) + \\ &+ \frac{1}{2}\sum_{l,k=1}^{n}\frac{\partial^2 F_i^{bio}}{\partial u_l \partial u_k}(\langle\mathbf{U}\rangle_{pat})\cdot u_l'(\mathbf{x},t)u_k'(\mathbf{x},t) + ...\end{aligned} \tag{4.23}$$

Averaging over space as usual, we get

$$\left[\frac{d\langle u_i\rangle_{pat}}{dt}\right]_{bio} \simeq F_i^{bio}(\langle\mathbf{U}\rangle_{pat}) + \frac{1}{2}\sum_{l,k=1}^{n}\frac{\partial^2 F_i^{bio}}{\partial u_l \partial u_k}(\langle\mathbf{U}\rangle_{pat})\cdot\langle u_l' u_k'\rangle_{pat} \tag{4.24}$$

Truncating the expansion at the second order of the fluctuation is a so-called "closure assumption". We are indeed imposing to third and higher moments of being negligible, reducing the total number of variables needed to fully describe $u_i(\mathbf{x},t)$. Subtracting equation (4.24) to (4.23) we find the fluctuation time derivative

$$\begin{aligned}\frac{du_i'(\mathbf{x},t)}{dt} \simeq &\sum_{l=1}^{n} \frac{\partial F_i^{bio}}{\partial u_l}(\langle \mathbf{U}\rangle_{pat}) \cdot u_l'(\mathbf{x},t) + \\ &+ \frac{1}{2}\sum_{l,k=1}^{n} \frac{\partial^2 F_i^{bio}}{\partial u_l \partial u_k}(\langle \mathbf{U}\rangle_{pat}) \cdot \left(u_l'(\mathbf{x},t)u_k'(\mathbf{x},t) - \langle u_l' u_k'\rangle_{pat}\right)\end{aligned} \tag{4.25}$$

If now we multiply by $u_j'(\mathbf{x},t)$ both members, swap the indices i and j and sum to the old expression, finally averaging in space we obtain

$$\left[\frac{d\langle u_i' u_j'\rangle_{pat}}{dt}\right]_{bio} \simeq \sum_{k=1}^{n}\left[\frac{\partial F_i^{bio}}{\partial u_k}(\langle \mathbf{U}\rangle_{pat}) \cdot \langle u_j' u_k'\rangle_{pat} + \frac{\partial F_j^{bio}}{\partial u_k}(\langle \mathbf{U}\rangle_{pat}) \cdot \langle u_i' u_k'\rangle_{pat}\right] \tag{4.26}$$

that is the time derivative of tracers covariances. The variances' behavior is trivially obtained for $i = j$.

4.7 Statistical model summary

The master equation (4.9) denotes how a tracer distribution inside a water patch evolves due to entrainment, mixing and interaction with the others. Through a statistical approach, this dynamic can be approximated by evolution of the mean, variance and covariance. We have seen that changes in the mean are due to entrainment of external water and interactions, while changes in the second moments account also to internal mixing. All this can be summarized by

$$\begin{aligned}\frac{d\langle u_i\rangle_{pat}}{dt} &= \left[\frac{d\langle u_i\rangle_{pat}}{dt}\right]_{sur} + \left[\frac{d\langle u_i\rangle_{pat}}{dt}\right]_{bio} \\ \frac{d\langle u_i'^2\rangle_{pat}}{dt} &= \left[\frac{d\langle u_i'^2\rangle_{pat}}{dt}\right]_{sur} + \left[\frac{d\langle u_i'^2\rangle_{pat}}{dt}\right]_{mix} + \left[\frac{d\langle u_i'^2\rangle_{pat}}{dt}\right]_{bio} \\ \frac{d\langle u_i' u_j'\rangle_{pat}}{dt} &= \left[\frac{d\langle u_i' u_j'\rangle_{pat}}{dt}\right]_{sur} + \left[\frac{d\langle u_i' u_j'\rangle_{pat}}{dt}\right]_{mix} + \left[\frac{d\langle u_i' u_j'\rangle_{pat}}{dt}\right]_{bio}\end{aligned} \tag{4.27}$$

Once specified the extent of the interactions between the tracers, this model requires knowing a priori first and second moments of the surrounding tracer distributions, as well as the entrainment rate that depends on $W(t)$, $L(t)$ and $T(t)$.

Chapter 5

Phytoplankton and carbon in the statistical model

In this Chapter we focus on a specific scenario where the tracers under consideration are phytoplankton, nutrients, and dissolved inorganic carbon, even if the previously presented model can be adapted to accommodate any number of tracers. We identify the biogeochemical interactions, undergoing in the ocean, that connect abundances of these organisms and compounds. In particular, an equation for the pCO_2 anomaly is developed starting from the carbon dynamics already discussed in the introduction. A closed system of equations is so reached and expanded to determine the statistical contributions entering in the full model. We finally end up with a complex set of nine equations describing first and second moments of the phytoplankton, nutrient and partial pressure anomaly distributions.

5.1 Biogeochemical statistical model

We start from the model discussed in Section 2 and apply that consumer-resource dynamic between two tracers, which represent phytoplankton $P(\mathbf{x},t)$ and a generic limiting nutrient $N(\mathbf{x},t)$. We also describe how the amount of dissolved inorganic carbon in the patch water $DIC(\mathbf{x},t)$ changes in response to this consumption and to air-sea flux of CO_2. The latter takes the form of

$$\begin{aligned}\left[\frac{dDIC(\mathbf{x},t)}{dt}\right]_{bio} = \left[\frac{dDIC(\mathbf{x},t)}{dt}\right]_{flux} + \left[\frac{dDIC(\mathbf{x},t)}{dt}\right]_{upt} = \\ = -\frac{F_{CO_2}(\mathbf{x},t)}{\rho h} \qquad + \frac{1}{\rho} S_{upt}(\mathbf{x},t) R_{C_T:N}\end{aligned} \tag{5.1}$$

where $R_{C_T:N}$ is the conversion factor between moles of nutrient consumed in S_{upt} (upt stands for "uptake") to moles of carbon, and h is the mixed layer depth in a given region of the ocean. The equations relating all the tracers are then

$$\begin{aligned}\left[\frac{dN(\mathbf{x},t)}{dt}\right]_{bio} &= -\nu \frac{N(\mathbf{x},t)}{N(\mathbf{x},t)+k} P(\mathbf{x},t) \equiv S_{upt}(\mathbf{x},t) \\ \left[\frac{dP(\mathbf{x},t)}{dt}\right]_{bio} &= +\nu \frac{N(\mathbf{x},t)}{N(\mathbf{x},t)+k} P(\mathbf{x},t) - mP(\mathbf{x},t) \\ \left[\frac{dDIC(\mathbf{x},t)}{dt}\right]_{bio} &= -\frac{K_o K_g \Delta p(\mathbf{x},t)}{h} + \frac{1}{\rho} S_{upt}(\mathbf{x},t) R_{C_T:N}\end{aligned} \tag{5.2}$$

Remember that ν is the phytoplankton maximum growth rate, k is the half-saturation constant and m is the phytoplankton mortality. The other parameters were introduced in Section 1.3 and are CO_2 solubility, K_o, CO_2 transfer velocity in water, K_g, and anomaly in partial pressure of CO_2, Δp.

Notice that the first two equations do not depend on carbon utilization, since this element is generally not considered a limiting factor for phytoplankton growth.

This system has also three equations but four variables (or better, fields) that are involved. The relationship between DIC and Δp needs, then, to be investigated.

5.2 pCO_2 anomaly as a tracer

The last equation of (5.2) can be reformulated to achieve a closed system of ODEs, as the one expected by (4.22) notation.

Foremost, let's use the DIC decomposition in saturation and disequilibrium components, respectively C_{sat} and ΔC

$$DIC(\mathbf{x},t) = C_{sat}(\mathbf{x},t) + \Delta C(\mathbf{x},t) \tag{5.3}$$

This allows to rewrite the equation (5.1) as

$$\frac{d\Delta C(\mathbf{x},t)}{dt} = -\frac{K_o K_g}{h}\Delta p(\mathbf{x},t) + \frac{1}{\rho}S_{upt}(\mathbf{x},t)R_{C_T:N} - \frac{dC_{sat}(\mathbf{x},t)}{dt} \tag{5.4}$$

Using the Revelle buffer factor B, introduced in Section 1.3, the residual component of the DIC can be reexpressed in terms of saturation component and the pCO_2 difference between the water and the atmosphere.

$$\Delta C(\mathbf{x},t) = \frac{C_{sat}(\mathbf{x},t)}{B \cdot pCO_2^{atm}(\mathbf{x},t)}\Delta p(\mathbf{x},t) \tag{5.5}$$

Deriving in time, making the assumption that $pCO_2^{atm}(\mathbf{x},t)$ is pretty constant, we obtain

$$\begin{aligned}
\frac{d\Delta C(\mathbf{x},t)}{dt} &= \frac{1}{B \cdot pCO_2^{atm}}\frac{d(C_{sat}(\mathbf{x},t)\cdot\Delta p(\mathbf{x},t))}{dt} \\
&= \frac{C_{sat}(\mathbf{x},t)}{B \cdot pCO_2^{atm}}\left[\frac{1}{C_{sat}(\mathbf{x},t)}\frac{dC_{sat}(\mathbf{x},t)}{dt}\cdot\Delta p(\mathbf{x},t) + \frac{d\Delta p(\mathbf{x},t)}{dt}\right] \\
&= \phi^{-1}(\mathbf{x},t)\left[\frac{1}{C_{sat}(\mathbf{x},t)}\frac{dC_{sat}(\mathbf{x},t)}{dt}\cdot\Delta p(\mathbf{x},t) + \frac{d\Delta p(\mathbf{x},t)}{dt}\right]
\end{aligned} \tag{5.6}$$

where some terms are grouped into $\phi(\mathbf{x},t)$, that is defined as

$$\phi(\mathbf{x},t) = \left(\frac{C_{sat}(\mathbf{x},t)}{B \cdot pCO_2^{atm}}\right)^{-1} \tag{5.7}$$

Inserting (5.6) into (5.4) and isolating the time derivative of $\Delta p(\mathbf{x},t)$ leads to

$$\frac{d\Delta p(\mathbf{x},t)}{dt} = -\phi(\mathbf{x},t)\frac{K_o K_g}{h}\Delta p(\mathbf{x},t) + \frac{\phi(\mathbf{x},t)}{\rho}S_{upt}(\mathbf{x},t)R_{C_T:Fe} - \phi(\mathbf{x},t)\frac{dC_{sat}(\mathbf{x},t)}{dt} + \\ - \frac{1}{C_{sat}(\mathbf{x},t)}\frac{dC_{sat}(\mathbf{x},t)}{dt}\cdot\Delta p(\mathbf{x},t) \tag{5.8}$$

Equation (5.8) denotes how the time evolution of the partial pressure anomaly depends on the other tracers N and P and also on the C_{sat} distribution. The impact of the latter has to be properly analyzed. Since we expect that $\Delta p << B\cdot pCO_2^{atm}$, the last term involving $\Delta p(\mathbf{x},t)/C_{sat}(\mathbf{x},t)$ can be considered negligible. The remaining term with $C_{sat}(\mathbf{x},t)$ derivative depends only on environmental factors like temperature, alkalinity and salinity. Assuming that the temperature $\mathcal{T}$ dependence is the stronger than the others, one can expand

$$\frac{dC_{sat}(\mathbf{x},t)}{dt} \simeq \frac{dC_{sat}(\mathbf{x},t)}{d\mathcal{T}(\mathbf{x},t)}\frac{d\mathcal{T}(\mathbf{x},t)}{dt} = \gamma_{\mathcal{T}}\frac{d\mathcal{T}(\mathbf{x},t)}{dt} \tag{5.9}$$

where $\gamma_{\mathcal{T}}$ is the locally linear proportionality constant between C_{sat} and $\mathcal{T}$ [35]. A last approximation is also to consider ϕ to be constant, since its derivatives in space and time are smaller of order of magnitudes with respect to the other quantities.

At the end, we get this simplified equation for Δp variation

$$\frac{d\Delta p(\mathbf{x},t)}{dt} = -\phi\frac{K_o K_g}{h}\Delta p(\mathbf{x},t) + \frac{\phi}{\rho}S_{upt}(\mathbf{x},t)R_{C_T:N} - \phi\gamma_{\mathcal{T}}\frac{d\mathcal{T}(\mathbf{x},t)}{dt} \tag{5.10}$$

which only requires knowing the temperature field dynamic, eventually retrieved from data. Relaxing further the need to characterize temperature heterogeneity and peculiarity inside the patch, we can simply model an average temperature present everywhere and equal to $\bar{\mathcal{T}}$.

This result indicates that, with these approximations, we can think of Δp as the only needed field (or, in all respects, tracer) accounting for the carbon dynamic inside the patch.

5.3 Full model description

The consumer-resource model with carbon uptake (5.2) can be written on its final shape as

$$\begin{aligned}
\left[\frac{dN(\mathbf{x},t)}{dt}\right]_{bio} &= -\nu\frac{N(\mathbf{x},t)}{N(\mathbf{x},t)+k}P(\mathbf{x},t) \equiv S_{bio}(\mathbf{x},t) \\
\left[\frac{dP(\mathbf{x},t)}{dt}\right]_{bio} &= +\nu\frac{N(\mathbf{x},t)}{N(\mathbf{x},t)+k}P(\mathbf{x},t) - mP(\mathbf{x},t) \\
\left[\frac{d\Delta p(\mathbf{x},t)}{dt}\right]_{bio} &= \left[\frac{d\Delta p(\mathbf{x},t)}{dt}\right]_{flux} + \left[\frac{d\Delta p(\mathbf{x},t)}{dt}\right]_{upt} + \left[\frac{d\Delta p(\mathbf{x},t)}{dt}\right]_{temp} = \\
&= -\phi\frac{K_o K_g}{h}\Delta p(\mathbf{x},t) + \frac{\phi}{\rho}S_{upt}(\mathbf{x},t)R_{C_T:N} - \phi\gamma_{\mathcal{T}}\frac{d\bar{\mathcal{T}}}{dt}
\end{aligned} \tag{5.11}$$

Unfortunately, this is only the description of the interactions between the involved tracers, so we have yet to formalize what are the effects of the drifting of such ecosystem in space. Taking up the statistical approach that we defined earlier, we only need to identify the terms appearing in (4.27) with $\{u_1, u_2, u_3\}$ being $\{N, P, \Delta p\}$.

5.3.1 Entrainment

The specification of the entrainment effect on tracers' moments is trivial once defined surrounding distribution moments as

$$\begin{matrix} \langle N_h \rangle_{suh} & \langle P_h \rangle_{suh} & \langle \Delta p_h \rangle_{suh} \\ \langle N_a \rangle_{sua} & \langle P_a \rangle_{sua} & \langle \Delta p_a \rangle_{sua} \\ \langle N_b \rangle_{sub} & \langle P_b \rangle_{sub} & \langle \Delta p_b \rangle_{sub} \end{matrix}$$

$$\begin{matrix} \langle N_h'^2 \rangle_{suh} & \langle P_h'^2 \rangle_{suh} & \langle \Delta p_h'^2 \rangle_{suh} \\ \langle N_a'^2 \rangle_{sua} & \langle P_a'^2 \rangle_{sua} & \langle \Delta p_a'^2 \rangle_{sua} \\ \langle N_b'^2 \rangle_{sub} & \langle P_b'^2 \rangle_{sub} & \langle \Delta p_b'^2 \rangle_{sub} \end{matrix}$$

$$\begin{matrix} \langle N_h' P_h' \rangle_{suh} & \langle N_h' \Delta p_h' \rangle_{suh} & \langle P_h' \Delta p_h' \rangle_{suh} \\ \langle N_a' P_a' \rangle_{sua} & \langle N_a' \Delta p_a' \rangle_{sua} & \langle P_a' \Delta p_a' \rangle_{sua} \\ \langle N_b' P_b' \rangle_{sub} & \langle N_b' \Delta p_b' \rangle_{sub} & \langle P_b' \Delta p_b' \rangle_{sub} \end{matrix}$$

which are, in total, $3 \cdot (2n + n(n-1)/2) = 27$. The amount of statistical quantities to know a priori seems a little bit scary, but in general one can think to model external tracer distributions that are homogeneous, imposing second moments of the reservoirs to be negligible.

Anyway, let's stay general and write equations (4.15), (4.17) and (4.19) for N, P, Δp and their just defined surroundings as

$$\begin{aligned} \left[\frac{d\langle N \rangle_{pat}}{dt}\right]_{sur} &= \Omega^h(t)\langle N_h \rangle_{suh} + \frac{1}{2}\Omega^v(t)\left(\langle N_a \rangle_{sua} + \langle N_b \rangle_{sub}\right) - \Omega(t)\langle N \rangle_{pat} \\ \left[\frac{d\langle P \rangle_{pat}}{dt}\right]_{sur} &= \Omega^h(t)\langle P_h \rangle_{suh} + \frac{1}{2}\Omega^v(t)\left(\langle P_a \rangle_{sua} + \langle P_b \rangle_{sub}\right) - \Omega(t)\langle P \rangle_{pat} \\ \left[\frac{d\langle \Delta p \rangle_{pat}}{dt}\right]_{sur} &= \Omega^h(t)\langle \Delta p_h \rangle_{suh} + \frac{1}{2}\Omega^v(t)\left(\langle \Delta p_a \rangle_{sua} + \langle \Delta p_b \rangle_{sub}\right) - \Omega(t)\langle \Delta p \rangle_{pat} \end{aligned} \tag{5.12}$$

$$
\begin{aligned}
\left[\frac{d\langle N'^2\rangle_{pat}}{dt}\right]_{sur} &= \Omega^h(t)\left(\langle N_h'^2\rangle_{suh} - \langle N'^2\rangle_{pat} + (\langle N_h\rangle_{suh} - \langle N\rangle_{pat})^2\right) + \\
&+ \frac{1}{2}\Omega^v(t)\left(\langle N_a'^2\rangle_{sua} - \langle N'^2\rangle_{pat} + (\langle N_a\rangle_{sua} - \langle N\rangle_{pat})^2\right) + \\
&+ \frac{1}{2}\Omega^v(t)\left(\langle N_b'^2\rangle_{sub} - \langle N'^2\rangle_{pat} + (\langle N_b\rangle_{sub} - \langle N\rangle_{pat})^2\right) = \\
&= \left[\left(\frac{d\langle N'^2\rangle_{pat}}{dt}\right)^h\right]_{sur} + \left[\left(\frac{d\langle N'^2\rangle_{pat}}{dt}\right)^v\right]_{sur}
\end{aligned}
$$

$$
\begin{aligned}
\left[\frac{d\langle P'^2\rangle_{pat}}{dt}\right]_{sur} &= \Omega^h(t)\left(\langle P_h'^2\rangle_{suh} - \langle P'^2\rangle_{pat} + (\langle P_h\rangle_{suh} - \langle P\rangle_{pat})^2\right) + \\
&+ \frac{1}{2}\Omega^v(t)\left(\langle P_a'^2\rangle_{sua} - \langle P'^2\rangle_{pat} + (\langle P_a\rangle_{sua} - \langle P\rangle_{pat})^2\right) + \\
&+ \frac{1}{2}\Omega^v(t)\left(\langle P_b'^2\rangle_{sub} - \langle P'^2\rangle_{pat} + (\langle P_b\rangle_{sub} - \langle P\rangle_{pat})^2\right) = \\
&= \left[\left(\frac{d\langle P'^2\rangle_{pat}}{dt}\right)^h\right]_{sur} + \left[\left(\frac{d\langle P'^2\rangle_{pat}}{dt}\right)^v\right]_{sur}
\end{aligned}
\tag{5.13}
$$

$$
\begin{aligned}
\left[\frac{d\langle \Delta p'^2\rangle_{pat}}{dt}\right]_{sur} &= \Omega^h(t)\left(\langle \Delta p_h'^2\rangle_{suh} - \langle \Delta p'^2\rangle_{pat} + (\langle \Delta p_h\rangle_{suh} - \langle \Delta p\rangle_{pat})^2\right) + \\
&+ \frac{1}{2}\Omega^v(t)\left(\langle \Delta p_a'^2\rangle_{sua} - \langle \Delta p'^2\rangle_{pat} + (\langle \Delta p_a\rangle_{sua} - \langle \Delta p\rangle_{pat})^2\right) + \\
&+ \frac{1}{2}\Omega^v(t)\left(\langle \Delta p_b'^2\rangle_{sub} - \langle \Delta p'^2\rangle_{pat} + (\langle \Delta p_b\rangle_{sub} - \langle \Delta p\rangle_{pat})^2\right) = \\
&= \left[\left(\frac{d\langle \Delta p'^2\rangle_{pat}}{dt}\right)^h\right]_{sur} + \left[\left(\frac{d\langle \Delta p'^2\rangle_{pat}}{dt}\right)^v\right]_{sur}
\end{aligned}
$$

$$
\begin{aligned}
\left[\frac{d\langle N'P'\rangle_{pat}}{dt}\right]_{sur} &= \Omega^h(t)\left(\langle N'_hP'_h\rangle_{suh} - \langle N'P'\rangle_{pat} + (\langle N_h\rangle_{suh} - \langle N\rangle_{pat})\cdot(\langle P_h\rangle_{suh} - \langle P\rangle_{pat})\right) + \\
&+ \frac{1}{2}\Omega^v(t)\left(\langle N'_aP'_a\rangle_{sua} - \langle N'P'\rangle_{pat} + (\langle N_a\rangle_{sua} - \langle N\rangle_{pat})\cdot(\langle P_a\rangle_{sua} - \langle P\rangle_{pat})\right) + \\
&+ \frac{1}{2}\Omega^v(t)\left(\langle N'_bP'_b\rangle_{sub} - \langle N'P'\rangle_{pat} + (\langle N_b\rangle_{sub} - \langle N\rangle_{pat})\cdot(\langle P_b\rangle_{sub} - \langle P\rangle_{pat})\right) = \\
&= \left[\left(\frac{d\langle N'P'\rangle_{pat}}{dt}\right)^h\right]_{sur} + \left[\left(\frac{d\langle N'P'\rangle_{pat}}{dt}\right)^v\right]_{sur}
\end{aligned}
$$

$$
\begin{aligned}
\left[\frac{d\langle N'\Delta p'\rangle_{pat}}{dt}\right]_{sur} &= \Omega^h(t)\left(\langle N'_h\Delta p'_h\rangle_{suh} - \langle N'\Delta p'\rangle_{pat} + (\langle N_h\rangle_{suh} - \langle N\rangle_{pat})\cdot(\langle \Delta p_h\rangle_{suh} - \langle \Delta p\rangle_{pat})\right) + \\
&+ \frac{1}{2}\Omega^v(t)\left(\langle N'_a\Delta p'_a\rangle_{sua} - \langle N'\Delta p'\rangle_{pat} + (\langle N_a\rangle_{sua} - \langle N\rangle_{pat})\cdot(\langle \Delta p_a\rangle_{sua} - \langle \Delta p\rangle_{pat})\right) + \\
&+ \frac{1}{2}\Omega^v(t)\left(\langle N'_b\Delta p'_b\rangle_{sub} - \langle N'\Delta p'\rangle_{pat} + (\langle N_b\rangle_{sub} - \langle N\rangle_{pat})\cdot(\langle \Delta p_b\rangle_{sub} - \langle \Delta p\rangle_{pat})\right) = \\
&= \left[\left(\frac{d\langle N'\Delta p'\rangle_{pat}}{dt}\right)^h\right]_{sur} + \left[\left(\frac{d\langle N'\Delta p'\rangle_{pat}}{dt}\right)^v\right]_{sur}
\end{aligned}
$$

$$
\begin{aligned}
\left[\frac{d\langle P'\Delta p'\rangle_{pat}}{dt}\right]_{sur} &= \Omega^h(t)\left(\langle P'_h\Delta p'_h\rangle_{suh} - \langle P'\Delta p'\rangle_{pat} + (\langle P_h\rangle_{suh} - \langle P\rangle_{pat})\cdot(\langle \Delta p_h\rangle_{suh} - \langle \Delta p\rangle_{pat})\right) + \\
&+ \frac{1}{2}\Omega^v(t)\left(\langle P'_a\Delta p'_a\rangle_{sua} - \langle P'\Delta p'\rangle_{pat} + (\langle P_a\rangle_{sua} - \langle P\rangle_{pat})\cdot(\langle \Delta p_a\rangle_{sua} - \langle \Delta p\rangle_{pat})\right) + \\
&+ \frac{1}{2}\Omega^v(t)\left(\langle P'_b\Delta p'_b\rangle_{sub} - \langle P'\Delta p'\rangle_{pat} + (\langle P_b\rangle_{sub} - \langle P\rangle_{pat})\cdot(\langle \Delta p_b\rangle_{sub} - \langle \Delta p\rangle_{pat})\right) = \\
&= \left[\left(\frac{d\langle P'\Delta p'\rangle_{pat}}{dt}\right)^h\right]_{sur} + \left[\left(\frac{d\langle P'\Delta p'\rangle_{pat}}{dt}\right)^v\right]_{sur}
\end{aligned}
\tag{5.14}
$$

We see that, as expected, each tracer is subject to the same dilution process with the respective reservoir.

5.3.2 Mixing

Referring to equations (4.20), for each considered tracer we have

$$
\begin{aligned}
\left[\left(\frac{d\langle N'^2\rangle_{pat}}{dt}\right)^h\right]_{mix} &= -\frac{\kappa^h(t)}{(S^h(t))^2}\langle N'^2\rangle_{pat} \\
\left[\left(\frac{d\langle N'^2\rangle_{pat}}{dt}\right)^v\right]_{mix} &= -\frac{\kappa^v(t)}{(S^v(t))^2}\langle N'^2\rangle_{pat} \\
\left[\left(\frac{d\langle P'^2\rangle_{pat}}{dt}\right)^h\right]_{mix} &= -\frac{\kappa^h(t)}{(S^h(t))^2}\langle P'^2\rangle_{pat} \\
\left[\left(\frac{d\langle P'^2\rangle_{pat}}{dt}\right)^v\right]_{mix} &= -\frac{\kappa^v(t)}{(S^v(t))^2}\langle P'^2\rangle_{pat} \\
\left[\left(\frac{d\langle \Delta p'^2\rangle_{pat}}{dt}\right)^h\right]_{mix} &= -\frac{\kappa^h(t)}{(S^h(t))^2}\langle \Delta p'^2\rangle_{pat} \\
\left[\left(\frac{d\langle \Delta p'^2\rangle_{pat}}{dt}\right)^v\right]_{mix} &= -\frac{\kappa^v(t)}{(S^v(t))^2}\langle \Delta p'^2\rangle_{pat}
\end{aligned}
\tag{5.15}
$$

$$
\begin{aligned}
\left[\left(\frac{d\langle N'P'\rangle_{pat}}{dt}\right)^h\right]_{mix} &= -\frac{\kappa^h(t)}{(S^h(t))^2}\langle N'P'\rangle_{pat} \\
\left[\left(\frac{d\langle N'P'\rangle_{pat}}{dt}\right)^v\right]_{mix} &= -\frac{\kappa^v(t)}{(S^v(t))^2}\langle N'P'\rangle_{pat} \\
\left[\left(\frac{d\langle N'\Delta p'\rangle_{pat}}{dt}\right)^h\right]_{mix} &= -\frac{\kappa^h(t)}{(S^h(t))^2}\langle N'\Delta p'\rangle_{pat} \\
\left[\left(\frac{d\langle N'\Delta p'\rangle_{pat}}{dt}\right)^v\right]_{mix} &= -\frac{\kappa^v(t)}{(S^v(t))^2}\langle N'\Delta p'\rangle_{pat} \\
\left[\left(\frac{d\langle P'\Delta p'\rangle_{pat}}{dt}\right)^h\right]_{mix} &= -\frac{\kappa^h(t)}{(S^h(t))^2}\langle P'\Delta p'\rangle_{pat} \\
\left[\left(\frac{d\langle P'\Delta p'\rangle_{pat}}{dt}\right)^v\right]_{mix} &= -\frac{\kappa^v(t)}{(S^v(t))^2}\langle P'\Delta p'\rangle_{pat}
\end{aligned}
\tag{5.16}
$$

5.3.3 Interaction

The application of the closure method defined by (4.24) and (4.26) leads to the following biogeochemical relations between tracer moments

$$
\begin{aligned}
\left[\frac{d\langle N\rangle_{pat}}{dt}\right]_{bio} &= -\nu\frac{\langle N\rangle_{pat}\langle P\rangle_{pat}}{\langle N\rangle_{pat}+k} + \nu k\frac{\langle P\rangle_{pat}\langle N'^2\rangle_{pat}}{(\langle N\rangle_{pat}+k)^3} - \nu k\frac{\langle N'P'\rangle_{pat}}{(\langle N\rangle_{pat}+k)^2} \\
\left[\frac{d\langle P\rangle_{pat}}{dt}\right]_{bio} &= +\nu\frac{\langle N\rangle_{pat}\langle P\rangle_{pat}}{\langle N\rangle_{pat}+k} - m\langle P\rangle_{pat} - \nu k\frac{\langle P\rangle_{pat}\langle N'^2\rangle_{pat}}{(\langle N\rangle_{pat}+k)^3} + \nu k\frac{\langle N'P'\rangle_{pat}}{(\langle N\rangle_{pat}+k)^2} \\
\left[\frac{d\langle \Delta p\rangle_{pat}}{dt}\right]_{bio} &= \left[\frac{d\langle \Delta p\rangle_{pat}}{dt}\right]_{flux} + \left[\frac{d\langle \Delta p\rangle_{pat}}{dt}\right]_{upt} + \left[\frac{d\langle \Delta p\rangle_{pat}}{dt}\right]_{temp} = \\
&= -\phi\frac{K_o K_g}{h}\langle \Delta p\rangle_{pat} + \frac{\phi}{\rho}\left[\frac{d\langle N\rangle_{pat}}{dt}\right]_{bio}\cdot R_{C_T:N} - \phi\gamma_{\mathcal{T}}\frac{d\bar{\mathcal{T}}}{dt}
\end{aligned}
\tag{5.17}
$$

$$
\begin{aligned}
\left[\frac{d\langle N'^2\rangle_{pat}}{dt}\right]_{bio} &= -2\nu k\frac{\langle P\rangle_{pat}\langle N'^2\rangle_{pat}}{(\langle N\rangle_{pat}+k)^2} - 2\nu\frac{\langle N\rangle_{pat}}{\langle N\rangle_{pat}+k}\langle N'P'\rangle_{pat} \\
\left[\frac{d\langle P'^2\rangle_{pat}}{dt}\right]_{bio} &= \left(+2\nu\frac{\langle N\rangle_{pat}}{\langle N\rangle_{pat}+k} - 2m\right)\langle P'^2\rangle_{pat} + 2\nu k\frac{\langle P\rangle_{pat}\langle N'P'\rangle_{pat}}{(\langle N\rangle_{pat}+k)^2} \\
\left[\frac{d\langle \Delta p'^2\rangle_{pat}}{dt}\right]_{bio} &= \left[\frac{d\langle \Delta p'^2\rangle_{pat}}{dt}\right]_{flux} + \left[\frac{d\langle \Delta p'^2\rangle_{pat}}{dt}\right]_{upt} = \\
&= -2\phi\frac{K_o K_g}{h}\langle \Delta p'^2\rangle_{pat} + \\
&\quad + \frac{\phi}{\rho}\left[-2\nu k\frac{\langle P\rangle_{pat}}{(\langle N\rangle_{pat}+k)^2}\langle N'\Delta p'\rangle_{pat} - 2\nu\frac{\langle N\rangle_{pat}}{\langle N\rangle_{pat}+k}\langle P'\Delta p'\rangle_{pat}\right]R_{C_T:N}
\end{aligned}
\tag{5.18}
$$

$$
\begin{aligned}
\left[\frac{d\langle N'P'\rangle_{pat}}{dt}\right]_{bio} &= \nu\frac{\langle N\rangle_{pat}}{\langle N\rangle_{pat}+k}\left(\langle N'P'\rangle_{pat} - \langle P'^2\rangle_{pat}\right) + \nu k\frac{\langle P\rangle_{pat}}{(\langle N\rangle_{pat}+k)^2}\left(\langle N'^2\rangle_{pat} - \langle N'P'\rangle_{pat}\right) + \\
&\quad - m\langle N'P'\rangle_{pat} \\
\left[\frac{d\langle N'\Delta p'\rangle_{pat}}{dt}\right]_{bio} &= \left[\frac{d\langle N'\Delta p'\rangle_{pat}}{dt}\right]_{flux} + \left[\frac{d\langle N'\Delta p'\rangle_{pat}}{dt}\right]_{upt} = \\
&= -\phi\frac{K_o K_g}{h}\langle N'\Delta p'\rangle_{pat} - \nu\frac{\langle N\rangle_{pat}}{\langle N\rangle_{pat}+k}\left(\langle P'\Delta p'\rangle_{pat} + \frac{\phi}{\rho}\langle N'P'\rangle_{pat}R_{C_T:N}\right) + \\
&\quad - \nu k\frac{\langle P\rangle_{pat}}{(\langle N\rangle_{pat}+k)^2}\left(\langle N'\Delta p'\rangle_{pat} + \frac{\phi}{\rho}\langle N'^2\rangle_{pat}R_{C_T:N}\right) \\
\left[\frac{d\langle P'\Delta p'\rangle_{pat}}{dt}\right]_{bio} &= \left[\frac{d\langle P'\Delta p'\rangle_{pat}}{dt}\right]_{flux} + \left[\frac{d\langle P'\Delta p'\rangle_{pat}}{dt}\right]_{upt} = \\
&= -\phi\frac{K_o K_g}{h}\langle P'\Delta p'\rangle_{pat} + \nu\frac{\langle N\rangle_{pat}}{\langle N\rangle_{pat}+k}\left(\langle P'\Delta p'\rangle_{pat} - \frac{\phi}{\rho}\langle P'^2\rangle_{pat}R_{C_T:N}\right) + \\
&\quad + \nu k\frac{\langle P\rangle_{pat}}{(\langle N\rangle_{pat}+k)^2}\left(\langle N'\Delta p'\rangle_{pat} - \frac{\phi}{\rho}\langle N'P'\rangle_{pat}R_{C_T:N}\right) + \\
&\quad - m\langle P'\Delta p'\rangle_{pat}
\end{aligned}
\tag{5.19}
$$

Obtained results are an extension of the model introduced by [28], in fact terms involving phytoplankton and nutrient coincide.

5.3.4 Summary

A final summary of the statistical model describing phytoplankton, nutrient and carbon interactions in a changing Lagrangian water patch.

$$\begin{aligned}
\frac{d\langle N\rangle_{pat}}{dt} &= \left[\frac{d\langle N\rangle_{pat}}{dt}\right]_{sur} + \left[\frac{d\langle N\rangle_{pat}}{dt}\right]_{bio} \\
\frac{d\langle P\rangle_{pat}}{dt} &= \left[\frac{d\langle P\rangle_{pat}}{dt}\right]_{sur} + \left[\frac{d\langle P\rangle_{pat}}{dt}\right]_{bio} \\
\frac{d\langle \Delta p\rangle_{pat}}{dt} &= \left[\frac{d\langle \Delta p\rangle_{pat}}{dt}\right]_{sur} + \left[\frac{d\langle \Delta p\rangle_{pat}}{dt}\right]_{bio}
\end{aligned} \tag{5.20}$$

$$\begin{aligned}
\frac{d\langle N'^2\rangle_{pat}}{dt} &= \left[\frac{d\langle N'^2\rangle_{pat}}{dt}\right]_{sur} + \left[\frac{d\langle N'^2\rangle_{pat}}{dt}\right]_{mix} + \left[\frac{d\langle N'^2\rangle_{pat}}{dt}\right]_{bio} \\
\frac{d\langle P'^2\rangle_{pat}}{dt} &= \left[\frac{d\langle P'^2\rangle_{pat}}{dt}\right]_{sur} + \left[\frac{d\langle P'^2\rangle_{pat}}{dt}\right]_{mix} + \left[\frac{d\langle P'^2\rangle_{pat}}{dt}\right]_{bio} \\
\frac{d\langle \Delta p'^2\rangle_{pat}}{dt} &= \left[\frac{d\langle \Delta p'^2\rangle_{pat}}{dt}\right]_{sur} + \left[\frac{d\langle \Delta p'^2\rangle_{pat}}{dt}\right]_{mix} + \left[\frac{d\langle \Delta p'^2\rangle_{pat}}{dt}\right]_{bio}
\end{aligned} \tag{5.21}$$

$$\begin{aligned}
\frac{d\langle N'P'\rangle_{pat}}{dt} &= \left[\frac{d\langle N'P'\rangle_{pat}}{dt}\right]_{sur} + \left[\frac{d\langle N'P'\rangle_{pat}}{dt}\right]_{mix} + \left[\frac{d\langle N'P'\rangle_{pat}}{dt}\right]_{bio} \\
\frac{d\langle N'\Delta p'\rangle_{pat}}{dt} &= \left[\frac{d\langle N'\Delta p'\rangle_{pat}}{dt}\right]_{sur} + \left[\frac{d\langle N'\Delta p'\rangle_{pat}}{dt}\right]_{mix} + \left[\frac{d\langle N'\Delta p'\rangle_{pat}}{dt}\right]_{bio} \\
\frac{d\langle P'\Delta p'\rangle_{pat}}{dt} &= \left[\frac{d\langle P'\Delta p'\rangle_{pat}}{dt}\right]_{sur} + \left[\frac{d\langle P'\Delta p'\rangle_{pat}}{dt}\right]_{mix} + \left[\frac{d\langle P'\Delta p'\rangle_{pat}}{dt}\right]_{bio}
\end{aligned} \tag{5.22}$$

Chapter 6

Phytoplankton CR model simulation

For now, let's consider the statistical model applied to a Lagrangian system containing only nutrient N and phytoplankton P, neglecting carbon dynamic. Equations (5.20), (5.21) and (5.22) regarding N and P form a system of five equations, which conceptually extend the simple model of Chapter 2. Consistence between the two descriptions can be found only in the case of vanishing variances and covariances, or more simply in the case of zeroth order truncation of the closure method (4.23). Otherwise, stationary behavior of the statistical model can differ significantly, involving variances and covariance steadily different from zero. We make now a comparison between these two cases, referring to them as "homogeneous statistical model" and "heterogeneous statistical model", understanding how allowed heterogeneity modifies the entity of nutrient-phytoplankton interaction.

6.1 Homogeneous case

In the simple model, the water patch is surrounded by a uniform reservoir with concentrations N_{out} and P_{out}, while in the Lagrangian statistical model, surroundings are distinct by region. A connection between the two descriptions can be reached defining $N_{out}(t)$ and $P_{out}(t)$ as the average surrounding concentrations of nutrient and phytoplankton experienced by the Lagrangian system as the patch evolve

$$\begin{aligned} N_{out}(t) &= \frac{\Omega^h(t)}{\Omega(t)}\langle N_h\rangle_{suh} + \frac{1}{2}\frac{\Omega^v(t)}{\Omega(t)}(\langle N_a\rangle_{sua} + \langle N_b\rangle_{sub}) \\ P_{out}(t) &= \frac{\Omega^h(t)}{\Omega(t)}\langle P_h\rangle_{suh} + \frac{1}{2}\frac{\Omega^v(t)}{\Omega(t)}(\langle P_a\rangle_{sua} + \langle P_b\rangle_{sub}) \end{aligned} \tag{6.1}$$

where time dependent Ω and its components are defined by (3.21), (3.22). With this notation, equations (5.20) for N and P means become superimposable to the one of the simple model (2.1). Their expressions are indeed

$$\begin{cases} \dfrac{d\langle N\rangle_{pat}(t)}{dt} = -\nu\dfrac{\langle N\rangle_{pat}(t)}{\langle N\rangle_{pat}(t)+k}\langle P\rangle_{pat}(t) + \Omega(t)(N_{out}(t) - \langle N\rangle_{pat}) \\ \dfrac{d\langle P\rangle_{pat}(t)}{dt} = \nu\dfrac{\langle N\rangle_{pat}(t)}{\langle N\rangle_{pat}(t)+k}\langle P\rangle_{pat}(t) - m\langle P\rangle_{pat}(t) + \Omega(t)(P_{out}(t) - \langle P\rangle_{pat}(t)) \end{cases} \tag{6.2}$$

The only modification with respect to (2.1) is the presence of time dependent entrainment rate and outside concentrations, which is the result of the water patch physical modelling. This dynamical

system equilibrium changes indeed in time, making it hard to identify the steady state. At a given time t, system's feasible fixed point $(\langle N\rangle^*_{pat}(t), \langle P\rangle^*_{pat}(t))$ have the expression already found in (2.11).

In Fig. 6.1A we show how the initial mean concentrations evolve towards the equilibrium $(\langle N\rangle^*_{pat}(t)$, $\langle P\rangle^*_{pat}(t))$, which in turn moves as time goes on.

6.2 Heterogeneous case

Describing now also the second moments of the tracer distributions, we have to deal with a system of five equations from (5.20), (5.21) and (5.22). Surrounding terms for variances and covariances cannot be written in a simple way as (6.1), so we maintain an implicit expression.

$$\begin{aligned}
\frac{d\langle N\rangle_{pat}}{dt} &= \Omega(t)(N_{out}(t) - \langle N\rangle_{pat}) + \left[\frac{d\langle N\rangle_{pat}}{dt}\right]_{bio} \\
\frac{d\langle P\rangle_{pat}}{dt} &= \Omega(t)(P_{out}(t) - \langle P\rangle_{pat}) + \left[\frac{d\langle P\rangle_{pat}}{dt}\right]_{bio} \\
\frac{d\langle N'^2\rangle_{pat}}{dt} &= \left[\frac{d\langle N'^2\rangle_{pat}}{dt}\right]_{sur} + \left[\frac{d\langle N'^2\rangle_{pat}}{dt}\right]_{mix} + \left[\frac{d\langle N'^2\rangle_{pat}}{dt}\right]_{bio} \\
\frac{d\langle P'^2\rangle_{pat}}{dt} &= \left[\frac{d\langle P'^2\rangle_{pat}}{dt}\right]_{sur} + \left[\frac{d\langle P'^2\rangle_{pat}}{dt}\right]_{mix} + \left[\frac{d\langle P'^2\rangle_{pat}}{dt}\right]_{bio} \\
\frac{d\langle N'P'\rangle_{pat}}{dt} &= \left[\frac{d\langle N'P'\rangle_{pat}}{dt}\right]_{sur} + \left[\frac{d\langle N'P'\rangle_{pat}}{dt}\right]_{mix} + \left[\frac{d\langle N'P'\rangle_{pat}}{dt}\right]_{bio}
\end{aligned} \tag{6.3}$$

Water patch movements, and the consequent time dependent $\Omega(t)$, determine the presence of time dependent stationary solutions $(\langle N\rangle^*_{pat}(t), \langle P\rangle^*_{pat}(t)$, $\langle N'^2\rangle^*_{pat}(t), \langle P'^2\rangle^*_{pat}(t), \langle N'P'\rangle^*_{pat}(t))$ difficult to quantify and find analytically. The complexity of this dynamical system of five independent variables may allow very intricate behaviors and multiple stable or unstable equilibria, but in this work we are not specifically interested on that.

Qualitatively, we expect that, if second moments stay limited in time, the dynamic in the phase space will converge to a temporary equilibrium, which may surely be different from the one found for $\langle N\rangle^*_{pat}(t)$ and $\langle P\rangle^*_{pat}(t)$ in the homogeneous case. This is in fact what happens in Fig. 6.1B, where the ending point in the N-P phase space does not match the same of the homogeneous case, even if the distance is not so high.

Interestingly, starting with the same parameters and initial conditions, homogeneous and heterogeneous statistical models can give rise to very different transient behaviors, resulting in different heights of phytoplankton peaks (Fig. 6.2). In this specific scenario, the peak displayed in the homogeneous case is bigger than the one in the heterogeneous case, but this can really change with different parameters value involved. The keep-in-mind message here, is that by fitting the initial phytoplankton growth one has to pay attention to presence of heterogeneity, which can really drift the size of the bloom generated.

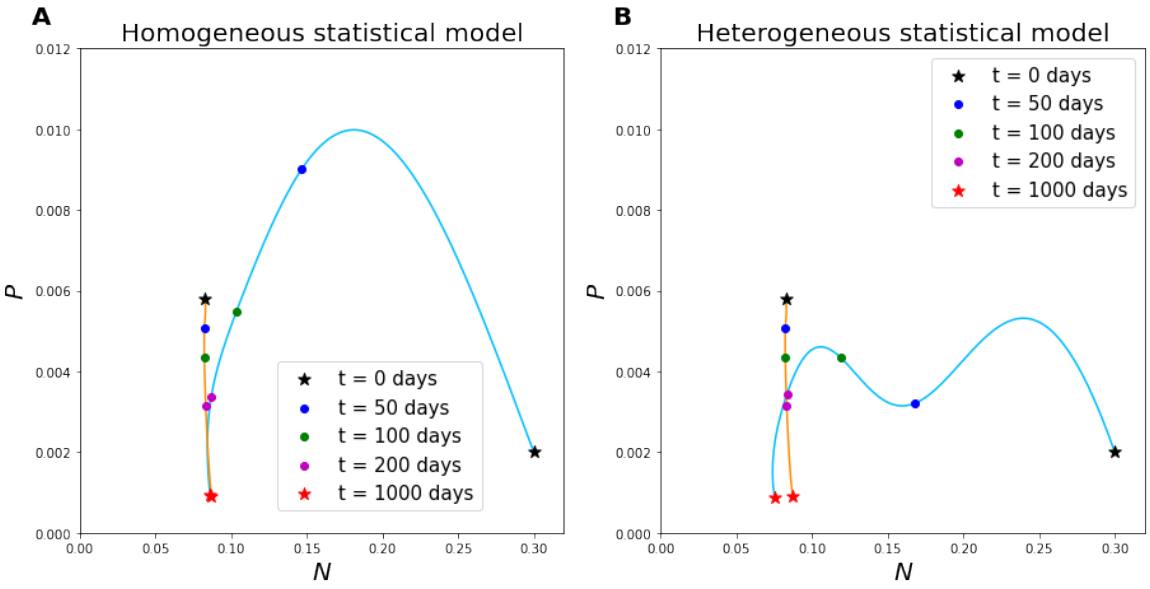

Figure 6.1: Comparison between homogeneous (6.2) and heterogeneous (6.3) model dynamic at stationary. Light blue curves represent $(\langle N\rangle_{pat}(t), \langle P\rangle_{pat}(t))$ trajectories, while orange curve is $(\langle N\rangle^*_{pat}(t), \langle P\rangle^*_{pat}(t))$ trajectory in the homogeneous case. In panel **A**, dynamic is brought towards the expected stationary values. In panel **B**, convergence of the light blue line is not in the same location, meaning that the stationary point in the heterogeneous case is different. Parameters in the two cases are the same: in particular $\nu = 0.8$, $m = 0.1$, $k = 1.73$, $\gamma_0 = 0.012$, $\kappa_0^h = 0.01$, $\kappa_0^h = 2.07 \cdot 10^{-6}$, $\delta_0 = 1 \cdot 10^{-4}$ (see table 7.1 for unit of measure). Initial patch size is $W(0) = 1$, $L(0) = 1$, $T(0) = 0.03$. Black stars are initial values of N and P, while red stars are computed after 1000 days.

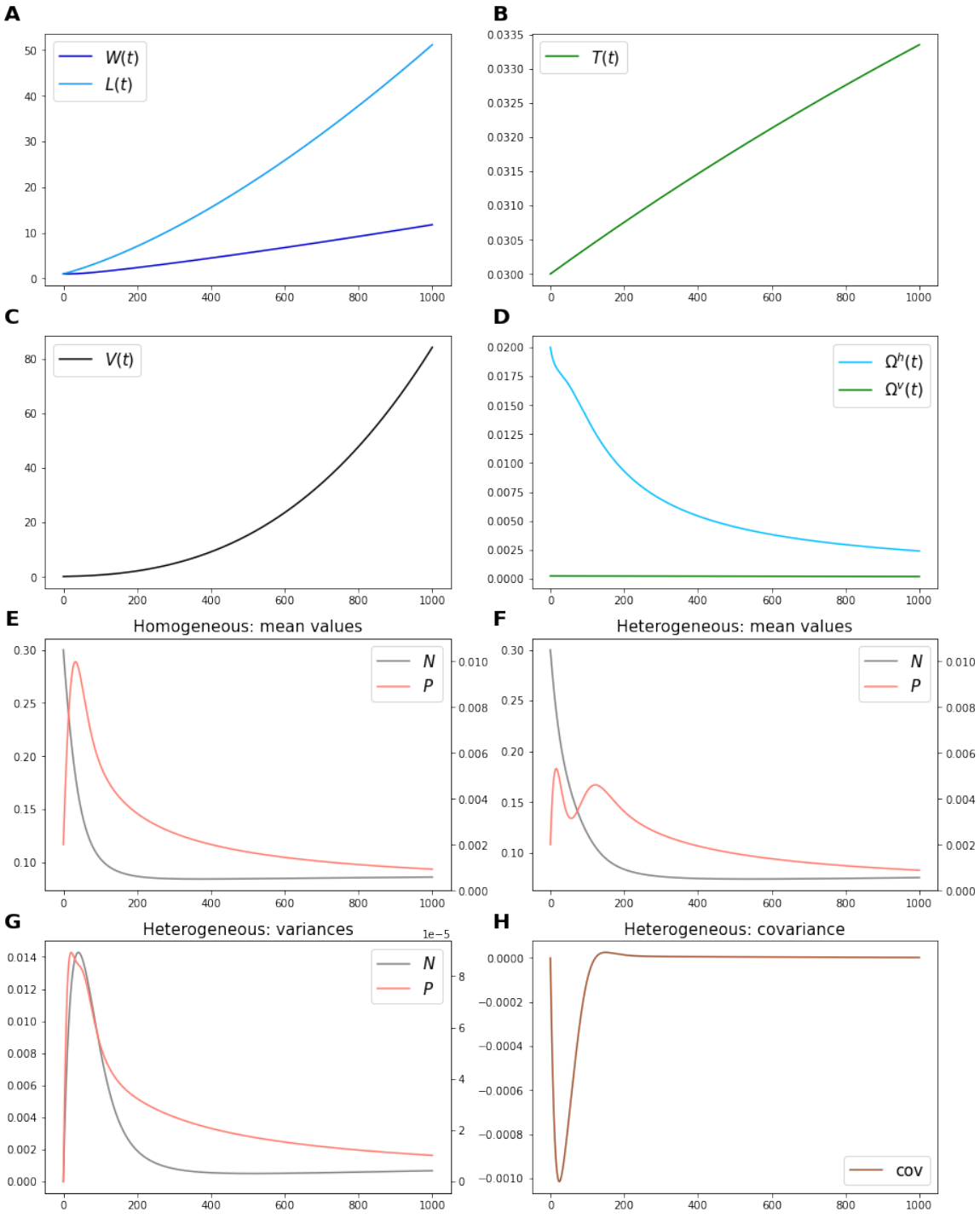

Figure 6.2: Time evolution of the quantities of interest related to the homogeneous and heterogeneous model. Panels **A**, **B** and **C** represent the evolutions of width, length, thickness and volume of the water patch. Their behavior is ruled by the fluid dynamical parameters γ_0, δ_0, κ_0^h and κ_0^v. Panel **D** represent the evolutions of the two components of the entrainment rate. Panels **E** and **F** contain the two dynamics predicted by homogeneous and heterogeneous model about the means of nutrient and phytoplankton inside the patch. In particular, phytoplankton mean concentrations display a different behavior in the transient phase. Panels **G** and **H** hold the predicted nutrient and phytoplankton variances and covariance in the heterogeneous case (they will be identically zero, otherwise). Stationary values are finite and non-zero. In panels **E**, **F**, **G** nutrient's y-axis is on the left, while phytoplankton's y-axis is on the right.

Chapter 7

SOIREE experiment simulation

7.1 The SOIREE experiment

The Southern Ocean is known to be rich in nutrients like nitrate and phosphate, but often limited by iron availability. Iron is a crucial micro-nutrient for phytoplankton growth, and its scarcity in these waters restricts primary productivity. This makes potentially this ocean site one of the largest repository of unused resources on the earth [4]. The Southern Ocean is also thought to have a fundamental role in regulating the global carbon cycle in both present and past times. Studies related to the Last Glacial Maximum suggest that export production was very big in these waters, likely because of more iron being available.

All these reasons brought a team of scientists, overseen by Dr. Philip Boyd and Dr. Rob Armstrong, to conduct an iron enrichment experiment in the waters of the Southern Ocean, called SOIREE "Southern Ocean Iron RElease Experiment" [5], in February 1999. A large amount of acidified ferrous sulfate $FeSO_4 \cdot 7H_2O$ was released, together with the tracer sulfur hexafluoride SF_6, into the mixed layer region over an initial area of about 50 km^2. The evolution of this water patch was monitored for about 40 days, allowing researchers to measure important physical and biochemical quantities such as iron dispersal concentration, chlorophyll concentration, stirring and dilution rates, carbon uptake rates, and many others [1].

Here, we want to model the experiment to assess the validity of the statistical approach introduced, also predicting some properties that unfortunately has not been measured, like tracers variances and covariances.

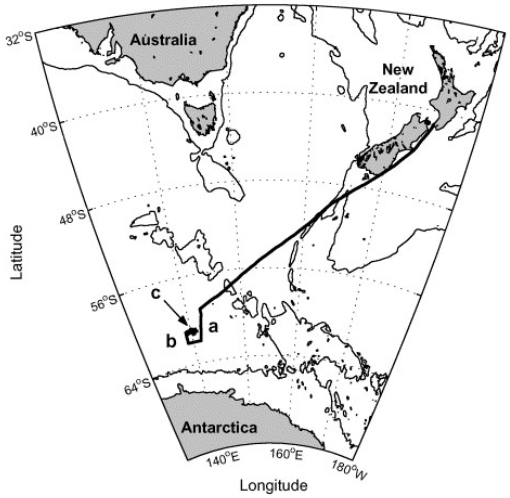

Figure 7.1: Location of the SOIREE experiment [5]

7.2 Environmental parameters setup

We are interested in describing how iron and phytoplankton concentrations, as well as pCO_2 level, vary during the 42 days of water patch tracking. In situ measurements [1], [13] are compared with the predicted evolution, both with regard to the physical patch enlargement that to phytoplankton bloom size. Also carbon uptake, in terms of Δp, is considered with respect to available data [18] and more advanced designs like the SWAMCO model [19], [17].

Physical parameters like strain rate, divergence and diffusivities observed during the experiment are retrieved from [1], [13]. Biological growth and death rates ν, m, as well as the half saturation constant k, are manually tuned to match with the experimental bloom size. Finally, information related to carbon parameters can be found from different sources [21], [13], [35], [25], [19] (see Tab. 7.1).

parameter	**value**	**unit of measure**
γ_0	0.12	day^{-1}
δ_0	$3 \cdot 10^{-6}$	day^{-1}
κ_0^h	0.10	$\text{km}^2 \cdot \text{day}^{-1}$
κ_0^v	$2.1 \cdot 10^{-6}$	$\text{km}^2 \cdot \text{day}^{-1}$
ν	0.40	day^{-1}
k	1.73	$(\mu\text{mol Fe}) \cdot \text{m}^{-3}$
m	0.05	day^{-1}
ϕ	1.64	$\mu\text{atm} \cdot \text{kg} \cdot (\mu\text{mol C})^{-1}$
K_o	0.06	$(\mu\text{mol C}) \cdot \text{kg}^{-1} \cdot \mu\text{atm}^{-1}$
K_g	17.28	$\text{m} \cdot \text{day}^{-1}$
h	65	m
ρ	1027	$\text{kg} \cdot \text{m}^{-3}$
B	10	#
$R_{C_T:Fe}$	$6 \cdot 10^4$	$(\mu\text{mol C}) \cdot (\mu\text{mol Fe})^{-1}$

Table 7.1: Set of parameters used to simulate the SOIREE experiment

Initial conditions of the water patch and of the tracer concentrations are set to mimic the environment where the iron release took place [1], [13], [11]. Moreover, the assumptions that have been made are that above and horizontal surroundings display the same tracer concentrations, while below the patch no presence of phytoplankton is allowed. Regarding the pCO_2 anomaly, it is set to be initially zero inside and outside the patch, since the gas is thought to be in equilibrium.

The mean value of the pCO_2 anomaly $\langle \Delta p \rangle_{pat}$ would theoretically depend on variations of the patch temperature $\bar{\mathcal{T}}$ as set in the equation (5.17). Due to the lack of consistent data among the entire realization of the experiment, we will consider $\bar{\mathcal{T}}$ approximately constant in time, so $d\bar{\mathcal{T}}/dt = 0$.

7.3 Simulation results

The simulation is performed for 42 days, starting with a massive iron release in a circular water patch of radius equal to 5 km. The action of strain, divergence and diffusion brings to an increase of the size of the patch on the y-axis, reaching about 75 km on the last day (Fig. 7.2A). Patch width initially decreases due to the stirring effect, but then stabilizes at around 4 km. Low values of vertical diffusivity and divergence (there is no consistent upwelling) determine a very soft increase in the patch thickness, rising from 30 to 32.5 m (Fig. 7.2B). In its entirety, the total volume grows by a factor of 15, mainly due to horizontal intrusion of water (Fig. 7.2C, 7.2D). In particular, it's interesting to notice that horizontal entrainment rate peaks around day 20, which correspond to the minimum of the patch width. Vertical entrainment is again limited by the small diffusivity and divergence.

variable	value	unit of measure
$W(0)$	5	km
$L(0)$	5	km
$T(0)$	30	m
$\langle N \rangle_{pat}(0)$	3.45	$(\mu\text{mol Fe}) \cdot \text{m}^{-3}$
$\langle P \rangle_{pat}(0)$	0.0249	$(\mu\text{mol Fe}) \cdot \text{m}^{-3}$
$\langle \Delta p \rangle_{pat}(0)$	0	μatm
$\langle N^h \rangle_{suh}(0)$	0.08	$(\mu\text{mol Fe}) \cdot \text{m}^{-3}$
$\langle P^h \rangle_{suh}(0)$	0.0249	$(\mu\text{mol Fe}) \cdot \text{m}^{-3}$
$\langle \Delta p^h \rangle_{suh}(0)$	0	μatm
$\langle N^a \rangle_{sua}(0)$	0.08	$(\mu\text{mol Fe}) \cdot \text{m}^{-3}$
$\langle P^a \rangle_{sua}(0)$	0.0249	$(\mu\text{mol Fe}) \cdot \text{m}^{-3}$
$\langle \Delta p^a \rangle_{sua}(0)$	0	μatm
$\langle N^b \rangle_{sub}(0)$	0.30	$(\mu\text{mol Fe}) \cdot \text{m}^{-3}$
$\langle P^b \rangle_{sub}(0)$	0	$(\mu\text{mol Fe}) \cdot \text{m}^{-3}$
$\langle \Delta p^b \rangle_{sub}(0)$	0	μatm

Table 7.2: Initial environmental conditions used to simulate the SOIREE experiment. Internal and external variances and covariances are initially set to zero and are not reported for compactness.

Heterogeneous simulation Initial iron concentration inside the patch is on average about 40 times higher than the environmental concentration, generating a strong gradient with the outside, which also enhance spatial heterogeneity. Iron decay is at first strengthen by intrusion of surrounding water (Fig. 7.3E), but then also biological consumption starts to play a role. Phytoplankton generated bloom, in fact, peaks on its average after around 20-25 days, at a time when mean iron concentration is already quite low (Fig. 7.3A). Even phytoplankton mean decay, at that point, is principally due to dilution (Fig. 7.3F).

Variances of iron and phytoplankton display an interesting behavior, since the iron one peaks first, while the phytoplankton one follows with a delay of about 10 days (Fig. 7.3B). Their values are pretty high with respect to what is allowed by the closure method of Section 4.6, and this indicates that possibly taking account of higher moments would be beneficial. Anyway, this behavior is mainly motivated by the strong initial gradient, and would not appear for initial conditions more similar to the environment. Figures 7.3G and 7.3H show that iron variance is only fed by the discrepancy with the surroundings, while biological uptake acts reducing heterogeneity. The opposite happens for phytoplankton variance, where consumption is linked to an enhancement of heterogeneity. In general, all mixing terms appear to be quantitatively negligible, and this could be due to a too much high characteristic time of decay. Future clarification will be needed to assess this hypothesis.

The covariance between iron and phytoplankton is expressed in terms of Pearson correlation (Fig. 7.3C), that is defined as

$$r(u_i, u_j)_{pat} = \frac{\langle u_i' u_j' \rangle_{pat}}{\sqrt{\langle u_i'^2 \rangle_{pat} \cdot \langle u_j'^2 \rangle_{pat}}} \tag{7.1}$$

and can assume values between -1 and 1. In the first part of planktonic growth, iron-phytoplankton correlation stays positive and near 1, meaning perfect correspondence between high level of phytoplankton and high levels of iron available. After phytoplankton peak, the correlation drops down and becomes negative in the final part, and this is probably related to phytoplankton overexploitation of iron-rich areas.

CO_2 sequestration inside the water patch is connected to the dynamic of the pCO_2 anomaly, that is Δp. Mean value of the latter resembles, in a rather satisfactory manner, partial pressure anomalies

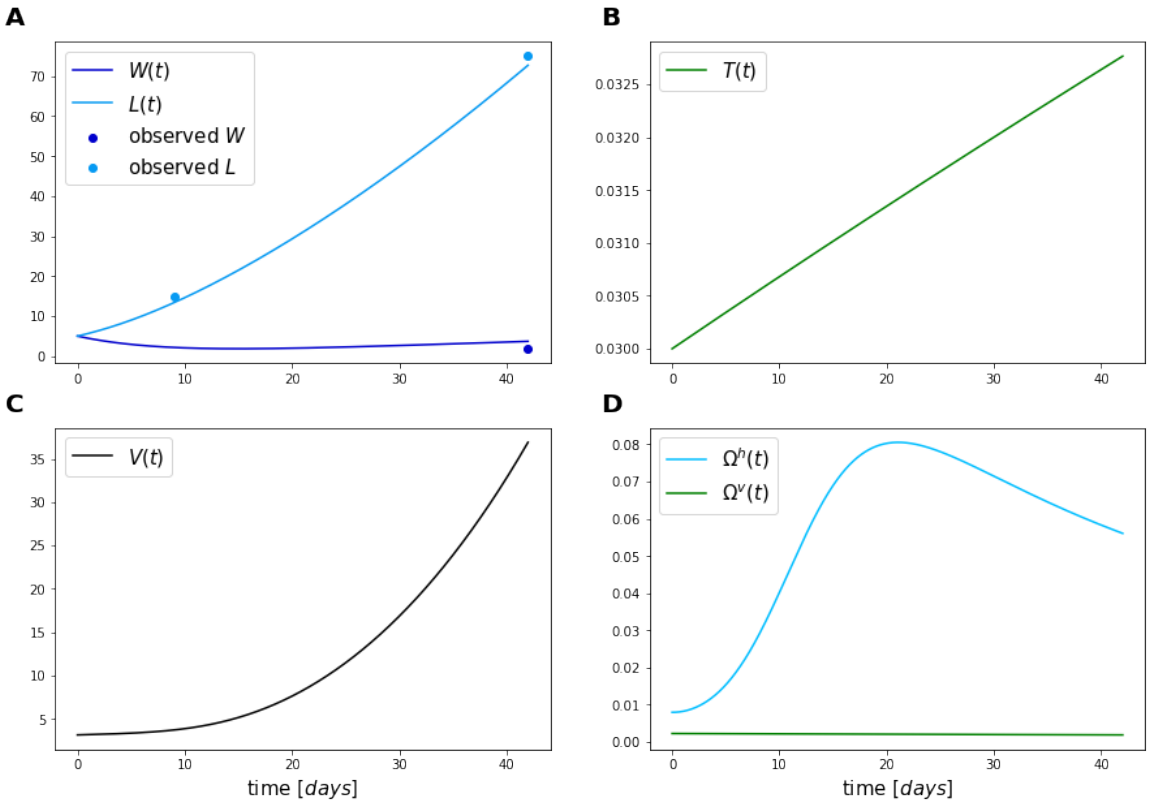

Figure 7.2: Simulation of the SOIREE water patch evolution, starting from a circular water patch with radius of 5 km and thickness of 30 m. Predicted and measured width and length of the patch are depicted in panel **A**, thickening process in panel **B**, while total volume increase in panel **C**. Horizontal and vertical entrainment rates, obtained from relative volume changes, are represented in panel **D**.

encountered in data collected the first 13 days inside the patch (the bottom part of the gray cloud, Fig. 7.4A). With respect to the SWAMCO prediction, the minimum of the pCO_2 anomaly occurs around 10 days before, in coincidence phytoplankton maximum concentration in our model. From Fig. 7.4B, it can be seen how important is to model entrainment and air-sea exchange in order to do not overestimate carbon uptake.

Spatial variance of Δp rise quickly after 15 days and reach a very high value ($\sqrt{\langle \Delta p'^2 \rangle_{pat}(peak)} \simeq$ 118 μatm), meaning that in some regions pCO_2 anomaly may even be positive (Fig. 7.4C). The only term in Fig. 7.4D enhancing heterogeneity is the biological uptake of carbon, while the others tend to flatten the Δp distribution.

Finally, correlations of N and P with Δp are depicted in Figures 7.4E and 7.4G. The first one start negative and, symmetrically to $r(N,P)_{pat}$, flips to positive in the final part of the experiment. This is expected, since phytoplankton growth implies carbon uptake. The second one, instead, stays perfectly negative from the beginning, and this is completely fair for the same reason.

Homogeneous simulation Accounting only for mean concentrations of the tracers involved, a consistent part of the system's behavior is preserved, but with some important differences. In the same conditions, in fact, the generated phytoplankton bloom has a more modest size (Fig. 7.5A) despite fitting quite well data related to the initial increase. This impacts also on the amount of pCO_2 anomaly, which seems underestimated in absolute value with respect to the SWAMCO prediction. All these observations suggest that, in particular for SOIREE simulation, introducing spatial variances and covariances in the description helps to achieve a better representation of the system. However, given the sparsity of the observations, we cannot fully support statistically this claim.

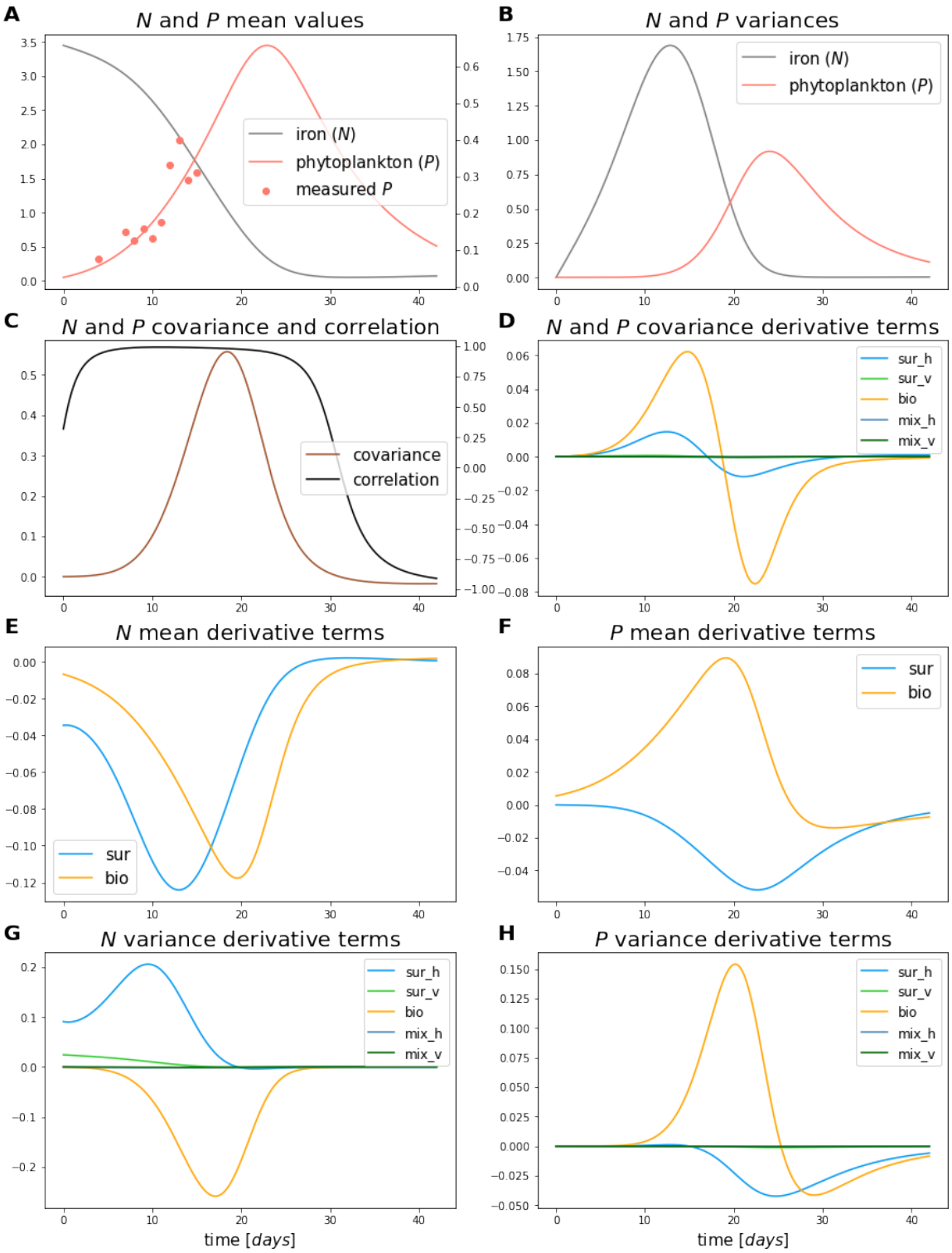

Figure 7.3: Simulation of the SOIREE tracers with the statistical model, accounting for heterogeneity. In panels **A** and **B** are represented iron and phytoplankton concentrations means and variances, respectively. Iron-phytoplankton covariance and correlation, defined in (7.3), and covariances derivative terms of equation (5.22) are depicted in panels **C** and **D**. Mean derivative terms for iron and phytoplankton of (5.20) are present in panels **E** and **F**, as well as variance derivative terms (5.21) in panels **G** and **H**. See text for a complete analysis. In panel **C**, note that the left y-axis is for covariance, while the right y-axis is for correlation.

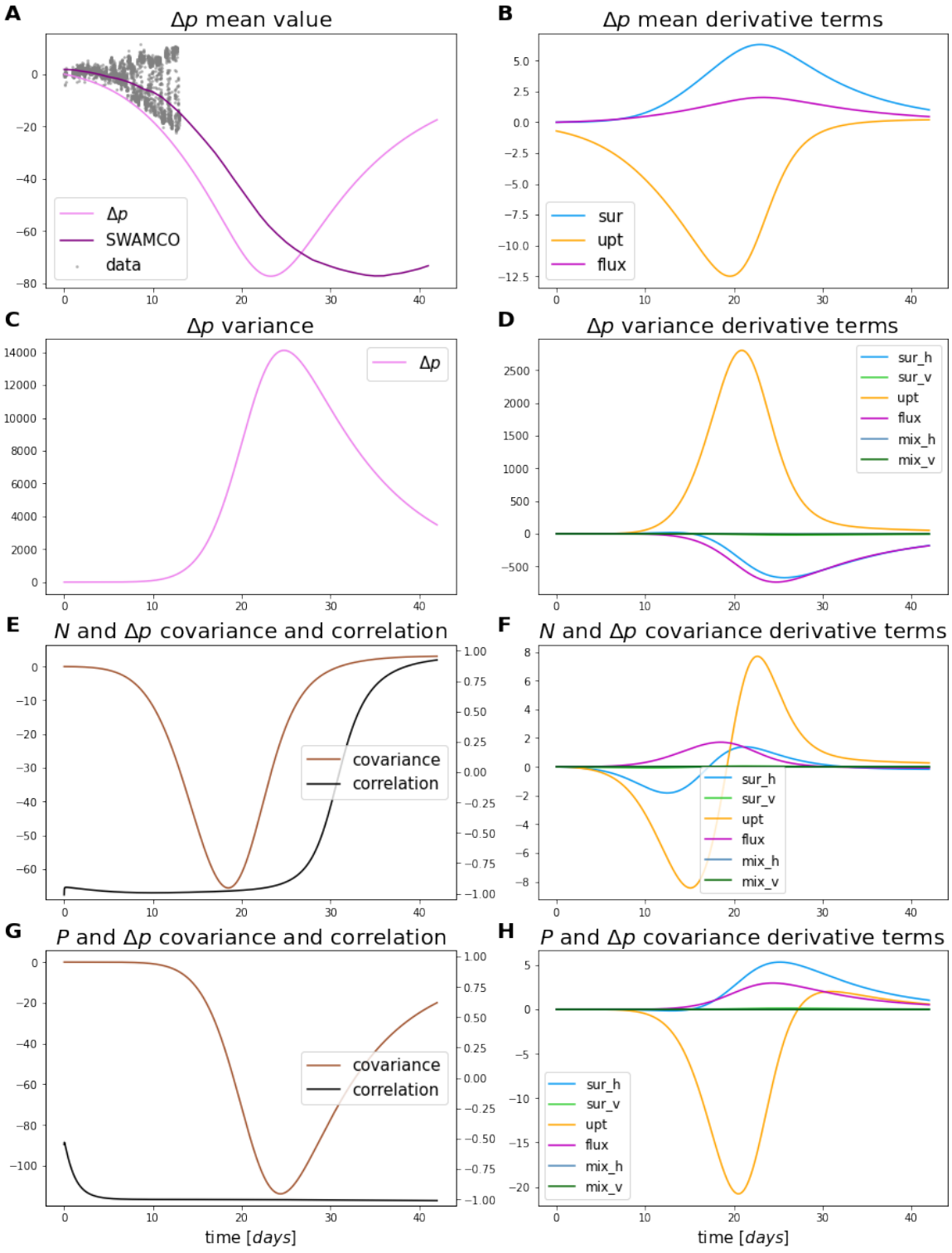

Figure 7.4: Simulation of the SOIREE tracers with the statistical model, accounting for heterogeneity. In panel **A** is represented mean pCO_2 anomaly, that is compared with SWAMCO model prediction on available data. Only the bottom part of the gray points is related to the anomaly inside the patch, while the upper regards measurements made in the surrounding. Panels **C**, **E** and **G** depict, respectively, Δp variance, iron-Δp covariance-correlation and phytoplankton-Δp covariance-correlation. On the right, all the derivative terms present in the full model equations (5.20), (5.21), (5.22) are shown in panels **B**, **D**, **F** and **H**. In panels **E** and **G**, note that the left y-axis is for covariance, while the right y-axis is for correlation. See text for complete analysis.

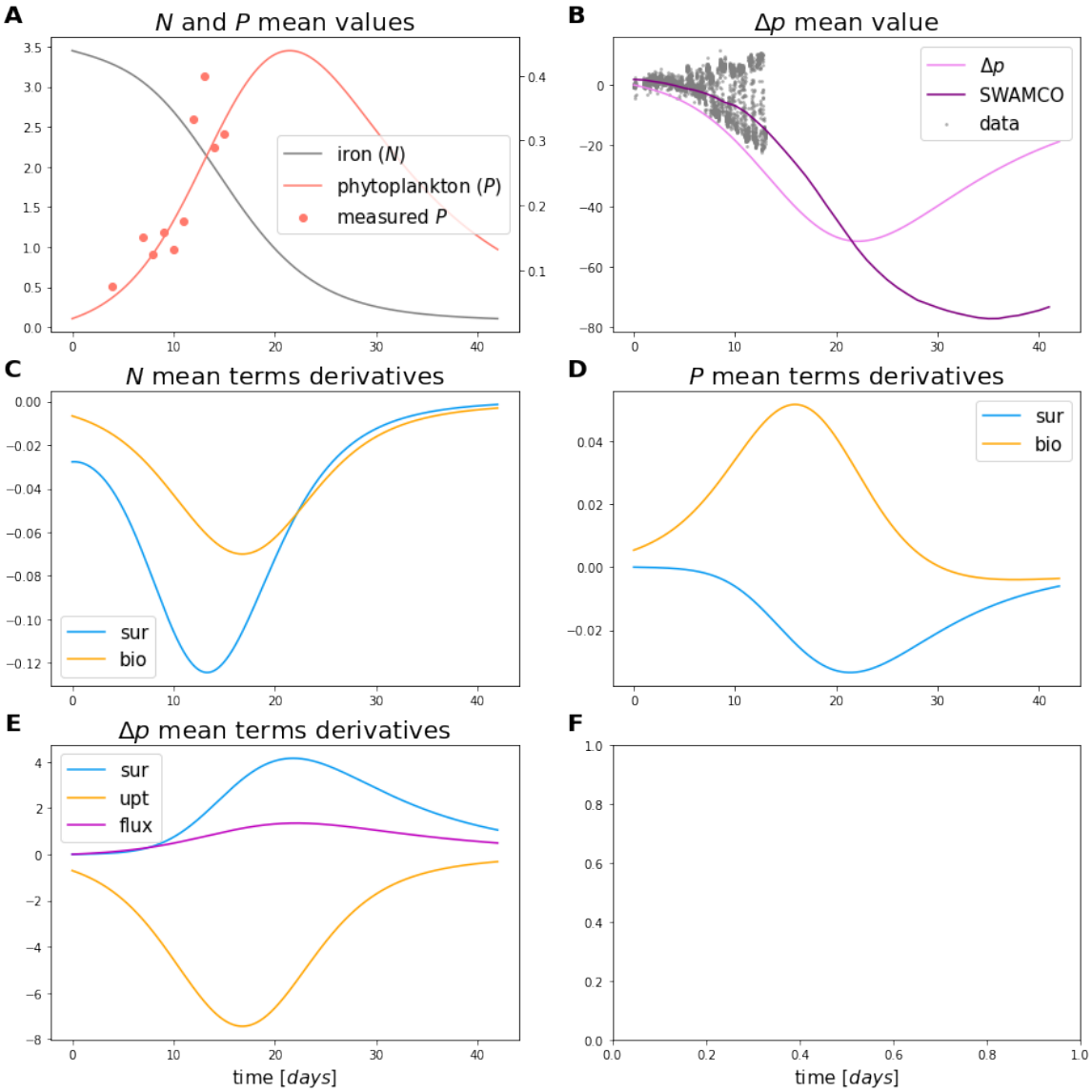

Figure 7.5: Simulation of the SOIREE tracers within the statistical model, in the simplified homogeneous case. In panel **A** is represented iron and phytoplankton concentrations means, while in panel **B** the mean pCO_2 anomaly, that is compared with SWAMCO model prediction on available data. Only the bottom part of the gray points is related to the anomaly inside the patch, while the upper regards measurements made in the surrounding. Mean derivative terms for N, P and Δp are depicted, respectively, in panels **C**, **D** and **E**. See text for complete analysis.

Chapter 8

Eddies in the Southern Ocean

Mesoscale eddies are coherent vortices with a rotational core, usually have a long life cycle of weeks or months and transport heat, salt, and other passive tracers over long distances [34]. They exist ubiquitously in the global ocean and can influence biogeochemical cycling through horizontal and vertical transport of water masses with different physical and biogeochemical characteristics [22]. Recent satellite observations have revealed that the world ocean surfaces are mostly occupied by oceanic mesoscale eddies and, in the Southern Ocean, eddy activity is particularly high [8].

The presence of mesoscale eddies at a given spatial scale can allow the formation of some mechanism of physical-biological interaction. First of all, eddy stirring, driven by turbulent advection, can promote high levels of heterogeneity and patchiness in nutrients and microorganisms concentrations in a given region of the ocean. Secondly, non-linear eddies can trap some fluid within their interiors, maintaining distinct physical, chemical, and biological properties over long periods [23]. These factors suggest that a Lagrangian description for this kind of systems is suitable.

We know also that cyclonic and anticyclonic eddies induce nutrient uplift and downwelling, depending on the eddy's developmental stage. This process can alter nutrient availability in the euphotic zone, influencing biological uptake of the present phytoplankton [23].

The objective is then to propose a first Lagrangian description for a mesoscale eddy, in which upwelling of nutrients is modelled by vertical dilution. Obtained results are still quite partial, since additional work is needed to characterize eddies specificities.

8.1 Non-rigid rotation effects

Let's consider a mesoscale eddy of horizontal elliptic shape of width $2W(t)$ and length $2L(t)$. We can assume that the water patch of interest is given by the resulting ellipsoid, obtained by accounting the whole mixed layer of depth $2T(t)$. The Lagrangian frame of reference is situated at the center of this ellipsoid and translates with it, absorbing the advection component of the global velocity field in that region. Local modification of the eddy-patch shape can be modeled through the following velocity field, that is an extension of (3.3) accounting for non-rigid body rotation

$$\begin{aligned} v_x(\mathbf{x},t) &= \left(-\gamma(t)+\frac{\delta(t)}{2}\right)x + \frac{\mathcal{A}y}{L^2(t)}\exp\left[-\frac{x^2}{2W^2(t)}-\frac{y^2}{2L^2(t)}\right] \\ v_y(\mathbf{x},t) &= \left(+\gamma(t)+\frac{\delta(t)}{2}\right)y - \frac{\mathcal{A}x}{W^2(t)}\exp\left[-\frac{x^2}{2W^2(t)}-\frac{y^2}{2L^2(t)}\right] \\ v_z(\mathbf{x},t) &= -\delta(t)z \end{aligned} \tag{8.1}$$

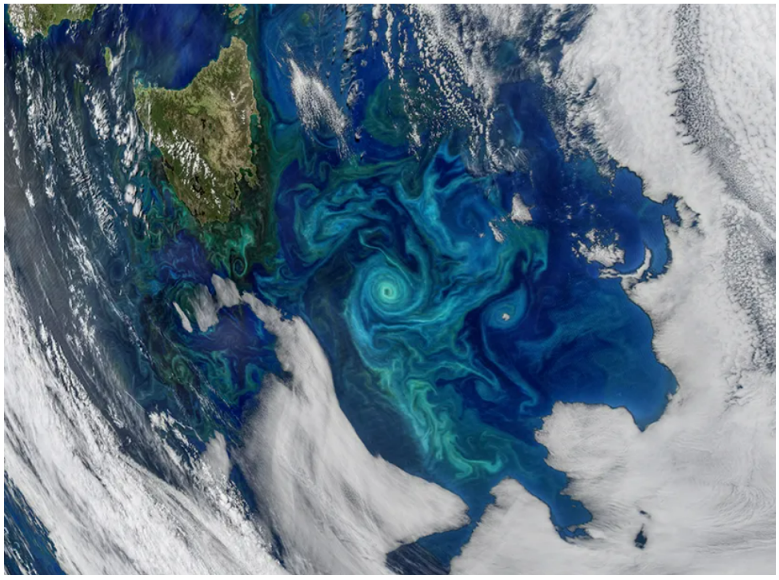

Figure 8.1: Phytoplankton bloom in the Tasman Sea captured by the NASA Moderate Resolution Imaging Spectroradiometer (MODIS) instrument on the Aqua satellite on 21 November 2017. Credit: NASA/Ocean Biology Processing Group, Goddard Space Flight Center.

This is, in fact, a composition between a 3D stagnation point flow, already mentioned in Section 3.3, and an eddy-like elliptical rotational flow [34]. Let's analyze the additive rotational terms. For $\mathcal{A} > 0$ we expect a clock-wise rotation, while for $\mathcal{A} < 0$ the spin is opposite. The intensity of the revolution speed has maximum value in the ellipse of semi-axes $W(t)$ and $L(t)$, but then decays by moving away to the center in a Gaussian manner. In its entirety, local velocity field is divergenceless, satisfying again fluid incompressibility ($\nabla \cdot \mathbf{v} = 0$).

It would be interesting, now, to employ the same formalism of Section 3.5 in order to measure the effect of the non-rigid body rotation on patch characteristic sizes $W(t)$, $L(t)$ and $T(t)$. Integrating the advection-diffusion equation (3.6) with local velocity field (8.1) one gets the following moments equations for the water patch distribution $\theta(\mathbf{x}, t)$

$$
\begin{aligned}
\frac{dM_0^x(t)}{dt} &= \left(-\gamma(t) + \frac{\delta(t)}{2}\right) M_0^x(t) + \int_{-\infty}^{+\infty} \frac{\mathcal{A}x}{L^2(t)} \exp\left[-\frac{x^2}{2W^2(t)} - \frac{y^2}{2L^2(t)}\right] \cdot \left.\frac{\partial \theta}{\partial y}\right|_{y,z=0} dx \\
\frac{dM_0^y(t)}{dt} &= \left(\gamma(t) + \frac{\delta(t)}{2}\right) M_0^y(t) - \int_{-\infty}^{+\infty} \frac{\mathcal{A}y}{W^2(t)} \exp\left[-\frac{x^2}{2W^2(t)} - \frac{y^2}{2L^2(t)}\right] \cdot \left.\frac{\partial \theta}{\partial x}\right|_{x,z=0} dy \qquad (8.2) \\
\frac{dM_0^z(t)}{dt} &= -\delta(t) M_0^z(t)
\end{aligned}
$$

$$
\begin{aligned}
\frac{dM_2^x(t)}{dt} &= +2\kappa^h(t) M_0^x(t) + 3\left(-\gamma(t) + \frac{\delta(t)}{2}\right) M_2^x(t) + \\
&\quad + \int_{-\infty}^{+\infty} \frac{\mathcal{A}x^3}{L^2(t)} \exp\left[-\frac{x^2}{2W^2(t)} - \frac{y^2}{2L^2(t)}\right] \cdot \left.\frac{\partial \theta}{\partial y}\right|_{y,z=0} dx \\
\frac{dM_2^y(t)}{dt} &= +2\kappa^h(t) M_0^y(t) + 3\left(\gamma(t) + \frac{\delta(t)}{2}\right) M_2^y(t) + \qquad (8.3) \\
&\quad - \int_{-\infty}^{+\infty} \frac{\mathcal{A}y^3}{W^2(t)} \exp\left[-\frac{x^2}{2W^2(t)} - \frac{y^2}{2L^2(t)}\right] \cdot \left.\frac{\partial \theta}{\partial x}\right|_{x,z=0} dy \\
\frac{dM_2^z(t)}{dt} &= +2\kappa^v(t) M_0^z(t) - 3\delta(t) M_2^z(t)
\end{aligned}
$$

in which integral terms are contributions coming from the rotational flow. Essentially, we found that non-rigid rotation can have an effect on the way patch shape modifies, and its evaluation depends on the specific formulation of those integrals. Their expressions are in general not so simple to manipulate as were (3.10) and (3.11), given the presence of θ derivate with respect to an axis that is not the one of integration. We need, then, to understand in which cases non-rigid rotation contribution can be neglected and what approximations are required.

8.2 Radial symmetry assumption

Let's now make the assumption of starting with a circular water patch ($W(0) = L(0)$) and that stirring is negligible (coherent eddy, $\gamma(t) = 0$). In this case, radial symmetry will be conserved among all the evolution in time, letting at most the circle to grow in radius $R(t) = W(t) = L(t)$ (Fig. 8.2). This is reflected also in the local velocity field, that becomes easily understandable in cylindrical coordinates

$$\begin{aligned} v_r(r,\varphi,z,t) &= \frac{\delta(t)}{2} r \\ v_\varphi(r,\varphi,z,t) &= \frac{\mathcal{A} r}{R^2(t)} \exp\left[-\frac{r^2}{2R^2(t)}\right] \\ v_z(r,\varphi,z,t) &= -\delta(t) z \end{aligned} \tag{8.4}$$

Divergence $\delta(t)$ acts in radial direction, while the rotational flow becomes a fully angular component of the velocity. This suggests that, if θ has radial symmetry ($\partial\theta/\partial\varphi = 0$), the advective term in cylindrical coordinates, that is

$$v_r \frac{\partial\theta}{\partial r} + v_\varphi \frac{1}{r}\frac{\partial\theta}{\partial\varphi} + v_z \frac{\partial\theta}{\partial z} \tag{8.5}$$

does not depend anymore on the expression of v_φ, which contains the rotational component. In other words, the advection-diffusion equation in cylindrical coordinates does not have any rotational term if the water patch distribution displays radial symmetry at any time t.

This request can be translated in cartesian coordinates, imposing $\partial\theta/\partial y|_{y,z=0} = 0$ and $\partial\theta/\partial x|_{x,z=0} = 0$ for any time t. These are the conditions that allow, indeed, to discard the integral terms of (8.2) and (8.3), making them equal to (3.10) and (3.11). Changes in $W(t)$, $L(t)$ and $T(t)$ will then be regulated by the same laws found in Section 3.5, but with $\gamma(t) = 0$.

8.3 Eddy simulation

We want to simulate the behavior of nutrient, phytoplankton and pCO_2 inside a mesoscale eddy, subject to an upwelling regime. The assumption is that radial symmetry is conserved during the whole eddy lifetime, considered to be around 45 days. In this specific case, non-rigid rotation doesn't enter in the equations of the moments (8.2), (8.3) and so there's no need to specify rotation intensity $\mathcal{A}$. We fix the origin of the Lagrangian frame of reference at the central point of the eddy, which will translate in space with the trajectory $\mathbf{X}(t)$. Then, radial symmetry makes the choice of a specific orientation of the x and y axes on the horizontal plane arbitrary, so we are free to choose a given static direction.

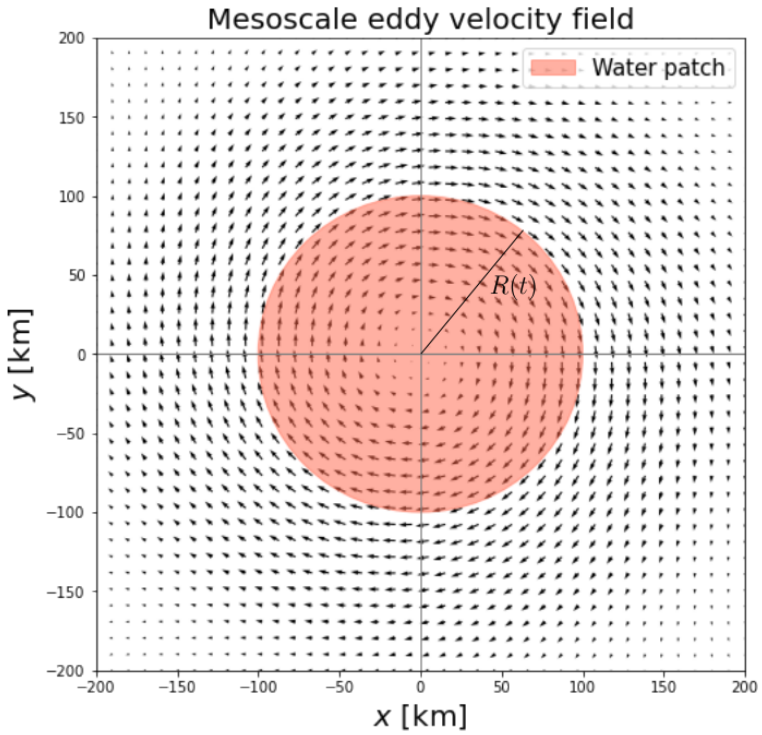

Figure 8.2: Mesoscale eddy local velocity field, projected on the x-y plane, in the special case of radial symmetry. The radial component is given by the divergence, while the angular component is the rotational flow.

Imaging that the planktonic ecosystem we aim to describe belongs to the Southern Ocean, and so is iron limited, we can exploit again information from [1], [13], [21], [25], [19], [11] to define realistic parameters and concentrations in the system (see Tables 8.1, 8.2). In particular, the horizontal diffusivity κ^h was kept relatively small to preserve eddy coherence [15]. Contrary to the SOIREE experiment, initially the patch is not fertilized, so distribution means are set equal to the horizontal surrounding. We suppose also that the eddy extends vertically until the water surface, and so only downward vertical expansion can occur. This can be modelled just redefining equations (4.15), (4.17) and (4.19) in a way that *above* increase of volume is fully redirected to the one *below*.

parameter	**value**	**unit of measure**
γ_0	0	day^{-1}
δ_0	$1 \cdot 10^{-4}$	day^{-1}
κ_0^h	5.0	$\text{km}^2 \cdot \text{day}^{-1}$
κ_0^v	$2.1 \cdot 10^{-5}$	$\text{km}^2 \cdot \text{day}^{-1}$
ν	1.1	day^{-1}
k	1.73	$(\mu\text{mol Fe}) \cdot \text{m}^{-3}$
m	0.05	day^{-1}
ϕ	1.64	$\mu\text{atm} \cdot \text{kg} \cdot (\mu\text{mol C})^{-1}$
K_o	0.06	$(\mu\text{mol C}) \cdot \text{kg}^{-1} \cdot \mu\text{atm}^{-1}$
K_g	17.28	$\text{m} \cdot \text{day}^{-1}$
h	65	m
ρ	1027	$\text{kg} \cdot \text{m}^{-3}$
B	10	#
$R_{C_T:Fe}$	$6 \cdot 10^4$	$(\mu\text{mol C}) \cdot (\mu\text{mol Fe})^{-1}$

Table 8.1: Set of parameters used to simulate the mesoscale eddy.

variable	value	unit of measure
$W(0)$	60	km
$L(0)$	60	km
$T(0)$	30	m
$\langle N \rangle_{pat}(0)$	0.08	$(\mu\text{mol Fe}) \cdot \text{m}^{-3}$
$\langle P \rangle_{pat}(0)$	0.0249	$(\mu\text{mol Fe}) \cdot \text{m}^{-3}$
$\langle \Delta p \rangle_{pat}(0)$	0	μatm
$\langle N^h \rangle_{suh}(0)$	0.08	$(\mu\text{mol Fe}) \cdot \text{m}^{-3}$
$\langle P^h \rangle_{suh}(0)$	0.0249	$(\mu\text{mol Fe}) \cdot \text{m}^{-3}$
$\langle \Delta p^h \rangle_{suh}(0)$	0	μatm
$\langle N^b \rangle_{sub}(0)$	0.30	$(\mu\text{mol Fe}) \cdot \text{m}^{-3}$
$\langle P^b \rangle_{sub}(0)$	0	$(\mu\text{mol Fe}) \cdot \text{m}^{-3}$
$\langle \Delta p^b \rangle_{sub}(0)$	0	μatm

Table 8.2: Initial environmental conditions used to simulate the mesoscale eddy. Internal and external variances and covariances are initially set to zero and are not reported for compactness.

The action of divergence and horizontal diffusion brings to a slight increase of the patch radius, reaching about 72 km on the last day (Fig. 8.3A). Upwelling, determined by vertical diffusivity and divergence, provokes a sensible change in the patch thickness, rising from 30 to 50 m (Fig. 8.3B). In its entirety, the total volume grows by a factor of 2, mainly due to vertical intrusion of water from below (Fig. 8.3C, 8.3D). Initially, in fact, vertical entrainment is approximately the double of the horizontal one, although then it drops to a similar rate.

Initial iron concentration inside the patch is risen by intrusion of nutrient-rich surrounding water, but then, after around 20 days, is limited by the meanwhile increase of phytoplankton population, which consume it. At the last day of the simulation, we end up with the same starting iron concentration, but also with the double of phytoplanktonic organisms present (Fig. 8.4A, 8.4E, 8.4F).

Variances of iron and phytoplankton peak correspondingly to their means maxima (Fig. 8.4B). The main contribution to this is given by vertical entrainment and biological uptake, working in an opposite way for iron with respect to phytoplankton (Fig. 8.4G, 8.4H). This description remains coherent to what we found simulating SOIREE.

During the eddy life cycle, phytoplankton population is still in the growth phase, and this stimulates iron-phytoplankton correlation to remain positive (Fig. 8.4C). The respective covariance is mainly fed by biological consumption, while this time entrainment acts with an opposite effect (Fig. 8.4D).

The predicted pCO_2 anomaly amounts to about 6 μatm, even if the distribution is again heterogeneous in space. As usual, entrainment and air-sea flux counterbalance the carbon consumption, both in the dynamics of the means and the variances (Fig. 8.5A, 8.5B, 8.5C, 8.5D).

Finally, correlations of N and P with Δp are depicted in Figures 8.5E and 8.5G. The first one stays negative but not so distant to zero, meaning that the correlation is not so strong. This can be related to the delay between iron and phytoplankton maxima. The second one remains instead very negative and robust, but that's expected since phytoplankton growth implies carbon uptake.

In summary, results of the simulation show that the upwelling of nutrients inside a mesoscale eddy in the Southern Ocean can cause a doubling of the phytoplanktonic organisms, at least for the time scales considered. The subsequent unraveling of the eddy shape due to the strain could then, hypothetically, disperse the produced biomass into the surrounding ocean.

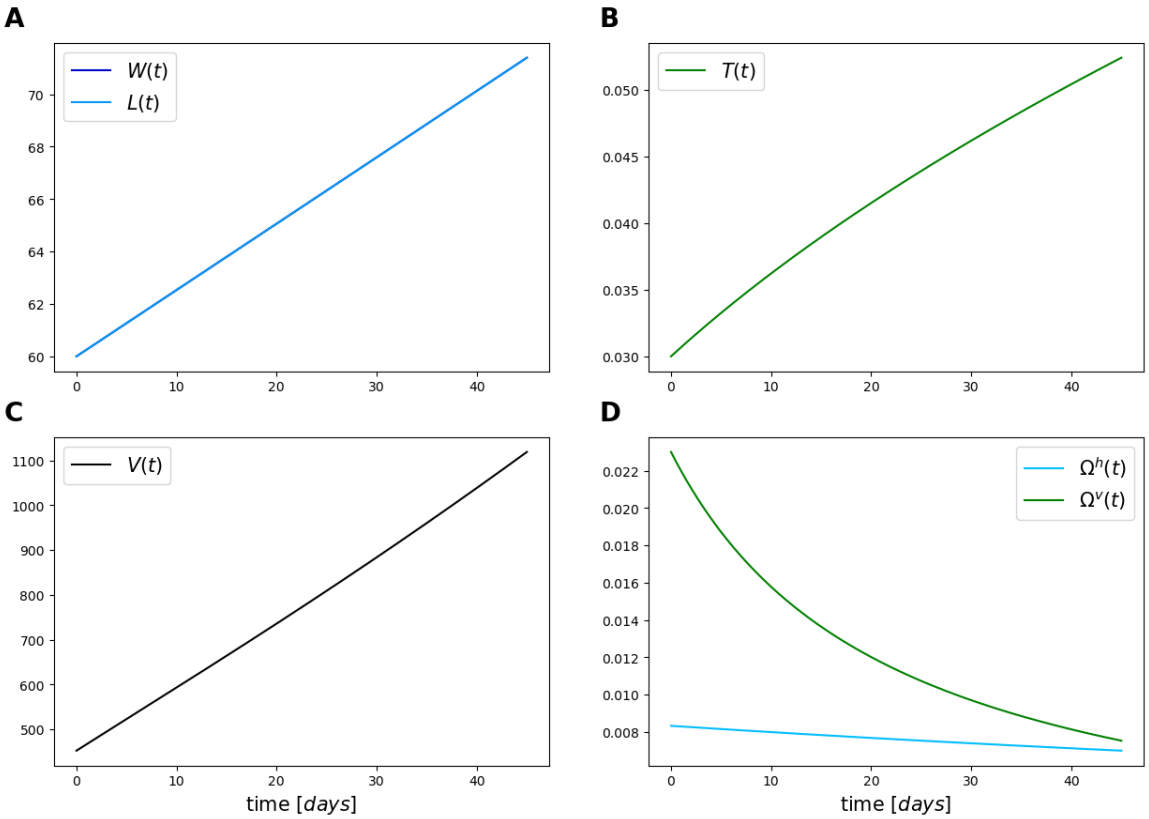

Figure 8.3: Simulation of the eddy water patch evolution, starting from a circular water patch with radius of 60 km and thickness of 30 m. Predicted and measured width and length of the patch are depicted in panel **A**, thickening process in panel **B**, while total volume increase in panel **C**. Horizontal and vertical entrainment rates, obtained from relative volume changes, are represented in panel **D**.

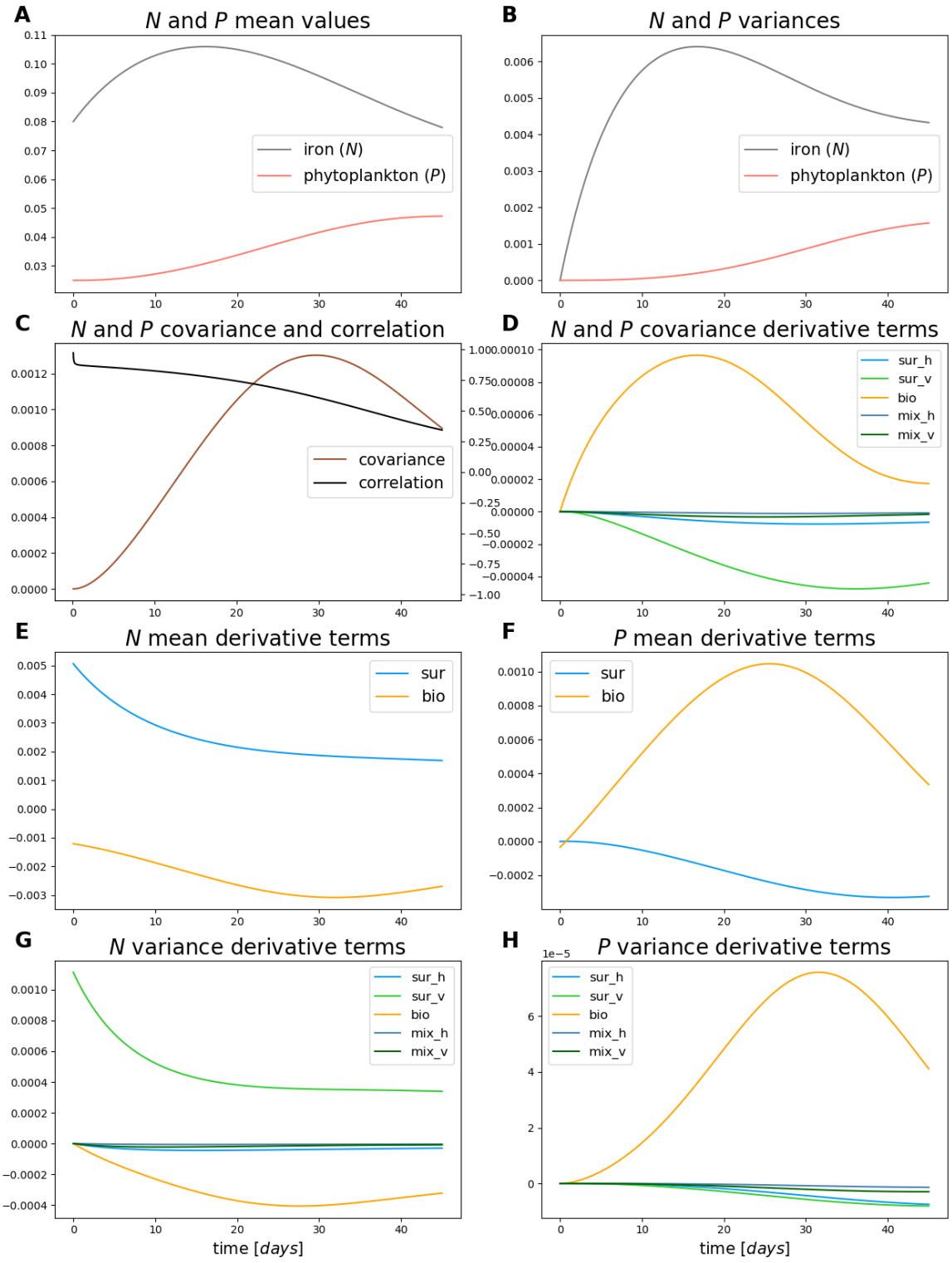

Figure 8.4: Simulation of the eddy tracers with the statistical model, accounting for heterogeneity. In panels **A** and **B** are represented iron and phytoplankton concentrations means and variances, respectively. Iron-phytoplankton covariance and correlation, defined in (7.3), and covariances derivative terms of equation (5.22) are depicted in panels **C** and **D**. Mean derivative terms for iron and phytoplankton of (5.20) are present in panels **E** and **F**, as well as variance derivative terms (5.21) in panels **G** and **H**. See text for a complete analysis.

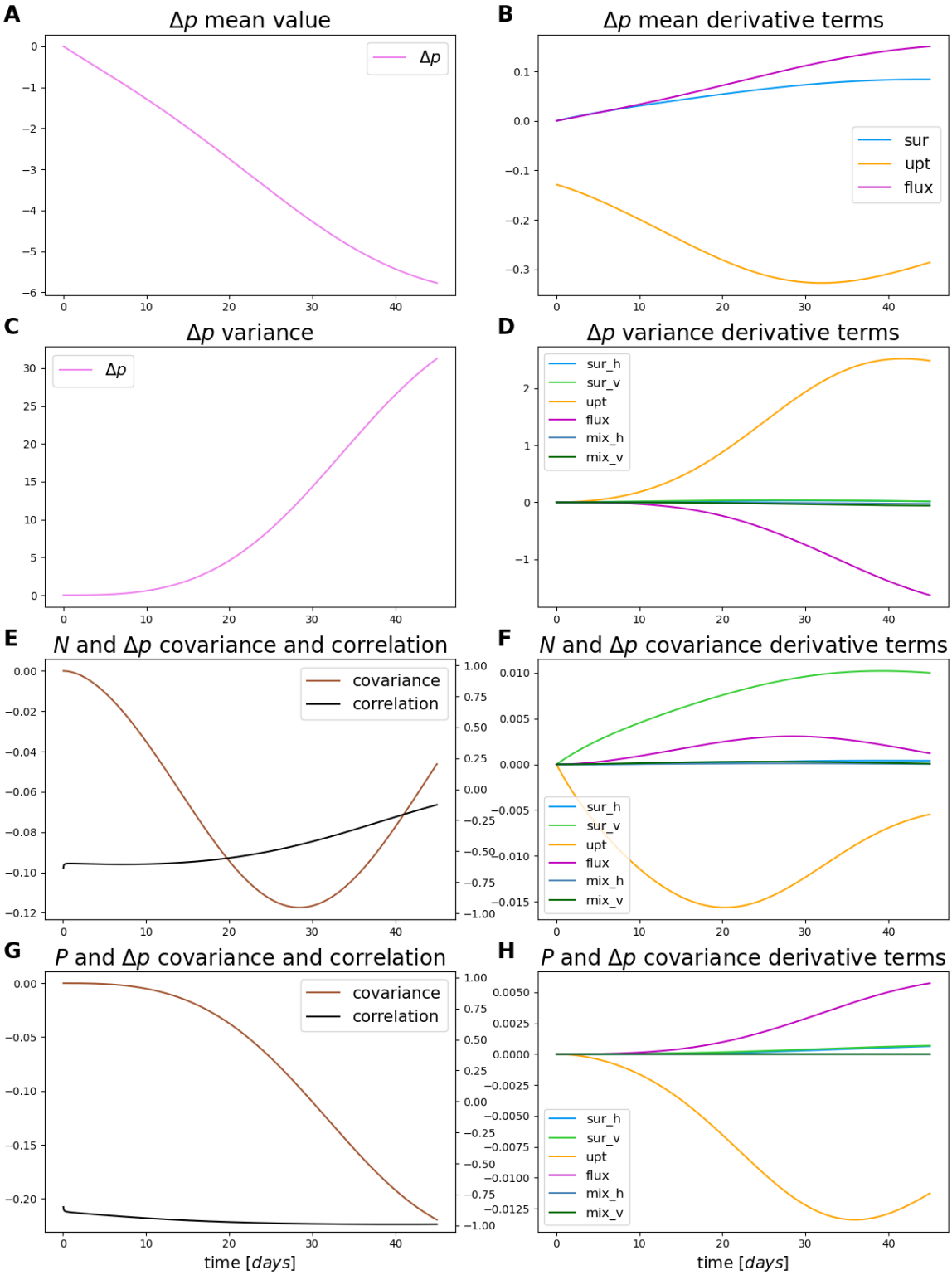

Figure 8.5: Simulation of the eddy tracers with the statistical model, accounting for heterogeneity. In panel **A** is represented mean pCO_2 anomaly, while in panels **C**, **E** and **G** are depicted, respectively, Δp variance, iron-Δp covariance-correlation and phytoplankton-Δp covariance-correlation. On the right, all the derivative terms present in the full model equations (5.20), (5.21), (5.22) are shown in panels **B**, **D**, **F** and **H**. See text for complete analysis.

Chapter 9

Conclusions and Future Works

In this work, we proposed a theory to describe plankton ecosystems in the ocean that is linked to Lagrangian description of fluid flows. Starting from the biological interaction between phytoplankton and a generic limiting nutrient inside a delimited water parcel, we implemented a simple homogeneous model taking into account the entrainment of external water with different concentrations of the elements. We then focused on the description of a water patch using a Lagrangian approach, showing that the main sources of deformation are straining, divergence and diffusion. The rate of increase in volume gives hence a measure of the entrainment from outside. In order to describe how a set of tracers linked to the patch evolves in time, we defined a general master equation, accounting for entrainment, mixing and interactions. We exploited mathematical tools like Reynolds decomposition and closure methods to simplify the model, focusing on the characterization of means, variances and covariance of the tracer distributions. This was a crucial point since heterogeneity has been maintained, at least at the first order, without involving complex PDEs in the description. At this point, we applied the statistical formalism that we presented to the initial simple schema, adding the contribution of the carbon in terms of CO_2 partial pressure anomaly. We used this approach to mimic the results of the SOIREE fertilization experiment, obtaining good accuracy in replicating the trend of pCO_2 anomaly during the initial phase. Finally, we explored the possibility of applying this general Lagrangian ecosystem description to model more complex three-dimensional entities like mesoscale eddies in the ocean, obtaining a meaningful prediction of tracers' behavior.

Some aspects of this presented work can be further explored, such as stability of the heterogeneous N-P system from a dynamical system perspective. Some ongoing research has also to clarify the effect of turbulent mixing on tracers' moments decay, and what are the time scales involved in these phenomena. Related to the SOIREE experiment simulation, the temperature contribution could be considered once collected from continuous measurements along the 42 days, which was not possible due to the lack of official data. In the analysis of mesoscale eddies, we also restricted ourselves to a simple case in which non-rigid rotation is neglected, but this obviously discards important properties of the flow.

An advantage of the proposed Lagrangian model for oceanic ecosystems is that it's very versatile, and can be used in a plenty of different contexts. The generic identity of the tracers involved in the theoretical framework allows considering, for example, injections of any kind of drifting substances, like, for instance, pollutants'. Biogeochemical description can also be enriched by considering a higher number of phytoplanktonic or zooplanktonic consumers, together with multiple limiting nutrients. This would get insights on how patchiness can really drive the spatial correlations between diverse resources and organisms. Even community ecology approaches would benefit of the Lagrangian representation, with the possibility to identify dispersal processes with the entrainment of waters across the patch boundaries.

Acknowledgements

I thank Prof. Suweis, that is the Thesis Supervisor, for making himself available despite his numerous commitments and for his valuable advice.

I want to give special thanks to Prof. Ser-Giacomi, that is the Thesis Co-supervisor, for always been present and always helping me in my Erasmus experience at Palma de Mallorca and in the writing of this thesis. I hope to work with him again in the future.

To my family, that in a difficult period did not hesitate to support me in my choices, and to all my friends, who are looking forward to celebrating this important step in my life.

Bibliography

[1] Edward R Abraham et al. "Importance of stirring in the development of an iron-fertilized phytoplankton bloom". In: *Nature* 407.6805 (2000), pp. 727–730.

[2] Vincenzo Artale et al. "Dispersion of passive tracers in closed basins: Beyond the diffusion coefficient". In: *Physics of Fluids* 9.11 (1997), pp. 3162–3171.

[3] Richard Stephen Kent Barnes and Roger N Hughes. *An introduction to marine ecology*. John Wiley & Sons, 1999.

[4] Philip W Boyd et al. "A mesoscale phytoplankton bloom in the polar Southern Ocean stimulated by iron fertilization". In: *Nature* 407.6805 (2000), pp. 695–702.

[5] PW Boyd and CS Law. "The Southern Ocean iron release experiment (SOIREE)—introduction and summary". In: *Deep Sea Research Part II: Topical Studies in Oceanography* 48.11-12 (2001), pp. 2425–2438.

[6] Laura A Bristow et al. "Nutrients that limit growth in the ocean". In: *Current Biology* 27.11 (2017), R474–R478.

[7] Francisco P Chavez, Monique Messié, and J Timothy Pennington. "Marine primary production in relation to climate variability and change". In: *Annual review of marine science* 3 (2011), pp. 227–260.

[8] Dudley B Chelton et al. "Global observations of large oceanic eddies". In: *Geophysical Research Letters* 34.15 (2007).

[9] Raffaele Corrado et al. "General characteristics of relative dispersion in the ocean". In: *Scientific reports* 7.1 (2017), p. 46291.

[10] Helen S Findlay et al. "Modelling of autumn plankton bloom dynamics". In: *Journal of plankton research* 28.2 (2006), pp. 209–220.

[11] Russell Frew et al. "Macronutrient and trace-metal geochemistry of an in situ iron-induced Southern Ocean bloom". In: *Deep Sea Research Part II: Topical Studies in Oceanography* 48.11-12 (2001), pp. 2467–2481.

[12] Christopher Garrett. "On the initial streakness of a dispersing tracer in two- and three-dimensional turbulence". In: *Dynamics of Atmospheres and Oceans* 7.4 (1983), pp. 265–277. ISSN: 0377-0265. DOI: https://doi.org/10.1016/0377-0265(83)90008-8. URL: https://www.sciencedirect.com/science/article/pii/0377026583900088.

[13] Etienne Hannon et al. "Modeling the bloom evolution and carbon flows during SOIREE: Implications for future in situ iron-enrichments in the Southern Ocean". In: *Deep Sea Research Part II: Topical Studies in Oceanography* 48.11-12 (2001), pp. 2745–2773.

[14] Robert W Howarth. "Nutrient limitation of net primary production in marine ecosystems". In: *Annual review of ecology and systematics* 19.1 (1988), pp. 89–110.

[15] Alexandra E Jones-Kellett and Michael J Follows. "A Lagrangian coherent eddy atlas for biogeochemical applications in the North Pacific Subtropical Gyre". In: *Earth System Science Data* 16.3 (2024), pp. 1475–1501.

[16] Pijush K Kundu, Ira M Cohen, and David R Dowling. *Fluid mechanics*. Academic press, 2015.

[17] C. Lancelot and P. W. Boyd. *Model results: daily avg surface pCO2 from the R/V Tangaroa 61TG3052 cruise in the Southern Ocean during 1999 (SOIREE project)*. Tech. rep. Biological and Chemical Oceanography Data Management Office (BCO-DMO), Version Date 2008-08-25. URL: http://lod.bco-dmo.org/id/dataset/2889.

[18] C. Lancelot and P. W. Boyd. *Surface water CO2 concentrations from R/V Tangaroa cruise 61TG3052 in the Southern Ocean in 1999 (SOIREE project)*. Tech. rep. Biological and Chemical Oceanography Data Management Office (BCO-DMO), Version Date 2010-02-03. URL: http://lod.bco-dmo.org/id/dataset/2843.

[19] Christiane Lancelot et al. "Modeling phytoplankton blooms and carbon export production in the Southern Ocean: dominant controls by light and iron in the Atlantic sector in Austral spring 1992". In: *Deep Sea Research Part I: Oceanographic Research Papers* 47.9 (2000), pp. 1621–1662.

[20] Lev Davidovich Landau and Evgenii Mikhailovich Lifshitz. *Fluid mechanics: Landau And Lifshitz: course of theoretical physics, Volume 6*. Vol. 6. Elsevier, 2013.

[21] Yuan-Hui Li and Tien-Fung Tsui. "The solubility of CO2 in water and sea water". In: *Journal of Geophysical research* 76.18 (1971), pp. 4203–4207.

[22] Qian Liu, Yingjie Liu, and Xiaofeng Li. "Characteristics of surface physical and biogeochemical parameters within mesoscale eddies in the Southern Ocean". In: *Biogeosciences* 20.23 (2023), pp. 4857–4874.

[23] Dennis J McGillicuddy Jr. "Mechanisms of physical-biological-biogeochemical interaction at the oceanic mesoscale". In: *Annual Review of Marine Science* 8 (2016), pp. 125–159.

[24] Surabi Menon et al. *Couplings between changes in the climate system and biogeochemistry*. Tech. rep. Lawrence Berkeley National Lab.(LBNL), Berkeley, CA (United States), 2007.

[25] François MM Morel, John G Rueter, and Neil M Price. "Iron nutrition of phytoplankton and its possible importance in the ecology of ocean regions with high nutrient and low biomass". In: *Oceanography* 4.2 (1991), pp. 56–61.

[26] Akira Okubo. "Oceanic diffusion diagrams". In: *Deep sea research and oceanographic abstracts*. Vol. 18. 8. Elsevier. 1971, pp. 789–802.

[27] Ruma Pal, Avik Kumar Choudhury, et al. *An introduction to phytoplanktons: diversity and ecology*. Tech. rep. Springer, 2014.

[28] Enrico Ser-Giacomi et al. "A Lagrangian model for drifting ecosystems reveals heterogeneity-driven enhancement of marine plankton blooms". In: *Nature Communications* 14.1 (2023), p. 6092.

[29] Miles A Sundermeyer and James F Price. "Lateral mixing and the North Atlantic Tracer Release Experiment: Observations and numerical simulations of Lagrangian particles and a passive tracer". In: *Journal of Geophysical Research: Oceans* 103.C10 (1998), pp. 21481–21497.

[30] Jinyun Tang and William J Riley. "Finding Liebig's law of the minimum". In: *Ecological Applications* 31.8 (2021), e02458.

[31] J-L Thiffeault. "Scalar decay in chaotic mixing". In: *Transport and Mixing in Geophysical Flows: Creators of Modern Physics*. Springer, 2008, pp. 3–36.

[32] Geoffrey K Vallis. *Atmospheric and oceanic fluid dynamics*. Cambridge University Press, 2017.

[33] Philip J Wallhead, Adrian P Martin, and Meric A Srokosz. "Spatially implicit plankton population models: transient spatial variability". In: *Journal of Theoretical Biology* 253.3 (2008), pp. 405–423.

[34] Zi-Fei Wang et al. "Two typical merging events of oceanic mesoscale anticyclonic eddies". In: *Ocean Science* 15.6 (2019), pp. 1545–1559.

[35] Richard G Williams and Michael J Follows. *Ocean dynamics and the carbon cycle: Principles and mechanisms*. Cambridge University Press, 2011.